



Spin Transport in Magnetic Nano-Structures

Item Type	text; Electronic Dissertation
Authors	Chen, Kai
Publisher	The University of Arizona.
Rights	Copyright © is held by the author. Digital access to this material is made possible by the University Libraries, University of Arizona. Further transmission, reproduction or presentation (such as public display or performance) of protected items is prohibited except with permission of the author.
Download date	22/05/2018 06:04:15
Link to Item	http://hdl.handle.net/10150/626524

SPIN TRANSPORT IN MAGNETIC NANO-STRUCTURES

by

Kai Chen

Copyright © Kai Chen 2017

A Dissertation Submitted to the Faculty of the

DEPARTMENT OF PHYSICS

In Partial Fulfillment of the Requirements

For the Degree of

DOCTOR OF PHILOSOPHY

In the Graduate College

THE UNIVERSITY OF ARIZONA

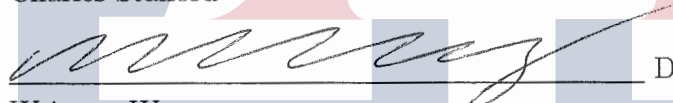
2017

THE UNIVERSITY OF ARIZONA
GRADUATE COLLEGE

As members of the Dissertation Committee, we certify that we have read the dissertation prepared by Kai Chen entitled Spin Transport in Magnetic Nano-Structures and recommend that it be accepted as fulfilling the dissertation requirement for the Degree of Doctor of Philosophy.


Date: December 01, 2017
Brian LeRoy


Date: December 01, 2017
Charles Stafford


Date: December 01, 2017
Weigang Wang

Final approval and acceptance of this dissertation is contingent upon the candidate's submission of the final copies of the dissertation to the Graduate College.

I hereby certify that I have read this dissertation prepared under my direction and recommend that it be accepted as fulfilling the dissertation requirement.


Date: December 01, 2017
Shufeng Zhang

STATEMENT BY AUTHOR

This dissertation has been submitted in partial fulfillment of the requirements for an advanced degree at the University of Arizona and is deposited in the University Library to be made available to borrowers under rules of the Library.

Brief quotations from this dissertation are allowable without special permission, provided that an accurate acknowledgement of the source is made. Requests for permission for extended quotation from or reproduction of this manuscript in whole or in part may be granted by the head of the major department or the Dean of the Graduate College when in his or her judgment the proposed use of the material is in the interests of scholarship. In all other instances, however, permission must be obtained from the author.

SIGNED: Kai Chen

ACKNOWLEDGEMENTS

It has been a wonderful adventure pursuing the doctorate degree in Physics at University of Arizona. I would like to take this opportunity to express my gratitude to all those who helped to make the past five years fruitful and pleasant.

Among all of them, I especially wish to thank my advisor Dr. Shufeng Zhang for his guidance and support. Throughout my graduate studies, Dr. Zhang has been interested and passionate about any progresses I have made and been patient and encouraging when I got myself stuck. Also, whenever I came up with questions, Dr. Zhang is there ready for a discussion, even on weekends. It is a memorable experience doing my graduate research with an advisor who is so enthusiastic about science.

Besides, I would like to thank Dr. Chia-Ling Chien, Dr. Weiwei Lin at Johns-Hopkins University and Dr. Haifeng Ding from Nanjing University for sharing with us their inspiring data prior to publication. Some of our papers wouldn't have been there without their results and suggestions. My sincere thanks also goes to all my committee members and Dr. Koen Visscher for providing such a supportive environment.

Also, I am indebted to my fellow classmates and all fiends. Parties and talks with Jianping Jiang, Kun Zhang and Lei Ye indeed relieved much of the stress and anxiety from research and life. Traveling and hiking with Yijun Ding, Shulei Zhang, Baijie Gu, Huanian Zhang, Gongwen Zu and Xin Zi has been such wonderful memories. I am also grateful to my dear colleagues Lei Xu, Shulei Zhang, Yihong Cheng and Anirban Kundu inspiring ideas and discussions and all the work we have done together.

At last, I thank my parents, my wife and my sister for love and best wishes. Without them being so supportive, none of those were even possible.

DEDICATION

To my wife

TABLE OF CONTENTS

LIST OF TABLES	9
LIST OF FIGURES	10
ABSTRACT	15
CHAPTER 1. INTRODUCTION	16
1.1. Background and Overview	16
1.1.1. Spin dependent electron transport	16
1.1.2. Magnon mediated spin transport	18
1.1.3. Interplay between magnetization dynamics and electron currents	20
1.2. Outline of the Dissertation	22
CHAPTER 2. LINEAR RESPONSE THEORY OF SPIN PUMPING	24
2.1. Motivation	24
2.2. Derivation of the Formula	25
2.3. Results and Discussion	28
2.3.1. Comparison with Scattering theory in ideal limit	28
2.3.2. Diffusive Contact	30
2.3.3. Numerical Results in Layered Structures	30
2.4. Experiments Demonstration of Spin Pumping	33
2.4.1. Enhanced Gilbert damping	34
2.4.2. Inverse spin Hall voltage	35
2.5. Spin Pumping in the presence of Spin-Orbit Coupling	35
2.6. Spin Pumping induced Electric Voltage	43
2.6.1. Spin pumping induced electric voltages	43
2.7. Results and discussions	44
CHAPTER 3. SPIN HALL MEASUREMENT IN SPIN PUMPING AND SPIN TRANSFER TORQUE	48
3.1. Experiments Measurement of spin Hall angle	48
3.2. Role of non-local spin Hall conductivity	50
3.2.1. Role of None Local Conductivity in Spin Hall Measurement .	50
3.2.2. Calculation of Conductivity in Thin Films	53

TABLE OF CONTENTS—*Continued*

3.2.3. Controversy between differently measured spin Hall angle . . .	54
CHAPTER 4. SPIN CONVERTANCE AT MAGNETIC INTERFACES	58
4.1. Motivation	58
4.2. Magnons and Spin batteries	59
4.2.1. Three spin Batteries	59
4.2.2. Magnons in Ferromagnets and Anti-ferromagnets	63
4.3. Spin convertance driven by Various Batteries	65
4.3.1. Spin conductance of a spin pumping battery	65
4.3.2. Spin conductance of a temperature gradient spin battery	68
4.3.3. Spin conductance with the spin Hall battery	69
4.4. Spin current enhancement via insertion of thin NiO layer	70
4.4.1. Boundary conditions for spin currents in multilayers	71
4.4.2. Modeling spin current at elevated temperatures	72
4.4.3. Discussions and conclusions	74
4.5. Other Remarks	75
4.5.1. Magnon density vs Magnon chemical potential	75
4.5.2. Different formalism of spin pumping	76
CHAPTER 5. SPIN TRANSPORT IN WEAK SCATTERING MEDIA IN THE PRESENCE OF SPIN-ORBIT COUPLING	77
5.1. Spin diffusion equation and spin injection into disordered medium	77
5.2. Spin transport equation in ballistic medium	80
5.3. Spin injection into ballistic medium	83
APPENDIX A. CONDUCTIVITY IN LAYERED THIN FILMS	89
A.1. Model Hamiltonian	89
A.2. Tight binding Green's function in thin film	90
A.3. Compare with Semiclassical Results	91
A.3.1. Comparison with Drude Model	91
A.3.2. Comparison with results of Boltzmann Equation	92
A.4. spatial dependence of conductivity in the presence of interface states	93

TABLE OF CONTENTS—*Continued*

APPENDIX B. DERIVATION AND CALCULATION FOR SPIN TRANSPORT EQUATION IN BALLISTIC REGIME	97
B.1. Derivation of the ballistic spin transport equation	97
B.2. Detailed Calculation for spin injection into ballistic material	100
B.2.1. Resistance dominated by the tunnel barrier	100
B.2.2. General solution and exact calculation	101
REFERENCES	104

LIST OF TABLES

TABLE 3.1. Spin Hall angles reported by inverse spin Hall voltage and spin transfer torque experiments.	50
TABLE 4.1. List of spin conductance $G_{\text{int}}a^2$ (a is the lattice constant) of several magnetic interfaces driven by different batteries. In these bilayer structures, the spin current across the interface is $\mathbf{j}_s = G_{\text{int}}\mathbf{V}/(1 + \epsilon)$ where ϵ characterizes a backflow spin current and will be calculated in late sections. The Table gives the dependence of the SC on temperature T , interface coupling strength J_{int} , electron density of states at Fermi level $g_e(E_F)$, Curie temperature T_C , and Néel temperature T_N	62

LIST OF FIGURES

- FIGURE 1.1. Spin Hall and inverse spin Hall effect. Left: a charge current is injected along $-y$ direction. A spin current polarized in z direction flows along y direction is generated via spin Hall effect. Right: a spin current polarized in z direction is injected along $-x$ direction. A charge current flowing in y direction is generated via inverse spin Hall effect. 18
- FIGURE 1.2. (a). Structure of a bilayer for longitudinal spin Seebeck effect. (b). Structure for spin convertance experiment. The left Pt layer is the driving layer and the right Pt layer is the detecting layer. The spin current flow direction in both setups is in z direction. Magnetization is pinned in x direction (out of paper). 19
- FIGURE 1.3. (a): Illustration of spin transfer torque. An in plane charge current is injected along y direction. The spin Hall current flows in z direction which is polarized the x direction which builds up a spin accumulation near the interface. (b). Spin pumping: The magnetization of FM layer precesses around x direction, which emits a spin current into adjacent NM layer. A charge current is generated via inverse spin Hall effect. 21
- FIGURE 2.1. The position-dependence of the real part of the spin pumping conductance for two magnetic (FM)/non-magnetic (NM) bilayers. (a) Both magnetic and non-magnetic layers, whose spin-dependent potentials are shown above, are metallic. (b) The magnetic layer is a ferromagnetic insulator (FI) and the non-magnetic is a metal. The spin-dependent potentials are also shown ($V_0 - E_F = 9$ eV). The Fermi energy is $E_F = 6$ eV, and the exchange parameters are $J_{ex} = 0.5$ and 5.0 eV as marked in the Figure. 31
- FIGURE 2.2. Real and imaginary parts of the spin pump conductance of the FM layer sandwiched by two semi-infinite non-magnetic metal layers, NM/FM/NM. The Fermi level $E_F = 6$ eV and the thickness of the FM layer is $2d$. (a) $J_{ex} = 0.5$ eV, and $2d = 2$ nm. (b) $J_{ex} = 0.5$ eV, and $2d = 4$ nm. (c) $J_{ex} = 5.0$ eV, $2d = 2$ nm. (d) The dependence of the real part of the spin pumping conductance at the interface on ferromagnetic layer thickness for two different J_{ex} 32

LIST OF FIGURES—*Continued*

- FIGURE 2.3. Illustration of spin pumping (a) without and (b) with Rashba SOC at the interface. In both cases, (c) and (d), the spin current decays oscillatorily within FM layer and exponentially in the NM. The maximum spin current j_{max} occurs at $z = 0^-$. The dependence of j_{max} , normalized to its disorder-free value j_{max}^0 , on the ferromagnetic exchange constant for several values of the disorder parameter Δ , (e), where Δ is the imaginary part of self energy. The ratio of the interface spin current jump Δj_{int} to the spin current relaxed in the NM layer as a function of the SOC strength for several thickness of the NM layer, (f) (in plane spin polarization). 39
- FIGURE 2.4. The enhanced damping parameter and its anisotropy of spin pumping for several different SOC parameters. (a) The precessing axis is parallel to the layers with the backflow fraction at large NM thickness $\epsilon \equiv \xi/(1 + \xi) = 10\%$, and (b) $\epsilon = 40\%$. The dashed lines indicate the effective thickness of the interface. (c) The difference of the enhanced damping parameter for the precessing axis perpendicular and parallel to the layers for $\epsilon = 10\%$, and (d) $\epsilon = 40\%$. The inset in (a) is from the experimental data in ref. [41]. 41
- FIGURE 2.5. NM layer thickness dependence of the electric voltage calculated from Eq. (2.68) and (2.71). The parameters are: $\theta_{SH}^N = 0.1$, $\lambda_{IEE} = 0.06nm$, $\lambda_{sd} = 7.7nm$ and $\delta = 0.9$, $\sigma_F = 3.3 \times 10^6 \Omega^{-1}m^{-1}$, $t_F = 10nm$. The spin diffusion length used here is the value from ref. [40]. 45
- FIGURE 2.6. The comparison of the thickness dependence of the electric voltage between our theory and experiments of Nakayama *et al.* [40]. In our calculation, we used the values $L = 1.6mm$, $f = 9.44GHz$, $\mu_0 Ms = 0.72T$ which are from ref. [40]. We use $\delta = 0.9$ as the interface spin memory loss. With the best fit, we find $\theta_{SH}^N = 0.035$, $\lambda_{sd} = 11.8nm$, $\mu_0 h_{rf} = 1.7 \times 10^{-4}T$, $\Gamma(0) = 3.02 \times 10^{19}m^{-2}$, $\lambda_{IEE} = 0.055nm$. (a) dependence on the FM layer thickness for a fixed $t_N = 10nm$, and (b) dependence on the NM layer for a fixed t_F 47

LIST OF FIGURES—*Continued*

- FIGURE 3.1. Illustration of spin Hall measurement. (a) A precessing magnetic layer pumps the spin current into the heavy metal. An electric field (or a charge voltage) from the ISH effect is measured. (b) An applied in-plane electric current accompanies a spin current flowing perpendicular to the layer due to SH effect. The spin current exerts a torque on the ferromagnetic layer which is being measured. The table of the spin Hall angles shows a wide range of values for these two classes of measurement. 49
- FIGURE 3.2. (a) and (b): Spatial dependence of the electric conductivity across a FM ($z < 0$)/NM ($z > 0$) bilayer for different film thickness. The magnitude of the conductivity is normalized by the bulk value of the NM layer. (c): The correction factor R as a function of NM layer thickness. In above calculation, we have taken the density of states and for the FM and NM to be the same so that the conductivity ratio is identical to the ratio of electron mean free path. In In Fig. 2(a-c) we take the mean free path as $\lambda_N = 10$ nm and $\lambda_F = 5$ nm and the spin diffusion length as $\lambda_s = 10$ nm. In Fig 2(d), three different $\lambda_F = 20, 10, 5$ nm are shown. 55
- FIGURE 3.3. The conductivity of a thin film with and without surface states as a function of layer thickness, λ is the electron mean free path in the bulk. When there is no surface states, the semiclassical continuous model (black square line) and our tight-binding approach (red circle line) are approximately same. In the presence of the surface state (c), the conductivity increases at the small thickness. The details of the parameters used are given in the Appendix A. 56
- FIGURE 4.1. Spin waves in ferromagnets and antiferromagnets. The brown, red and blue arrows are the spins on the FI lattice, AFI sublattice A and AFI sublattice B , respectively. 64

LIST OF FIGURES—*Continued*

- FIGURE 4.2. The spin Seebeck signal enhancement factor, η_{th} , as a function of temperature for various spin conductance of the NM layer from $G_N = 1, 2, 5, 10, \infty$ (10^{18}m^{-2}), calculated by using Eq. (4.28). The parameters are $a_F = 1.39$ nm, $a_A = 0.42$ nm, $T_C = 560$ K, $T_N = 160$ K ($t_{\text{NiO}} = 0.6$ nm), $g_e(E_F) = 3n_e/2E_F$ with $n_e = 5 \times 10^{22}\text{cm}^{-3}$ and $E_F = 5$ eV. $J_{\text{YIG/Pt}} = 0.07$ eV and $J_{\text{NiO/Pt}} = 0.13$ eV are the sd constant at the interface. (a) The enhancement factor for a number of spin conductance of the NM layer. (b) Comparison of the experimental points [20] with the theoretical curve for $G_N = 6.7 \times 10^{18}\text{m}^{-2}$ 73
- FIGURE 5.1. Illustration of spin injection in lateral spin valve. In subfigure (a), we show the structure of a lateral spin valve. (b) shows the typical results of spin injection results taken from [127] where L is the distance between spin injector and spin detector. 79
- FIGURE 5.2. A model bilayer consists of a ferromagnet and a non-magnetic metallic layer separated by a tunnel barrier at $x = 0$. The spin-dependent transmission and reflection coefficients are T_σ and R_σ . The spin accumulation at both sides of the barrier is also shown and will be quantitatively calculated. 80
- FIGURE 5.3. Spin injection through a tunnel barrier ($T_\sigma \ll 1$) into a diffusive NM layer, $l_0/\lambda = 0.2$, the polarization of the barrier resistance is $p_J = 0.5$. We plot CPs and spin accumulation in unit of $\rho j_e p_J \lambda$. (a) The directional and spin dependence of chemical potentials in the NM layer for left-going, right-going, spin up and spin down electrons. (b) the spin-dependent CP μ_s and its ballistic part μ_b , as well as the spin accumulation δm derived from CPs shown in top panel. 84
- FIGURE 5.4. Spin injection through a tunnel barrier into a weak scattering NM layer where we choose $l_0/\lambda = 2$ and $p_J = 0.5$. All CPs and spin accumulation are plotted in unit of $\rho j_e p_J \lambda$. (a) The directional and spin dependence of chemical potentials in the NM layer for left-going, right-going, spin up and spin down electrons. (b) the spin-dependent CP μ_s and its ballistic part μ_b , as well as the spin accumulation δm . The dotted line shows $\delta m_0 = \rho j_e p_J \lambda e^{-x/\lambda}$ 86

LIST OF FIGURES—*Continued*

- FIGURE 5.5. The enhancement factor of spin accumulation as a function of the ratio of the mean free path and spin dephasing length for various transmission coefficients. The other parameters are, $\rho_F \lambda_F = 5$, $\rho_{F\sigma} l_{F\sigma} = 2$, $p_F = 0.5$, $\rho l_0 = 1$, $(h/e^2 N) = 2$, where $\rho_{F\sigma}$ ($l_{F\sigma}$) is the resistivity (mean free path) in FM layer for spin channel σ , $p_F = (\rho_{F\downarrow} - \rho_{F\uparrow})/(\rho_{F\downarrow} + \rho_{F\uparrow})$, λ_F is the spin diffusion length of the FM layer and $\rho_F = \rho_{F\uparrow} \rho_{F\downarrow}/(\rho_{F\downarrow} + \rho_{F\uparrow})$. 87
- FIGURE A.1. (a). The local and nonlocal contributions to the interface conductance as a function of the coupling between 2d and 3d states. In our calculation, we took $k_F a = 1$. (b). The current distribution throughout the bilayer for fixed hopping parameters. 94
- FIGURE A.2. The conductivity of a thin film with and without surface states as a function of layer thickness, λ is the electron mean free path in the bulk. When there is no surface states, the semiclassical continuous model (black square line) and our tight-binding approach (red circle line) are approximately same. In the presence of the surface state (c), the conductivity increases at the small thickness. The parameters used here: Rashba split is $0.2E_F$, mean free path 5 nm , the interfacial hopping $t_L/t = 0.4$. . 95

ABSTRACT

Since the discovery of giant magnetoresistance in 1980s, Spintronics became an exciting field which studies numerous phenomena including the spin transport in magnetic heterostructures, magnetization dynamics and the interplay between them. I have investigated different topics during my graduate research. In this dissertation, I summarize all my projects including spin pumping, spin convertance and spin injection into ballistic medium.

First, we develop a linear response formalism for spin pumping effect. Spin pumping refers that a precessing emits a spin current into its adjacent nonmagnetic surroundings, which was originally proposed using scattering theory. The newly developed formalism is demonstrated to be identical the early theory in limiting case. While our formalism is convenient to include the effects of disorders and spin-orbit coupling which can resolve the quantitative controversies between early theory and experiments. Second, the spin pumping experiments indicates a much smaller spin Hall angle compared with the results obtained via the spin transfer torque measurements. We found that such issues can be resolved when taking into consideration the effects of non-local conductivity. And we conclude neither of the two methods measures the real spin Hall angle while the spin pumping methods provides much accurate estimations. Third, we developed the spin transport equations in weak scattering medium in the presence of spin-orbit coupling. Before this, all spin dependent electron transport has been modeled by the conventional spin diffusion equation. While recent spin injection experiments have seen the failure of spin diffusion equation. As the experimental fitting using spin diffusion models led to unrealistic conclusions. At last, we study the spin convertance in anti-ferromagnetic multilayers, where the spin information can be mutually transferred between ferromagnetic/anti-ferromagnetic and conduction electrons. Our theory successfully explained the experiment results that the insertion of thin NiO film between YIG/Pt largely enhances the spin Seebeck currents.

CHAPTER 1

INTRODUCTION

1.1 Background and Overview

In 1988, Dr. Albert Fert and Dr. Peter Grünberg independently discovered the Giant Magnetoresistance (GMR) in Fe/Cr/Fe multilayers [1,2]. Experimental results showed that the electrical resistance of the trilayer is largely influenced by the relative magnetization direction between the two Fe layers. When the magnetization of two Fe layers are aligned to be parallel, the resistance of the trilayer is much smaller compared to that when they are aligned to be antiparallel. Since this Nobel prize winning discovery, many other exciting spin dependent phenomena have been reported in last thirty years, including spin Hall effect [3,4], spin transfer torque [6,7] and so on.

Based on the spin information carrier, all spin transport phenomena can be roughly classified into three major categories, i.e., spin dependent electron transport, magnon mediated spin transport, and the interplay between electronic current and magnetization dynamics. In this section, we briefly discuss some of those topics which are closely related to this dissertation.

1.1.1 Spin dependent electron transport

In conducting medium like metallic or semi-conducting heterostructures, both spin and charge information are carried by conduction electrons. In collinear magnetic multilayers, two-current model has been used to explain tons of transport phenomena [5]. In such theory, the charge current carried by spin up and spin down electrons are treated separately both in the bulk and at the interface. Both giant magnetoresistance and spin injection [8,9] can be readily explained using two current model. In materials with spin-orbit coupling, spin-charge conversion is of the most interesting spin transport topics. Here, we give some brief introduction about two of those ideas.

In magnetic metals, the electron density and the momentum relaxation rates for spin up and spin down electrons are different. When an electric field is applied, the

current carried by spin up/down electrons can be obtained via Drude model

$$j_{\uparrow} = en_{\uparrow}\tau_{\uparrow}E \quad (1.1)$$

$$j_{\downarrow} = en_{\downarrow}\tau_{\downarrow}E \quad (1.2)$$

where n_s is the electron density for spin up/down electrons, τ_s the relaxation time. We can rewrite the above currents by combining the two equations and introducing the spin dependent conductivity, $\sigma_s = en_s\tau_s$,

$$j_e = j_{\uparrow} + j_{\downarrow} = (\sigma_{\uparrow} + \sigma_{\downarrow})E \quad (1.3)$$

$$j_s = j_{\uparrow} - j_{\downarrow} = (\sigma_{\uparrow} - \sigma_{\downarrow})E \quad (1.4)$$

where j_e is the charge current and j_s is the spin current. In magnetic materials, $\sigma_{\uparrow} \neq \sigma_{\downarrow}$ and the electric current is always accompanied by a non vanishing spin current. In magnetic multilayers, we can also use such model which separates the current carried by spin up/down electrons. In last chapter of this thesis, we investigate spin injection into a two dimensional electron gas using this technique. Different from charge current can be fully determined by a flowing direction and magnitude, a spin current has a flowing direction and a spin polarization direction apart from the magnitude. For example, the above spin current has a flowing direction identical to the electric field, and polarization direction which is the direction of the magnetization (or up spin direction).

Electronic spin current can also be achieved in the absence of magnetic order. In heavy metals like Pt or Ta and some semi-conductors, there is strong spin-orbit coupling. When a charge current is injected, the spin up electrons are more likely to be scattered to left (or right) while spin down electrons are more scattered to the opposite direction which leads to a spin current flowing perpendicular to the charge current, as shown in Fig. 1.1(a),

$$j_s = \theta_H j_e \quad (1.5)$$

the θ_H is the spin Hall angle which characterize the conversion rate from charge current to spin current. In spin Hall effect, the spin current polarization direction, spin current flow direction and charge current flow direction are all perpendicular to the other two. Such spin current builds up a spin accumulation near the interface [12] which can be detected using optical method, or measured by spin transfer torque effects.

In the other way around, when a spin current is injected in such materials, a charge current will be generated which is referred as the ‘‘inverse spin Hall effect’’.

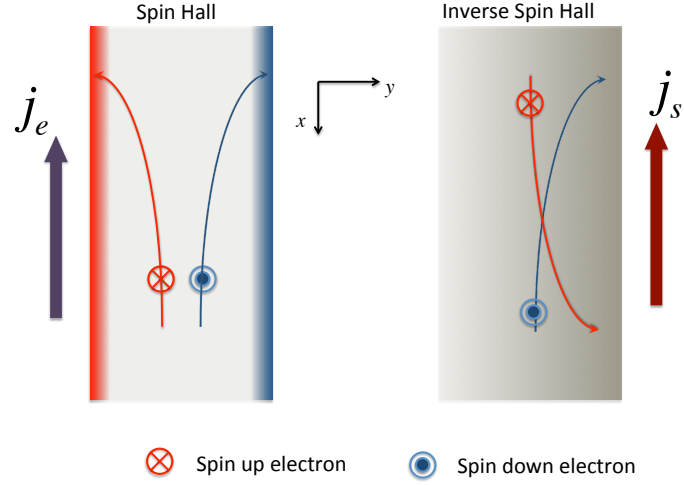


FIGURE 1.1. Spin Hall and inverse spin Hall effect. Left: a charge current is injected along $-y$ direction. A spin current polarized in z direction flows along y direction is generated via spin Hall effect. Right: a spin current polarized in z direction is injected along $-x$ direction. A charge current flowing in y direction is generated via inverse spin Hall effect.

The conversion rate is identical to the spin Hall angle,

$$j_e = \theta_H j_s. \quad (1.6)$$

Such inverse spin Hall effect makes it possible to detect spin transport electrically.

Besides the spin-orbit coupling in material bulk, the SOC at the interface also leads to spin-charge conversion. While different from the homogeneous symmetry in bulk material, The interface SOC results in a conversion between *only* in plane charge current and spin accumulation at the interface. At heavy metal interface or topological interface, there is spin momentum locking [11] or Rashba SOC [10]. An in plane charge current converts to a spin accumulation at the the interface which is referred as Rashba Edelstein effect [13]. The process vice versa is named as inverse Rashba Edelstein effect [14, 15]. Such spin-charge conversion contributes to the spin pumping induced electric voltages discussed in Chapter 2.

1.1.2 Magnon mediated spin transport

Low energy excitation of a magnetic spin lattice is known as magnon. In contrast to conduction electrons which carry both charge and spin information, magnons carry

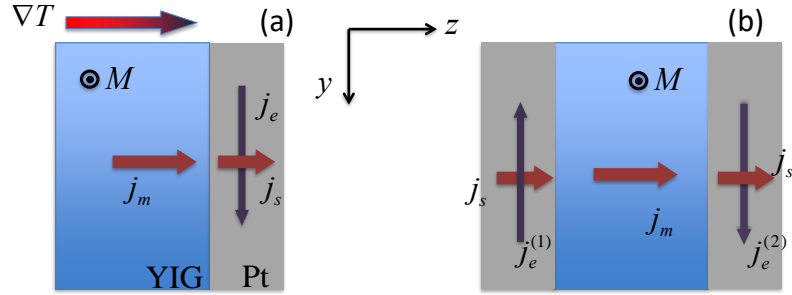


FIGURE 1.2. (a). Structure of a bilayer for longitudinal spin Seebeck effect. (b). Structure for spin convertance experiment. The left Pt layer is the driving layer and the right Pt layer is the detecting layer. The spin current flow direction in both setups is in z direction. Magnetization is pinned in x direction (out of paper).

only spin information. In magnetic insulators, only magnons are present, which makes magnetic insulators perfect systems to study magnon mediated spin transport. As magnon cannot be driven by electric field like electrons, up until now, magnonic transport is either driven by a thermal gradient or a non-equilibrium spin accumulation in an adjacent layer.

First, we discuss the thermally driven magnonic transport which is named as spin Seebeck effect and illustrated in Fig. 1.2(a). As magnons are bosonic particles, its occupation number is sensitive to temperature. When a thermal gradient applied to the YIG layer, more magnons are occupied at the hot end and less in the cold end. A resultant diffusive magnon current will flow from hot to cold end. When the YIG layer is coupled to heavy metal, the magnon current can be converted to electronic spin current in metal layer and detected utilizing inverse spin Hall effect. Notice that in both YIG and Pt layer, the polarization of the spin current is parallel to the magnetization direction.

The boundary condition at the YIG/Pt interface, say $z = z_0$, is modeled by the spin convertance proposed by Zhang and Zhang [16], including the continuity of spin current and the Ohm's law for interface conductance [16, 19],

$$j_m(z_0-) = j_s(z_0+) \quad (1.7)$$

$$g^{\text{th}} [\mu_m(z_0-) - \mu_s(z_0+)] = j_m(z_0-) \quad (1.8)$$

where $j_m(z_0-)$ and $j_s(z_0+)$ are the magnon and spin current near the interface, and $\mu_m(z_0-)$ and $\mu_s(z_0+)$ the spin accumulation. g^{th} is the interface spin conductance,

where “th” refers to incoherent thermal magnon. The thermal conductance will be related to following mixing conductance in later chapters.

Another driving source for magnon transport can be spin accumulation from adjacent layer. In Fig. 1.2(b), we show the structure to verify spin convertance proposed by Zhang and Zhang [16]. The idea can be divided into several steps: 1). We inject an in plane charge current in the driving layer (left). 2) Via spin Hall effect, a spin current flowing in perpendicular direction is generated which builds up a spin accumulation near the interface. 3) The spin accumulation can be converted to a magnon accumulation via spin convertance and the magnon accumulation leads to a diffusive magnon current in the YIG layer (middle). 4). The magnon current then converts back to electronic spin current at the right YIG/Pt interface. 5). The spin current in the right Pt layer can be electrically detected via inverse spin Hall effect.

In above paragraphs, we briefly outlined two magnonic transport phenomena. The YIG layer acts as the source layer in the first case while conducting medium layer in the second case. While they share the same boundary condition at interfaces, and same conductance. The meaning of g^{th} should become more clear in later chapters.

1.1.3 Interplay between magnetization dynamics and electron currents

Spin transfer torque is one of the most studied topics in spintronic research. The structure originally proposed by J. C. Slonczewski is a spin valve using two FM layer [6]. In his original proposal, the spin current and accumulation is polarized by a ferromagnetic layer. The resultant spin current can be used to switch the magnetization of another ferromagnetic layer. While the spin current in the following example it is generated from spin Hall effect. We consider a slightly different structure shown in Fig. 1.3(a) to illustrate the relation between spin pumping and spin transfer torque. The driving source here is an electric current injected along y direction. Via spin Hall effect, it generates a spin current flowing along z direction and polarized along x direction which builds up a spin accumulation near the interface $\boldsymbol{\mu} = \mu\hat{x}$. This spin accumulation in turn leads to a torque or a spin current at the interface [17],

$$\mathbf{j}_s = g_{\text{mix}}\mathbf{m} \times (\boldsymbol{\mu} \times \mathbf{m}) \quad (1.9)$$

where $g_{\text{mix}} = \sum_k 1 - r_{\uparrow}r_{\downarrow}^*$ is the “mixing conductance” which will also be used in spin pumping effect discussed below, \mathbf{m} is unit vector indicating the magnetization direction. And r_s is the spin dependent reflection coefficient at the interface In above equation, the mixing conductance can be understood as an interfacial conductance

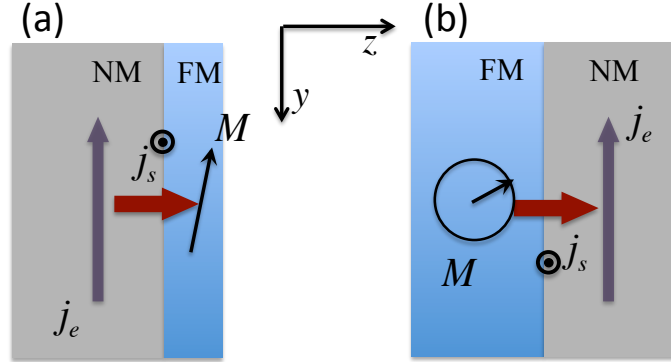


FIGURE 1.3. (a): Illustration of spin transfer torque. An in plane charge current is injected along y direction. The spin Hall current flows in z direction which is polarized the x direction which builds up a spin accumulation near the interface. (b). Spin pumping: The magnetization of FM layer precesses around x direction, which emits a spin current into adjacent NM layer. A charge current is generated via inverse spin Hall effect.

for a transverse spin accumulation in analogy to Shavin conductance for charge. The summation over k runs over all possible channels.

The magnetization of the FM layer then rotates subject to this spin current,

$$\frac{d\mathbf{m}}{dt} = -\gamma\mathbf{m} \times \mathbf{H}_{eff} + \beta\mathbf{m} \times (\boldsymbol{\mu} \times \mathbf{m}) \quad (1.10)$$

where β is the called the polarization factor which is proportional to the current density and inversely proportional to the FM layer size and magnetization. \mathbf{H}_{eff} is the effective field.

Spin pumping refers to the phenomena that a precessing ferromagnets emits a pure spin currents in to the adjacent NM layer as shown in Fig. 1.3(b) [24,25].

$$\mathbf{j}_s = \frac{\hbar}{2\pi} g_{\text{mix}} \mathbf{m} \times \frac{d\mathbf{m}}{dt} \quad (1.11)$$

where g_{mix} is the same mixing conductance. In above equation, the spin current flows from ferromagnetic layer to non-magnetic (NM) layer, and $\mathbf{M} \times \frac{d\mathbf{M}}{dt}$ indicates the spin polarization direction. To the leading order of precession angle, the spin pumping current is an a.c. current. While it has a d.c. components to the second order which is always measured as a detection of spin pumping.

Compared to spin transfer torque where a spin current drives the free layer magnetization to precessing, spin pumping effect addresses the inverse process where a spin current is generated by a precessing ferromagnet. Spin pumping is proved to be identical to spin transfer torque in terms of Onsager's reciprocity theorem [26]. Thus, they share the same interface conductance, g_{mix} .

1.2 Outline of the Dissertation

During my Ph.D. research, I have accomplished projects involving all of three above topics of which the details are discussed in later chapters. This thesis is organized as follows.

Chapter 2 and 3 are devoted to spin pumping effect. As we have mentioned that the spin pumping theory is originally formulated using scattering theory. The spin pumping efficiency is expressed in terms of spin dependent reflection coefficients at magnetic interfaces. While those transmission and reflection coefficients are convenient to use in ballistic transport regime or mesoscopic structures, they are difficult to determine in disordered materials. To solve such issues, we develop a linear response theory of spin pumping in Chapter 2. Our result for the spin current is formulated using real space Green's functions which are natural to include any disorders or spin-orbit couplings. Our result has been demonstrated to be identical to the conventional result in the limiting cases where any disorders and spin-orbit coupling is absent. Beyond this ideal case, we discuss the effects of spin-orbit coupling on spin pumping. We demonstrated that most of the spin pumping current is relaxed at the interface instead of relaxing in the nonmagnetic layer as assumed by early theory. We can resolve controversies on spin diffusion lengths reported by experiments from different groups.

In Chapter 3, we address another controversy in spin pumping experiments. Spin pumping and spin transfer torque are believed to be the inverse process of each other. Both of them can be used as experimental method to estimated the spin Hall angle and spin diffusion length in the NM metals. While the spin pumping experiments always predicts much smaller spin Hall angle compared to those reported from spin transfer torque experiments. By taking into account the non-local conductivity in thin films, we demonstrated that the spin pumping measurements always slightly underestimate the spin Hall angle while the spin transfer torque experiments always overestimate the spin Hall angle by a large amount.

In 2012, Zhang and Zhang proposed the spin convertance between ferromagnetic

magnon and conduction electrons [16]. In Chapter 4, we add anti-ferromagnetic magnons into the picture and discussed the anti-ferromagnetic (AF) magnon - conduction electron convertance, also the convertance between FM magnon and AF magnon. More interestingly, we propose that the spin pumping effect can be viewed in terms of electron-magnon spin convertance, which enables us to compare the mixing conductance to the spin convertance conductance. In addition, we applied our spin convertance results to study spin Seebeck in YIG/NiO/Pt trilayer structure. We confirm that the spin current can be is enhanced when a thin NiO film is inserted in between YIG and Pt [20].

In most spin dependent electron transport models, the spin current is described by spin diffusion equation which is only valid when the electron momentum relaxation is much faster than the spin relaxation. In such a diffusive limit, the electron momentum information is lost so fast that the spin information of all electrons can be approximated by a momentum averaged spin accumulation. In Chapter 5, we develop new equations to address spin transport in the opposite regime in weak scattering semiconductors where the electron momentum information lives longer than the spin information. In the end of 2014, D. Weiss *et al.* studied the spin injection into ballistic 2 dimensional electron gas [27]. Using traditional spin diffusion model, the estimated spin polarization of the injected current exceeds 600% which is unphysical. While using our transport equation, we found that the reported 600% is the real polarization amplified by a factor of $1 + l_0^2/\lambda^2$ where l_0, λ is the electron mean free path and the spin diffusion/dephasing length. The real spin polarization is still below 100%.

I would like to point out that some parts of this thesis have already been published in following papers [18, 19, 21–23].

CHAPTER 2

LINEAR RESPONSE THEORY OF SPIN PUMPING

By using the time-dependent linear response theory, we generalize the spin pumping formalism for a precessing magnet embedded in a non-magnetic conducting medium. The spin pumping current outside and inside the precessing magnetic layer can be calculated on an equal footing. Our formulation can be efficiently applied to systems with interface roughness and disorders. In the disorder-free limiting cases, we find the result is identical to the results derived from scattering theory.

2.1 Motivation

One of the most interesting spintronics phenomena is spin pumping which describes generation of a spin current in a non-magnetic metal layer by an adjacent precessing ferromagnetic layer. Up until now, the description of the spin pumping current \mathbf{j}_s is given by the scattering formalism [25] in which transport is formulated via reflection and transmission coefficients between the leads and the conductor [34],

$$\mathbf{j}_s = \frac{\hbar}{4\pi} \left(g_r \mathbf{m} \times \frac{d\mathbf{m}}{dt} - g_i \frac{d\mathbf{m}}{dt} \right) \quad (2.1)$$

where \mathbf{m} is a unit vector representing the precessing magnetization direction, g_r and g_i are the real and imaginary parts of the mixing conductance $g \equiv g_r + ig_i = \sum (1 - r_\sigma^* r_\sigma)$ in which r_σ is the reflection coefficient for the spin $\sigma = \uparrow, \downarrow$ at the interface between the non-magnetic and magnetic layers.

The above spin pumping theory has successfully been applied to many experimental realizations such as the enhancement of the Gilbert damping of thin films and spin pumping induced charge voltage. In spite of general acceptance of the spin pumping phenomenon, the reflection coefficients in the mixing conductance are usually calculated for an isolated interface [29] and the effects of disorders in the layers on the mixing conductance are completely discarded. As it has been known that the reflection and transmission coefficients are most useful for calculating transport in mesoscopic conductors, but rather inconvenient and prohibitively complicated for a diffusive system due to the presence of a large number of transverse scattering paths [30]. In diffusion systems, the standard and convenient description of transport

is to utilize linear response theories such as the Kubo formalism where the transport coefficients are expressed in terms of scattering parameters, e.g., mean free paths and spin diffusion lengths, so that the effects of disorders can be explicitly addressed. Indeed, theories for disordered media have already been attempted [35, 36].

2.2 Derivation of the Formula

In this chapter, we provide a derivation of the spin pumping current based on the time-dependent linear response theory in which the spin pumping current is related to a set of conventional spectral density functions instead of the reflection coefficients. Thus, disorders can be explicitly included via the retarded Green's functions. We have found a number of salient features of the spin pumping: 1) the mixing conductance is non-local, i.e., a two-point spin-pumping conductivity is necessary in order to relate the magnetization precessing at one site \mathbf{r}' to the induced current at another site \mathbf{r} , 2) the effect of disorders on spin pumping current can be explicitly included and thus, spin pumping depends on the interface as well as bulk scattering parameters, 3) the spin current also exists *inside the precessing magnetic layer* and can be determined by the same formalism, and 4) in the case of disorder-free layers, the present formulation is similar to that derived from the scattering theory [25].

We start by considering a magnetic particle or a magnetic layer embedded in a non-magnetic conducting medium. The magnetization of the magnetic layer is uniformly precessing around z -axis with a single frequency ω_0 ,

$$\mathbf{m}(\mathbf{r}, t) = \theta_F(\mathbf{r}) [m_s \mathbf{e}_z + \delta m (\mathbf{e}_x \cos \omega_0 t + \mathbf{e}_y \sin \omega_0 t)] \quad (2.2)$$

where δm is the precession amplitude which is small compared to the saturation magnetization $m_s \approx m_z$, $\theta_F(\mathbf{r})$ is a step function, i.e. $\theta_F(\mathbf{r}) = 1$ if \mathbf{r} is inside the precessing magnet and $\theta_F(\mathbf{r}) = 0$ if outside. The interaction between the itinerant electron spin and magnetization is modeled by the conventional exchange interaction, $V(\mathbf{r}, t) = -J_{ex} \boldsymbol{\sigma} \cdot \mathbf{m}(\mathbf{r}, t)$. Thus the total Hamiltonian is $H = H_0 + H'(t)$ where the time-independent term H_0 is

$$H_0 = H_{kin} - J_{ex} m_s \sigma^z \theta_F(\mathbf{r}) \quad (2.3)$$

where H_{kin} is the electron kinetic energy. The time-dependent perturbation is

$$H'(t) = -J_{ex} \sum_{\alpha=x,y} \sigma^\alpha m_\alpha(\mathbf{r}, t) \quad (2.4)$$

The spin current density tensor j_i^α , where α denotes the direction of spin-polarization and i the direction of transport, is calculated from the Kubo formula,

$$j_i^\alpha(\mathbf{r}, t) = \frac{iJ_{ex}}{2} \sum_{\beta=x,y} \int d^3r' \int dt' \Theta(t-t') \langle [\mathcal{J}_i^\alpha(\mathbf{r}, t), \mathcal{S}^\beta(\mathbf{r}', t')] \rangle m_\beta(\mathbf{r}', t') \quad (2.5)$$

where $\mathcal{S}^\beta(\mathbf{r}', t')$ and $\mathcal{J}_i^\alpha(\mathbf{r}, t)$ are spin density and spin current density operators defined in terms of the spinor quantum field operator $\psi(\mathbf{r}, t) = (\psi_\uparrow(\mathbf{r}, t), \psi_\downarrow(\mathbf{r}, t))^T$

$$\begin{aligned} \mathcal{S}^\alpha(\mathbf{r}, t) &= \psi^\dagger(\mathbf{r}, t) \sigma^\alpha \psi(\mathbf{r}, t), \\ \mathcal{J}_i^\alpha(\mathbf{r}, t) &= \frac{\hbar}{2m_e i} \psi^\dagger(\mathbf{r}, t) \sigma^\alpha \overleftrightarrow{\partial}_i \psi(\mathbf{r}, t), \end{aligned} \quad (2.6)$$

where $\overleftrightarrow{\partial}_i = \overrightarrow{\partial}_i - \overleftarrow{\partial}_i$ is the anti-symmetric differential operator.

The retarded response function in Eq. (2.5),

$$U_i^{\alpha\beta}(\mathbf{r}, \mathbf{r}'; t-t') \equiv -i\Theta(t-t') \langle [\mathcal{J}_i^\alpha(\mathbf{r}, t), \mathcal{S}^\beta(\mathbf{r}', t')] \rangle,$$

can be evaluated in the Matsubara frequency representation [37] outlined below. The equivalent imaginary time form is

$$U_i^{\alpha\beta}(\mathbf{r}, \mathbf{r}'; \tau) = -\langle [T_\tau \mathcal{J}_i^\alpha(\mathbf{r}, \tau) \mathcal{S}^\beta(\mathbf{r}', 0)] \rangle. \quad (2.7)$$

Inserting the spin current density and spin accumulation density from the definition,

$$\mathcal{J}_i^\alpha(\mathbf{r}, \tau) = \frac{\hbar}{2m_e i} \psi^\dagger(\mathbf{r}, \tau) \sigma^\alpha \overleftrightarrow{\partial}_i \psi(\mathbf{r}, \tau); \mathcal{S}^\alpha(\mathbf{r}, \tau) = \psi^\dagger(\mathbf{r}, \tau) \sigma^\alpha \psi(\mathbf{r}, \tau), \quad (2.8)$$

where $\psi(\mathbf{r}, \tau) = (\psi_\uparrow(\mathbf{r}, \tau), \psi_\downarrow(\mathbf{r}, \tau))^T$ is the spinor quantum field operator, we have

$$U_i^{\alpha\beta}(\mathbf{r}, \mathbf{r}'; \tau) = -\frac{\hbar}{2m_e i} \sum_{s_1 s_2 s_3 s_4} \langle T_\tau \psi_{s_1}^\dagger(\mathbf{r}, \tau) \sigma_{s_1 s_2}^\alpha \overleftrightarrow{\partial}_i \psi_{s_2}(\mathbf{r}, \tau) \psi_{s_3}^\dagger(\mathbf{r}', 0) \sigma_{s_3 s_4}^\beta \psi_{s_4}(\mathbf{r}', 0) \rangle. \quad (2.9)$$

Utilize Wick theorem, with the Mastubara Green's function defined as $[G(\mathbf{r}, \mathbf{r}'; \tau)]_{s_1 s_2} = -i \langle T_\tau \psi_{s_1}(\mathbf{r}, \tau) \psi_{s_2}^\dagger(\mathbf{r}, 0) \rangle$, we find

$$\begin{aligned} U_i^{\alpha\beta}(\mathbf{r}, \mathbf{r}'; \tau) &= -\frac{\hbar}{2m_e i} \sum_{s_1 s_2 s_3 s_4} \sigma_{s_1 s_2}^\alpha \sigma_{s_3 s_4}^\beta [G(\mathbf{r}', \mathbf{r}; -\tau)]_{s_4 s_1} \overleftrightarrow{\partial}_i [G(\mathbf{r}, \mathbf{r}'; \tau)]_{s_2 s_3} \\ &= \frac{\hbar}{2m_e i} Tr \left[\sigma^\alpha G(\mathbf{r}, \mathbf{r}'; \tau) \overleftrightarrow{\partial}_i \sigma^\beta G(\mathbf{r}', \mathbf{r}; -\tau) \right] \end{aligned} \quad (2.10)$$

Conduct Fourier transform $U_i^{\alpha\beta}(\mathbf{r}, \mathbf{r}'; i\omega_n) = \int_0^{\beta_0} d\tau e^{i\omega_n\tau} U_i^{\alpha\beta}(\mathbf{r}, \mathbf{r}'; \tau)$, the response function in frequency representation is

$$U_i^{\alpha\beta}(\mathbf{r}, \mathbf{r}'; i\omega_n) = \frac{1}{\beta_0} \sum_{i\omega_m} \frac{\hbar}{2m_e i} Tr \left[\sigma^\alpha G(\mathbf{r}, \mathbf{r}'; i\omega_m + i\omega_n) \overset{\leftrightarrow}{\partial}_i \sigma^\beta G(\mathbf{r}', \mathbf{r}; i\omega_m) \right] \quad (2.11)$$

where $\beta_0 = 1/k_B T$. After the frequency summation, we have

$$U_i^{\alpha\beta}(\mathbf{r}, \mathbf{r}'; \omega) = \frac{-i\omega}{2\pi} \frac{\hbar^3}{2m_e i} Tr \left[\sigma^\alpha G^R(\mathbf{r}, \mathbf{r}'; E_F) \overset{\leftrightarrow}{\partial}_i \sigma^\beta G^A(\mathbf{r}', \mathbf{r}; E_F) \right]. \quad (2.12)$$

In the following discussion, we omit the E_F argument in the Green's function for convenience. Apply the inverse Fourier transform and use $F^{-1}[i\omega \mathbf{m}(\omega)] = d\mathbf{m}(t)/dt$, we arrive at the equation for pumped spin current,

$$j_i^\alpha(\mathbf{r}, t) = \frac{\hbar}{4\pi} \frac{J_{ex} \hbar^2}{2m_e i} \sum_{\beta} \int_{FM} d^3 r' Tr \left[\sigma^\alpha G^R(\mathbf{r}, \mathbf{r}') \overset{\leftrightarrow}{\partial}_i \sigma^\beta G^A(\mathbf{r}', \mathbf{r}) \right] \frac{dm_\beta}{dt} \quad (2.13)$$

When spin-orbit coupling is absent in the picture, the above spinor Green's function can be expressed in terms of spin up/down Green's function,

$$G(\mathbf{r}, \mathbf{r}') = \frac{g_\uparrow(\mathbf{r}, \mathbf{r}') + g_\downarrow(\mathbf{r}, \mathbf{r}')}{2} + \frac{g_\uparrow(\mathbf{r}, \mathbf{r}') - g_\downarrow(\mathbf{r}, \mathbf{r}')}{2} \boldsymbol{\sigma} \cdot \mathbf{m} \quad (2.14)$$

where $g_\uparrow(\mathbf{r}, \mathbf{r}')$ and $g_\downarrow(\mathbf{r}, \mathbf{r}')$ are the Green's functions for the electron with spin parallel or anti-parallel to the magnetization. Expand $\boldsymbol{\sigma} \cdot \mathbf{m} = \sum_{\gamma} m_\gamma \sigma^\gamma$ and insert above Green's function into Eq. (2.13)

$$\begin{aligned} j_i^\alpha(\mathbf{r}, t) &= \frac{\hbar}{4\pi} \frac{J_{ex} \hbar^2}{2m_e i} \sum_{\beta} \int_{FM} d^3 r' \frac{dm_\beta}{dt} \\ &2 \left[\sum_{\gamma} i\epsilon_{\alpha\gamma\beta} m_\gamma g_1^R(\mathbf{r}, \mathbf{r}') \overset{\leftrightarrow}{\partial}_i g_0^A(\mathbf{r}', \mathbf{r}) + i\epsilon_{\alpha\beta\gamma} m_\gamma g_0^R(\mathbf{r}, \mathbf{r}') \overset{\leftrightarrow}{\partial}_i g_1^A(\mathbf{r}', \mathbf{r}) \right. \\ &\left. + \delta_{\alpha\beta} g_0^R(\mathbf{r}, \mathbf{r}') \overset{\leftrightarrow}{\partial}_i g_0^A(\mathbf{r}', \mathbf{r}) - \delta_{\alpha\beta} g_1^R(\mathbf{r}, \mathbf{r}') \overset{\leftrightarrow}{\partial}_i g_1^A(\mathbf{r}', \mathbf{r}) \right] \end{aligned} \quad (2.15)$$

where $g_{0/1}(\mathbf{r}, \mathbf{r}') = [g_\uparrow(\mathbf{r}, \mathbf{r}') \pm g_\downarrow(\mathbf{r}, \mathbf{r}')] / 2$, we find

$$\begin{aligned} j_i^\alpha(\mathbf{r}, t) &= \frac{\hbar}{4\pi} \frac{J_{ex} \hbar^2}{m_e} \sum_{\beta} \int_{FM} d^3 r' \frac{dm_\beta}{dt} \\ &\left[\sum_{\gamma} \text{Re} g_\uparrow^R(\mathbf{r}, \mathbf{r}') \overset{\leftrightarrow}{\partial}_i g_\downarrow^A(\mathbf{r}', \mathbf{r}) \epsilon_{\alpha\gamma\beta} m_\gamma - \delta_{\alpha\beta} \text{Im} g_\uparrow^R(\mathbf{r}, \mathbf{r}') \overset{\leftrightarrow}{\partial}_i g_\downarrow^A(\mathbf{r}', \mathbf{r}) \right] \end{aligned} \quad (2.16)$$

The above results can be rewritten in by introducing a spin conductance Γ ,

$$\mathbf{j}_i(\mathbf{r}, t) = \frac{\hbar}{4\pi} \left[\Gamma_i^{re}(r) \mathbf{m} \times \frac{d\mathbf{m}}{dt} - \Gamma_i^{im}(r) \frac{d\mathbf{m}}{dt} \right], \quad (2.17)$$

with the spin pumping conductance is $\Gamma_i(\mathbf{r}) = \Gamma_i^{re}(\mathbf{r}) + i\Gamma_i^{im}(\mathbf{r})$ and

$$\Gamma_i(\mathbf{r}) = \frac{J_{ex}\hbar^2}{m_e} \int_{FM} d^3r' g_{\uparrow}^R(\mathbf{r}, \mathbf{r}') \overleftrightarrow{\partial}_i g_{\downarrow}^A(\mathbf{r}', \mathbf{r}) \quad (2.18)$$

When compare Eq. (2.17) to Eq. (2.1), it is easy to see the equivalence between Γ defined above and the mixing conductance in scattering theory. The connections will be discussed in next section.

2.3 Results and Discussion

2.3.1 Comparison with Scattering theory in ideal limit

In this section, we explicitly show the calculation of the Green's function for a bilayer and compare our results with Eq. (2.1) derived from the previous scattering approach. For a one-body spin-dependent potential $V_s(z)$, the green's function satisfies

$$\left[E - E_{\parallel} \pm i0^+ + \frac{\hbar^2}{2m_e} \frac{d^2}{dz^2} - V_s(z) \right] g_s^{R/A}(z, z') = \delta(z - z'). \quad (2.19)$$

For layered structure, the above Green's function is solved for each layer with a set of constants of the integration which are subsequently determined via boundary conditions at the interface,

$$g_s^{A/R}(0^+, 0^+) = g_s^{A/R}(0^-, 0^+) = g_s^{A/R}(0^+, 0^-) = g_s^{A/R}(0^-, 0^-). \quad (2.20)$$

and

$$\frac{d}{dz} g_s^{A/R}(z, z') \Big|_{z=0^+} = \frac{d}{dz} g_s^{A/R}(z, z') \Big|_{z=0^-} \quad (2.21)$$

for an arbitrary interface potential without singularity. For a tunneling contact where $V(z) = a\delta(z)$, the last equation is replaced by

$$\frac{d}{dz} g_s^{A/R}(z, z') \Big|_{z=0^+} - \frac{d}{dz} g_s^{A/R}(z, z') \Big|_{z=0^-} = g_s^{A/R}(0, 0) \frac{2m_e a}{\hbar^2}. \quad (2.22)$$

Next, we should analytically calculate the Green's function with a simple model potential of a FM/NM bilayer given below,

$$V_s(z) = \begin{cases} V_0 - sJ_{ex} & z < 0 \\ 0 & z > 0 \end{cases} \quad (2.23)$$

In this case, the solution of Eq. (2.19) can be expressed by the reflection and transmission coefficients [28],

$$g_s^R(z > 0, z' < 0) = -i \frac{m_e}{\hbar^2 k_s} t'_s e^{ikz - ik_s z'} \quad (2.24)$$

$$g_s^R(z < 0, z' > 0) = -i \frac{m_e}{\hbar^2 k} t_s e^{-ikz + ik_\uparrow z'} \quad (2.25)$$

$$g_s^R(z > 0, z' > 0) = -i \frac{m_e}{\hbar^2 k} \left[e^{ik|z-z'|} + r_s e^{ik(z+z')} \right] \quad (2.26)$$

$$g_s^R(z < 0, z' < 0) = -i \frac{m_e}{\hbar^2 k_s} \left[e^{ik|z-z'|} + r'_s e^{-ik(z+z')} \right] \quad (2.27)$$

where t'_s, r'_s are the transmission and reflection coefficients for right going electrons (from FM to NM), t_s, r_s are those for left going electrons, and $k = \sqrt{2m_e(E - E_\parallel)/\hbar}$, $k_s = \sqrt{2m(E - E_\parallel - V_0 + sJ_{ex})/\hbar}$. The advanced Green's function can be calculated from the following relation,

$$g_s^A(z, z') = [g_s^R(z', z)]^* \quad (2.28)$$

Insert these Green's functions into Eq. (2.18) in the main text, we have

$$\Gamma_z(0) = \sum_{k_\parallel} \frac{k_\uparrow + k_\downarrow}{2k_s} t'_\uparrow (t_\downarrow)^* \quad (2.29)$$

Now we are able to compare Eq. (2.29) with the mixing conductance. With the boundary conditions, Eq. (2.20), we have

$$\frac{t'_s}{k_s} = \frac{t_s}{k} = \frac{1 + r_s}{k} = \frac{1 + r'_s}{k_s} \quad (2.30)$$

With Eq. (2.21), we have

$$1 - r_s = \frac{k_s}{k} t_s, \quad (2.31)$$

or for a tunneling contact, Eq. (2.22)

$$- [ik(1 - r_s) - ik_s t_s] = t_s \frac{2m_e a}{\hbar^2}. \quad (2.32)$$

Choose either one of Eq. (2.31) or (2.32) together with Eq. (2.30), one can simplify Eq. (2.29), and prove

$$\Gamma_z(0) = \sum_{k_\parallel} 1 - r_\uparrow r_\downarrow^*; \quad (2.33)$$

this proves that our formalism reduces to that of the scattering formalism in the absence of the interface spin-orbit coupling and diffusive scattering.

2.3.2 Diffusive Contact

The effects of disorders on the spin pumping are not included in the scattering theory while fully encoded in the Green's functions. If the disorder is modeled by a local self energy (similar to the momentum-independent local relaxation time approximation in the Boltzmann equation) such that we may approximate the Green's function as [31]

$$g_{\sigma}^{imp}(\mathbf{r}, \mathbf{r}') = g_{\sigma}^{(0)}(\mathbf{r}, \mathbf{r}')\mathcal{P}_{\sigma}(\mathbf{r}, \mathbf{r}') \quad (2.34)$$

where $g_{\sigma}^{(0)}$ is the Green's function without disorders and

$$\mathcal{P}_{\sigma}(\mathbf{r}, \mathbf{r}') = \exp \left[-\frac{1}{2} \int_{\mathbf{r}'}^{\mathbf{r}} \kappa_{\sigma}(\mathbf{r}'') \hat{\mathbf{n}} \cdot d\mathbf{r}'' \right] \quad (2.35)$$

where $\hat{\mathbf{n}} = (\mathbf{r} - \mathbf{r}') / |\mathbf{r} - \mathbf{r}'|$, the integral is over the direct path from \mathbf{r}' to \mathbf{r} . $\kappa_{\sigma}(\mathbf{r})$ is the inverse of the local mean free path related to the imaginary part of the disorder-induced self-energy $\Delta_{\sigma}(\mathbf{r})$ via $\kappa_{\sigma} = 2m_e\Delta_{\sigma}/\hbar^2k_F$. Equations (2.34) and (2.35) have a very intuitive geometrical interpretation: when the electron travels from the point \mathbf{r}' to \mathbf{r} , the two-point spectral density is reduced by the collision probability. By using Eq. (2.18), we find the spin pumping conductance at the interface is reduced by the impurity scattering

$$\Gamma^{imp}(0) = \frac{J_{ex}^2}{J_{ex}^2 + \Delta^2} \Gamma^0. \quad (2.36)$$

where $\Delta = (\Delta_{\uparrow} + \Delta_{\downarrow})/2$. Eq. (2.36) indicates that the strong scattering (small mean free path) near the interface reduces the spin pumping conductance at the interface.

2.3.3 Numerical Results in Layered Structures

In above derivation, we have calculated the the Green's functions within bilayer structures. In Fig. 2.1, we show some numerical results for spin pumping current, $\Gamma(x)$ in a bilayer structure. Fig. 2.1(a) shows the result of metallic bilayers for two different exchange parameters. As expected, the spin current in the ferromagnetic layer only exists in the vicinity of the interface. As the spin pumping current is polarized perpendicular to magnetization, of which the relaxation is dominated by the dephasing due to exchange interaction. The oscillation and decay length of the spin current can be estimated by $\frac{1}{k_{F\uparrow} - k_{F\downarrow}}$ for a spherical Fermi Surface. In previous spin transfer torque studies, such spin dephasing length is estimated to be 1-2 nm [32]. Also, we see the influence of exchange strength on the spin pumping current is not significant. When we increase J_{ex} from 0.5 eV to 5 eV the spin pumping current only alters by

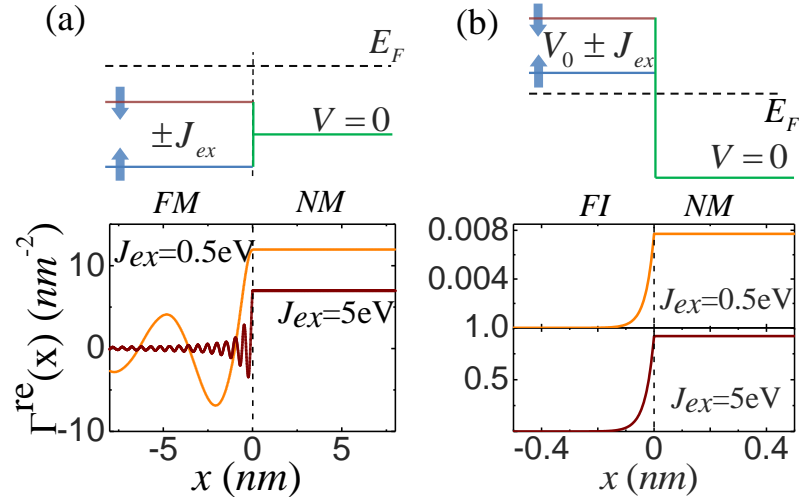


FIGURE 2.1. The position-dependence of the real part of the spin pumping conductance for two magnetic (FM)/non-magnetic (NM) bilayers. (a) Both magnetic and non-magnetic layers, whose spin-dependent potentials are shown above, are metallic. (b) The magnetic layer is a ferromagnetic insulator (FI) and the non-magnetic is a metal. The spin-dependent potentials are also shown ($V_0 - E_F = 9$ eV). The Fermi energy is $E_F = 6$ eV, and the exchange parameters are $J_{ex} = 0.5$ and 5.0 eV as marked in the Figure.

a factor of 2. Such result can be understood by combining the result of scattering theory and our discussion about the diffusive contact. In the mixing conductance definition, the mixing conductance equals to Sharvin Conductance when J_{ex} is close to zero so that one should not expect large influence of J_{ex} on spin pumping. Our Green's function results suggest that it is only true when J_{ex} outweighs the electron self energy. Thus, increasing the J_{ex} from 0.5 to 5 eV still changes the current while only by a relative small amount.

Also, the spin current in this calculation is a constant which is due to the absence of spin relaxation in our picture. It will be fixed in later chapters when we include the back flow spin current from NM layer to FM layer.

In Fig. 2.1(b), we show the similar results for spin pumping from a ferromagnetic insulator. When compared to the metallic case, two differences can be concluded at the first glance. First, the spin current in ferromagnetic layer decrease exponentially instead of with oscillation as the spin current is now tunneling into the FM layer rather than dephasing. For the same reason, the decay length also becomes much

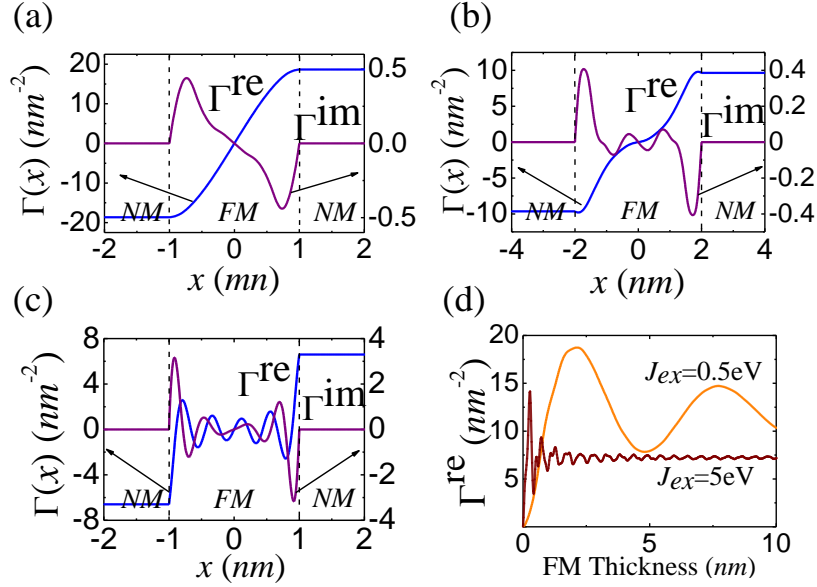


FIGURE 2.2. Real and imaginary parts of the spin pump conductance of the FM layer sandwiched by two semi-infinite non-magnetic metal layers, NM/FM/NM. The Fermi level $E_F = 6 \text{ eV}$ and the thickness of the FM layer is $2d$. (a) $J_{ex} = 0.5 \text{ eV}$, and $2d = 2 \text{ nm}$. (b) $J_{ex} = 0.5 \text{ eV}$, and $2d = 4 \text{ nm}$. (c) $J_{ex} = 5.0 \text{ eV}$, $2d = 2 \text{ nm}$. (d) The dependence of the real part of the spin pumping conductance at the interface on ferromagnetic layer thickness for two different J_{ex}

shorter. Second, the magnitude of spin pumping current now sensitively depends on the strength of exchange coupling between conduction electrons and magnetization.

We now calculate the spin current in a trilayer structure. In Fig. 2.2, we show the spin pumping in a trilayer structure with several different parameters. In Fig. 2.2(a) and (b), we calculate $\Gamma(x)$ for a small exchange coupling and two different FM layer thicknesses. The result shown in Fig. 2.2(c) is for a large exchange coupling for a thin FM film. It can be concluded from the numerical results that the real part of $\Gamma(x)$ always dominates over the imaginary part beyond the FM layer. And both the real and imaginary part oscillates within the FM layer. In Fig. 2.2(d), we show the how the real part of $\Gamma(x)$ at the interface depends on the FM layer thickness. It vanishes for small zero FM layer thickness since $\Gamma(x)$ is anti-symmetric over the FM layer. The oscillating trend for $\Gamma(x)$ over FM layer thickness is also reported in [33].

2.4 Experiments Demonstration of Spin Pumping

Since the discovery of spin pumping in metallic bilayer in 2002, spin pumping experiments has been studied in many different materials including heavy metal [38–44], semi-conductors [45–47] and topological insulators [15, 48, 49]. In all of such systems, the spin-orbit coupling plays a pivot role which is neglected in the scattering theory. After developing the linear response theory, we are capable of taking the interface spin-orbit coupling into consideration [21]. More importantly, we confirm the spin memory loss which is first observed in giant magnetoresistance experiments. Also, the spin memory loss resolves the issues in determining the spin diffusion length of heavy metals [50, 51]. Spin pumping is usually experimentally detected via enhanced Gilbert damping and inverse spin Hall voltage. Here we briefly discuss the experiments and the controversies between results published by different groups. To start, we consider the spin pumping in a metallic bilayer. For convenience, we still use the mixing conductance which is identical results before we take spin-orbit coupling into consideration. The spin current at the interface, say $x = 0$, from direct spin pumping is,

$$\mathbf{j}_s^{\text{pump}}(0) = g_{\text{mix}} \mathbf{m} \times \frac{d\mathbf{m}}{dt} \quad (2.37)$$

where we have neglect the imaginary part of mixing conductance. If the NM layer is a ideal spin sink, all spin current will be immediately relaxed. While for real material, the spin relaxation is not that fast; Thus, a spin accumulation is built up in the NM layer which leads to a backflow spin current.

$$\mathbf{j}_s^{\text{back}}(0) = g_{\text{mix}} \boldsymbol{\mu} \quad (2.38)$$

The total spin current is the difference between the pumped spin current and the current flows back to the FM layer,

$$\mathbf{j}_s^{\text{tot}}(0) = \mathbf{j}_s^{\text{sp}}(0) - \mathbf{j}_s^{\text{back}}(0) \quad (2.39)$$

Another boundary condition is required to solve the all above unknown variables, $\mathbf{j}_s^{\text{tot}}, \mathbf{j}_s^{\text{back}}, \boldsymbol{\mu}$, where we need the spin diffusion equation within the NM layer. The spin current density in the NM layer is purely diffusive since the spin information is not coupled to any field,

$$\mathbf{j}_s^{\text{tot}}(x > 0) = -D \nabla \boldsymbol{\mu}(x > 0) \quad (2.40)$$

where $D = v_F^2 \tau_m$ is the diffusion constant in the NM layer, v_F is the Fermi velocity and τ_m is the electron momentum relaxation time. Another equation is spin continuity

equation,

$$\frac{\partial \boldsymbol{\mu}(x > 0)}{\partial t} = -\nabla \mathbf{j}_s^{\text{tot}}(x > 0) - \frac{\boldsymbol{\mu}(x > 0)}{\tau_s} \quad (2.41)$$

where the second term is the gradient of spin current and last term refers to the local spin relaxation. Here, τ_s is the spin relaxation time. Above two equations lead to the spin diffusion equation,

$$\frac{d^2 \boldsymbol{\mu}(x > 0)}{dx^2} = \frac{\boldsymbol{\mu}(x > 0)}{\lambda^2} \quad (2.42)$$

where $\lambda = \sqrt{v_F^2 \tau_s \tau_m}$ is the spin diffusion equation (SDE). For a NM thin film $0 < x < t_N$, the spin current density has the form of

$$\mathbf{j}_s^{\text{tot}}(x > 0) = \frac{\mathbf{j}_s(0)}{\sinh t_N / \lambda} \sinh(t_N - x) / \lambda \quad (2.43)$$

such that the spin current at the outer interface vanishes.

Put all above results together, we can rewrite Eq. (3.1) and solve the total spin current density at the interface,

$$\mathbf{j}_s^{\text{tot}}(0) = \frac{1}{1 + \xi} g_{\text{mix}} \mathbf{m} \times \frac{d\mathbf{m}}{dt} \quad (2.44)$$

where $\xi = (g_{\text{mix}} \lambda / D) \coth \frac{t_N - x}{\lambda}$ is the backflow parameter.

2.4.1 Enhanced Gilbert damping

The spin pumping current is generated by magnetization precession which is in turn driven by ferromagnetic resonance. The dynamics of a FM layer is always described by the Landau-Lifshitz-Gilbert equation,

$$\frac{d\mathbf{m}}{dt} = -\gamma \mathbf{m} \times \mathbf{H}_{\text{eff}} - \alpha_0 \mathbf{m} \times \left(\mathbf{m} \times \frac{d\mathbf{m}}{dt} \right) + \frac{g_L}{4\pi M t_F} \mathbf{j}_s \quad (2.45)$$

where α is the Gilbert damping of the ferromagnetic layer itself, which is due to the inhomogeneous broadening and other disorder effects. The last term emerges from the spin transfer torque effect, where M is the magnetization of the film, t_F the FM layer thickness and g_L the Lande factor.

When we plugged in the total spin pumping current we just calculated above, the spin pumping current act as an extra damping term,

$$\alpha = \alpha_0 + \frac{g_L g_{\text{mix}}}{4\pi(1 + \xi) M t_F} \quad (2.46)$$

where the second term denotes the extra damping induced by spin pumping.

2.4.2 Inverse spin Hall voltage

Let's consider the polarization of the spin pumping current. Recall that the magnetization precession is,

$$\mathbf{m}(\mathbf{r}, t) = \theta_F(\mathbf{r}) [m_s \mathbf{e}_z + \delta m (\mathbf{e}_x \cos \omega_0 t + \mathbf{e}_y \sin \omega_0 t)] \quad (2.47)$$

Then the spin pumping current polarization is

$$\mathbf{m} \times \frac{d\mathbf{m}}{dt} = \omega [\delta m^2 \mathbf{e}_z + m_s \delta m (\mathbf{e}_x \cos \omega_0 t - \mathbf{e}_y \sin \omega_0 t)]. \quad (2.48)$$

The second term is an ac spin current which is up to the first order of the precessing magnitude δm , and the first term is of the second order or precessing magnitude but a dc current. The ac current is difficult to measure experimentally [38, 52], so the dc term is mostly studied in spite of the small magnitude.

Recall Eq. (2.44), the dc part of the spin pumping current is

$$j_s^{\text{tot}}(x > 0) = \frac{g_{\text{mix}} \omega \sin^2 \phi}{(1 + \xi) \sinh(t_N/\lambda)} \sinh \frac{t_N - x}{\lambda} \quad (2.49)$$

where the ϕ is the precession angle. Such spin current is flowing in x direction while polarized along z direction. Via inverse spin Hall angle, a electric charge current flowing in y direction is generated. The the total charge current can be calculated

$$I_c = \theta_H \int_0^{t_N} dx j_s^{\text{tot}}(x) = \frac{\theta_H g_{\text{mix}} \omega \sin^2 \phi}{(1 + \xi)} \tanh \frac{t_N}{2\lambda} \quad (2.50)$$

This current can be measured as an electric voltage.

When comparing Eq. (2.50) and (2.46), both the enhanced damping and the electric current/voltage depend on the NM layer thickness. For enhanced damping, the dependence emerges from ξ , while the thickness of electric current emerges from ξ and the extra tanh term. Obviously, of them should have same length scale as λ , which significantly differs from the experiment results. The observed enhanced damping saturates at $t_N = 2$ nm while the charge current signal doesn't saturates until 35 nm [41]. In this chapter, we will first theoretically introduce the effects of interfacial SOC and then discuss how this can resolve above controversies.

2.5 Spin Pumping in the presence of Spin-Orbit Coupling

In Sec. 2.2, we have derived the general formula for spin pumping

$$j_i^\alpha(\mathbf{r}, t) = \frac{\hbar}{4\pi} \frac{J_{ex} \hbar^2}{2m_e i} \sum_\beta \int_{FM} d^3 r' T r \left[\sigma^\alpha G^R(\mathbf{r}, \mathbf{r}') \overset{\leftrightarrow}{\partial}_i \sigma^\beta G^A(\mathbf{r}', \mathbf{r}) \right] \frac{dm_\beta}{dt} \quad (2.51)$$

In Chapter 2, we show the application of the above formula when the spin-orbit coupling is absent in the system. In the earlier case, the Green's function is diagonal in the spin space,

$$G^0(\mathbf{r}, \mathbf{r}') = \frac{g_\uparrow(\mathbf{r}, \mathbf{r}') + g_\downarrow(\mathbf{r}, \mathbf{r}')}{2} + \frac{g_\uparrow(\mathbf{r}, \mathbf{r}') - g_\downarrow(\mathbf{r}, \mathbf{r}')}{2} \boldsymbol{\sigma} \cdot \mathbf{m} \quad (2.52)$$

Here, we try to evaluate spin pumping in the presence of SOC interface; in this case the spinor Green's functions are not diagonal in spin space. We consider an interfacial Rashba spin-orbit coupling of the standard form,

$$V(\mathbf{r}) = \alpha_R \delta(z) (\hat{\mathbf{k}} \times \hat{\mathbf{z}}) \cdot \boldsymbol{\sigma}, \quad (2.53)$$

where α_R denotes the Rashba coefficient. There are two essential approaches to include the above Rashba potential in the Green's functions. First, we could introduce an additional term for the boundary condition of the Green's function, i.e., the derivative of the Green's function would have a jump across the interface, similar to Eq. (2.22) for a δ -potential. Matching boundary conditions that entail rotation of spinor Green's functions makes this approach tedious and difficult. An alternative is to treat the Rashba interaction as a perturbation such that the Green's function can be readily obtained as long as we have the Green's function in the absence of the Rashba term. We find the latter approach is simpler and valid up to second order in the Rashba potential. The Green's function may be obtained via Dyson equation [37], $G(\mathbf{r}, \mathbf{r}') = G^0(\mathbf{r}, \mathbf{r}') + \int d^3r_0 G(\mathbf{r}, \mathbf{r}_0) V(\mathbf{r}_0) G(\mathbf{r}_0, \mathbf{r}')$, where G^0 is the Green's function without the spin-orbit coupling.

By using the Dyson equation, the Green's function in the presence of the SOC is

$$G(\mathbf{r}, \mathbf{r}') = G^{(0)}(\mathbf{r}, \mathbf{r}') + \int d^3r_0 G(\mathbf{r}, \mathbf{r}_0) V(\mathbf{r}_0) G^{(0)}(\mathbf{r}_0, \mathbf{r}') \quad (2.54)$$

with $G^{(0)}(\mathbf{r}, \mathbf{r}')$ being a 2×2 matrix defined above. For the bilayer in which the SOC is confined at $z = 0$, we can write the Green's functions in the first and second order perturbation on the SOC parameter α_R ,

$$\begin{aligned} G^{(1)}(z, z') &= \alpha_R G^{(0)}(z, 0) \left[(\hat{k}_\parallel \times \hat{z}) \cdot \boldsymbol{\sigma} \right] G^{(0)}(0, z') \\ G^{(2)}(z, z') &= \alpha_R^2 G^{(0)}(z, 0) \left[(\hat{k}_\parallel \times \hat{z}) \cdot \boldsymbol{\sigma} \right] G^{(0)}(0, 0) \left[(\hat{k}_\parallel \times \hat{z}) \cdot \boldsymbol{\sigma} \right] G^{(0)}(0, z') \end{aligned} \quad (2.55)$$

By placing them into Eq. (2.51), the spin current is

$$\begin{aligned}
& j_z^{(2),\alpha}(z, t) \\
&= \frac{\hbar}{4\pi} \frac{J_{ex} \hbar^2}{2m_e i} \sum_{\beta} \int_{FM} d^3 z' \frac{dm_{\beta}}{dt} \left\{ Tr \left[\sigma^i G^{(1)A}(z, z'; E_F) \overset{\leftrightarrow}{\partial}_z \sigma^{\beta} G^{(1)R}(z', z; E_F) \right] \right. \\
&+ Tr \left[\sigma^{\alpha} G^{(0)A}(z, z'; E_F) \overset{\leftrightarrow}{\partial}_z \sigma^{\beta} G^{(2)R}(z', z; E_F) \right] \\
&+ Tr \left. \left[\sigma^{\alpha} G^{(2)A}(z, z'; E_F) \overset{\leftrightarrow}{\partial}_z \sigma^{\beta} G^{(1)R}(z', z; E_F) \right] \right\} \quad (2.56)
\end{aligned}$$

After we express the Green's functions in terms of the unperturbed $g_{\uparrow/\downarrow}(z, z')$, e.g.,

$$\begin{aligned}
& G^{(1)}(z, z')/\alpha_R \\
&= g_0(z, 0)g_0(0, z') \left[(\hat{k}_{\parallel} \times \hat{z}) \cdot \sigma \right] \\
&+ g_0(z, 0)g_1(0, z') \left[(\hat{k}_{\parallel} \times \hat{z}) \cdot \sigma \right] (\sigma \cdot \mathbf{m}) \\
&+ g_1(z, 0)g_0(0, z') (\sigma \cdot \mathbf{m}) \left[(\hat{k}_{\parallel} \times \hat{z}) \cdot \sigma \right] \\
&+ g_1(z, 0)g_1(0, z') (\sigma \cdot \mathbf{m}) \left[(\hat{k}_{\parallel} \times \hat{z}) \cdot \sigma \right] (\sigma \cdot \mathbf{m}). \quad (2.57)
\end{aligned}$$

we find the pumped spin currents at the interface is, up to the second order in SOC,

$$\mathbf{j}_z^{(2)}(z \approx 0, t) = \frac{\hbar}{4\pi} \Gamma^0 \frac{J_{ex}^2}{J_{ex}^2 + \Delta^2} \left[-\text{sign}(z)\eta \left(\mathbf{m} \times \frac{d\mathbf{m}}{dt} \right)_z \hat{z} - 2\eta\Theta(z)\mathbf{m} \times \frac{d\mathbf{m}}{dt} \right] \quad (2.58)$$

with $\eta = \alpha_R^2 k_F^2 / E_F^2$.

After some cumbersome algebra we find to second order in the Rashba coefficient the spin current near the interface can be written in compact form as,

$$\mathbf{j}_z(0^-) = \frac{\hbar}{4\pi} \frac{J_{ex}^2}{J_{ex}^2 + \Delta^2} \Gamma^0 \mathcal{A}_1 \cdot \left(\mathbf{m} \times \frac{d\mathbf{m}}{dt} \right), \quad (2.59)$$

at the FM side of the interface, and

$$\mathbf{j}_z(0^+) = \frac{\hbar}{4\pi} \frac{J_{ex}^2}{J_{ex}^2 + \Delta^2} \Gamma^0 \mathcal{A}_2 \cdot \left(\mathbf{m} \times \frac{d\mathbf{m}}{dt} \right) \quad (2.60)$$

for the NM layer side of the interface. Here Δ is the imaginary part local self-energy due to disorder, Γ^0 the spin pumping conductivity across the interface without disorder, which is the same as the ‘‘mixing conductance’’ in the scattering formalism, and the matrices \mathcal{A}_1 and \mathcal{A}_2 are,

$$\mathcal{A}_1 = \begin{pmatrix} 1 & 0 & 0 \\ 0 & 1 & 0 \\ 0 & 0 & 1 + \eta \end{pmatrix}; \mathcal{A}_2 = \begin{pmatrix} 1 - 2\eta & 0 & 0 \\ 0 & 1 - 2\eta & 0 \\ 0 & 0 & 1 - 3\eta \end{pmatrix}.$$

where $\eta = (\alpha_R k_F / E_F)^2$. From ab-initio calculations the Rashba coefficient has been estimated to be between 0.03 and 3 eVÅ for different systems [53]. Given that the Fermi vector, k_F , is of the order of an inverse Angstrom, η is as large as 0.3 for the systems to be discussed below.

The physical meaning of the diagonal matrices $\mathcal{A}_1, \mathcal{A}_2$ is: without SOC at the interface the spin current is polarized in the direction of $\mathbf{m} \times d\mathbf{m}/dt$ throughout the structure; the Rashba term at an interface makes the spin of the electron rotate about the axis $\hat{z} \times \hat{\mathbf{k}}$. Since this direction is in the plane of a layer, spins polarized parallel and perpendicular to the plane of the layers receive different torques; thus \mathcal{A}_1 and \mathcal{A}_2 are not unit matrices. However, the matrices remain diagonal because the off-diagonal terms vanish after summing over the momentum of conduction electrons. In \mathcal{A}_2 , $1 - 2\eta$ and $1 - 3\eta$ refer to the spin memory loss factor for spin currents flowing across the interface that are polarized parallel and perpendicular to the interface .

Having determined the spin pumping current near an interface, we evaluate the back-scattering or “backflow” of the spin current that reduces the current arising from spin pumping. Consider a boundary condition such that the spin current is zero at the outer boundary of the NM layer; then one can write the spin current in the layer in terms of its value at the interface, i.e., $\mathbf{j}_z(z > 0) = \mathbf{j}_z(0^+) \sinh[(t_N - z)/\lambda_{sd}] / \sinh(t_N/\lambda_{sd})$, where λ_{sd} is the spin-diffusion length. Consequently a spin accumulation $\boldsymbol{\mu}$ is established in the NM layer; this accumulation is polarized transversely to the magnetization of the FM layer. For this reason the spin current backscattered into the FM layer is also polarized transversely to the magnetization of the layer, and decays within a spin coherence length, which for a strong ferromagnet such as Co and Fe is a few monolayers [32], The ensuing difference between spin accumulations in the NM and FM layers creates a bias which drives a diffusive spin current flow towards the FM layer known as the “backflow” due to spin pumping [54]. In previous approaches without SOC, backflow was accounted for by introducing the mixing conductance across the interface. Here, we include backflow by using Eq. (3) where the source term, the magnetization dynamics in the FM layer, is replaced by the spin accumulation $\boldsymbol{\mu}(\mathbf{r})$ in the NM layer, i.e.,

$$j_z^{\alpha,back}(\mathbf{r}) = \frac{\hbar}{2m_e i C} \sum_{\beta} \int_{NM} d^3\mathbf{r}' Tr[\sigma^{\alpha} G^R(\mathbf{r}, \mathbf{r}'; E_F) \overset{\leftrightarrow}{\partial}_z \sigma^{\beta} G^A(\mathbf{r}', \mathbf{r}; E_F)] \mu_{\beta}(\mathbf{r}'). \quad (2.61)$$

where $C = (\frac{m_e}{\hbar^2})^2 l_m$ is a normalization factor, and l_m the mean free path. By using calculations similar to those leading to Eqs. (2.59) and (2.60), the backflow spin

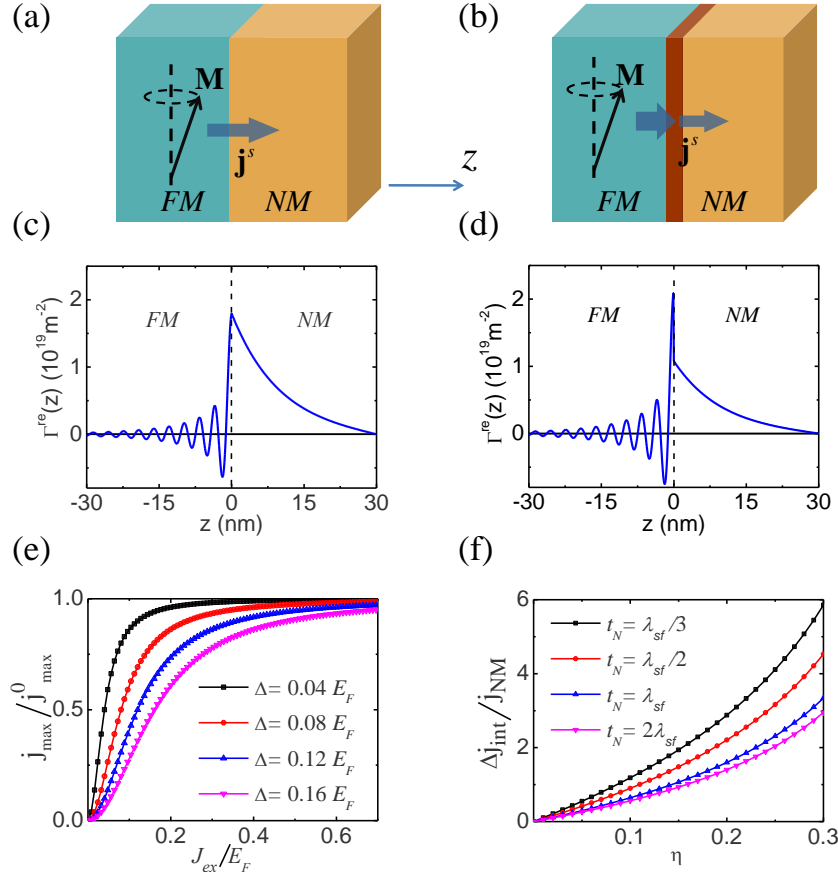


FIGURE 2.3. Illustration of spin pumping (a) without and (b) with Rashba SOC at the interface. In both cases, (c) and (d), the spin current decays oscillatorily within FM layer and exponentially in the NM. The maximum spin current j_{max} occurs at $z = 0^-$. The dependence of j_{max} , normalized to its disorder-free value j_{max}^0 , on the ferromagnetic exchange constant for several values of the disorder parameter Δ , (e), where Δ is the imaginary part of self energy. The ratio of the interface spin current jump Δj_{int} to the spin current relaxed in the NM layer as a function of the SOC strength for several thickness of the NM layer, (f) (in plane spin polarization).

current across an interface is,

$$\mathbf{j}_z^{back}(0^-) = -\frac{\hbar}{2m_e k_F} \Gamma^0 \mathcal{A}_2 \cdot \boldsymbol{\mu}(0^+), \quad (2.62)$$

$$\mathbf{j}_z^{back}(0^+) = -\frac{\hbar}{2m_e k_F} \Gamma^0 \mathcal{A}_1 \cdot \boldsymbol{\mu}(0^+). \quad (2.63)$$

By combining currents due to the spin pumping, backflow, and diffusive current

in the NM layer we finally arrive at the spin pumping current for the FM/NM bilayer. In the NM layer

$$\mathbf{j}_z(z > 0) = \frac{\hbar\Gamma^0}{4\pi} \frac{J_{ex}^2}{J_{ex}^2 + \Delta^2} N(z) \mathcal{A}_N \cdot \left(\mathbf{m} \times \frac{d\mathbf{m}}{dt} \right), \quad (2.64)$$

where $N(z) = \sinh[(t_N - z)/\lambda_{sd}] / \sinh(t_N/\lambda_{sd})$; in the FM layer

$$\mathbf{j}_z(z < 0) = \frac{\hbar\Gamma^0}{4\pi} \frac{J_{ex}^2}{J_{ex}^2 + \Delta^2} F(z) \mathcal{A}_F \cdot \left(\mathbf{m} \times \frac{d\mathbf{m}}{dt} \right), \quad (2.65)$$

where $F(z)$ is 1 at $z = 0$ and has an oscillatory decay in the FM layer. The matrices \mathcal{A}_N and \mathcal{A}_F are

$$\mathcal{A}_N = \frac{1}{1 + \xi} \begin{pmatrix} 1 - 2\eta & 0 & 0 \\ 0 & 1 - 2\eta & 0 \\ 0 & 0 & 1 - 3\eta - \frac{\xi\eta}{1 + \xi} \end{pmatrix};$$

$$\mathcal{A}_F = \frac{1}{1 + \xi} \begin{pmatrix} 1 + 4\eta\xi & 0 & 0 \\ 0 & 1 + 4\eta\xi & 0 \\ 0 & 0 & 1 + 8\eta\xi + \frac{\eta}{1 + \xi} \end{pmatrix}.$$

where the *backflow factor* $\xi = (3/2)(\Gamma^0/k_F^2)(\lambda_{sd}/l_m) \coth(t_N/\lambda_{sd})$, ranges between zero and infinity. $\xi = 0$ refers to the case where's no backflow; then \mathcal{A}_F , \mathcal{A}_N reduce to \mathcal{A}_1 , \mathcal{A}_2 . $\xi = \infty$ indicates that the entire spin current pumped into the NM bulk flows back across the interface; then \mathcal{A}_N vanishes and \mathcal{A}_F is proportional to η which means that the entire spin current is relaxed at the interface.

Equations (2.64) and (2.65) are our main results. In Fig. 2.3, we show the spin current in the FM/NM bilayer for various values of the disorder, SOC strength, and thickness of the NM layer. We conclude by discussing the salient features of the dependence of spin pumping on these parameters and relate our results to existing data.

1) Spin memory loss and spin current absorption at interfaces. The loss of spin current at Cu/Pt interfaces was proposed more than a decade ago. H. Kurt *et al.* [55] observed in their CPP GMR study that the spin current across a Cu/Pt interface is not continuous. More quantitatively, if the standard spin diffusion equations are used to fit the data of magnetoresistance, a spin memory loss parameter, as large as 90%, at the Cu/Pt interface has to be introduced. The spin memory loss cannot be due to strong spin flip scattering in the Pt layer since the measured spin diffusion length of Pt remains relatively long at 14nm. We consider such spin memory loss

as the experimental evidence of the strong interfacial SOC. Another experimental support of the loss of spin current at interfaces is the observation that enhanced damping due to spin pumping saturates at just a few monolayers of Pt grown on FM films [41], i.e., a thicker Pt layer does not increase the damping since the spin current is mainly lost to the interface. These experiments support our idea that the SOC at interfaces that absorbs a significant portion of the spin current; quantitative estimates for the loss are determined from Eqs. (2.64) and (2.65) as long as the Rashba coefficient is known.

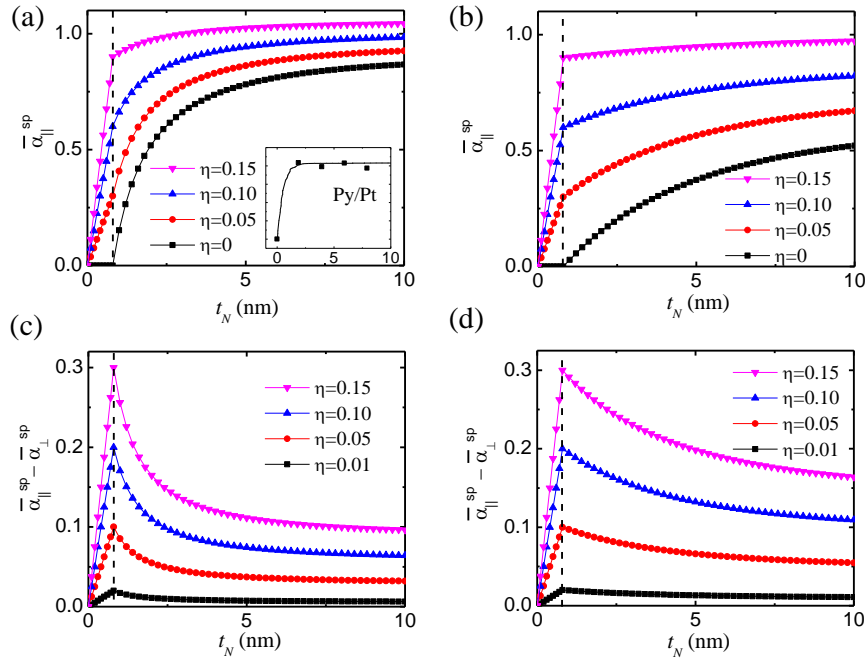


FIGURE 2.4. The enhanced damping parameter and its anisotropy of spin pumping for several different SOC parameters. (a) The precessing axis is parallel to the layers with the backflow fraction at large NM thickness $\epsilon \equiv \xi/(1 + \xi) = 10\%$, and (b) $\epsilon = 40\%$. The dashed lines indicate the effective thickness of the interface. (c) The difference of the enhanced damping parameter for the precessing axis perpendicular and parallel to the layers for $\epsilon = 10\%$, and (d) $\epsilon = 40\%$. The inset in (a) is from the experimental data in ref. [41].

2) Dependence of the spin current on disorder. Yoshino *et al.* have investigated the dependence of the enhanced damping on the composition of the ferromagnetic alloy $\text{Fe}_x\text{Ni}_{1-x}$ [56]. It was found that the induced electric voltage scales

with the average saturation magnetization of the alloy. In our sd model, the saturation magnetization is proportional to the exchange parameter J_{ex}^2 , and thus the spin pumping current, Eq. (2.64) and (2.65), which is proportional to the enhanced damping parameter, does predict such dependence in the limit of a strong disorder. In the previous spin pumping theory [25], the mixing conductance is independent of the alloy composition.

3) Resolving the controversy between short and long spin diffusion length.

Currently there is a lively debate on the spin diffusion length of Pt [39–44]. In FMR experiments, the thickness dependence of the damping constant leads to a short length, typically a few monolayers, while the inverse spin Hall effect presages a much longer spin diffusion length for Pt. This discrepancy is resolved by noting that the damping enhancement of FMR is mainly associated with absorption of spin current at the interface, while the inverse spin Hall effect measures the spin current in the bulk of the Pt layer. Our formalism, Eqs. (2.64) and (2.65), provides a natural explanation for the different length scales found from different experiments.

4) Anisotropy of enhanced damping. Another prediction from Eqs. (2.64) and (2.65) is the anisotropy of the pumping current depending on whether the axis for the precessing magnetization is in or perpendicular to the plane of a layer. If we define the enhanced damping parameter as the loss of spin current at the interface and in the NM bulk, we find,

$$\alpha_{\perp} \propto \frac{1 + 4\eta\xi}{1 + \xi} \quad (2.66)$$

$$\alpha_{\parallel} \propto \frac{1 + 6\eta\xi}{1 + \xi} + \frac{\eta}{2(1 + \xi)^2} \quad (2.67)$$

The in-plane damping is always larger than that of the out-of-plane. Early experiments overlooked this anisotropy. In Fig. 2.4, we show the anisotropy of the enhanced damping as the parameters are varied.

5) Inverse spin Hall from the FM layer. Eq. (2.65) explicitly determines the spin current in the FM layer. We are unable to analytically write down the expression for the position dependence of $F(z)$ due to different Fermi surfaces in different materials. However we can estimate the average spin current, $I_F^t \equiv (1/t_{FM}) \int_{-\infty}^0 dz \mathbf{j}(z)$, in the FM layer by approximating $F(z)$ as an oscillatory decaying function with a period of $L_{co} = 2\pi/(k_{F\uparrow} - k_{F\downarrow})$; it follows that $I_F^t \approx L_{co} j(0^-)$. The inverse spin Hall in the FM layer converts the spin current into a voltage V_{ISHE} proportional to I_F^t . Such a voltage has recently been observed in NiFe/YIG bilayers [57].

Finally, we wish to comment that our theory may also be applied to study the

spin pumping in ferromagnetic and topological insulator bilayers. A spin pumping induced robust spin Hall voltage has already observed in NiFe/Ag/Bi [15] and NiFe/BiSbTeSe [48]. A possible explanation is that the spin pumping induces a large spin accumulation near the surface of the topological insulator, and a conversion between the spin accumulation and electric current occurs at the momentum-spin locked surface [14]. We point out that a more quantitative treatment of spin accumulation and induced current on the surface of TI's would have to include the coupling between the 2-dimensional TI states and 3-d metallic states; this requires a separate study.

2.6 Spin Pumping induced Electric Voltage

In above section, we proved that the interface Rashba SOC leads to spin memory loss, which explains the reason why the enhanced Gilbert damping saturates at a small NM layer thickness. In this section, we discuss the effects of interface SOC on the induced electric voltage.

2.6.1 Spin pumping induced electric voltages

As both spin currents absorbed by the interface RSOC and by the spin diffusion in the NM layer would enhance the damping of the FM precession, they also contribute to the electric voltage. In the NM layer, the injected spin current converts to a charge voltage via ISHE which may be parameterized by the spin Hall angle θ_{SH}^N ,

$$V_N = \frac{\theta_{SH}^N e L \Gamma_{eff}^N f \sin^2 \phi \lambda_{sd}}{\sigma_N t_N + \sigma_F t_F} \tanh \frac{t_N}{2\lambda_{sd}} \quad (2.68)$$

where we have averaged over a precession period so that the above signal is a dc voltage; in the above equation, ϕ is the FM precession angle, L is the length of the bilayer along y direction, f is the precession frequency, $\sigma_{N(F)}$ is the conductivity of the NM (FM) layers, $t_{N(F)}$ is the thickness of the NM (FM) layer and $\Gamma_{eff}^N = \Gamma(0)(1 - \epsilon)(1 - \delta)$ is the effective spin pumping conductance. Note that Γ_{eff}^N reduces to the conventional spin mixing conductance if there is no interface SOC ($\delta = 0$). The induced charge voltage from the FM layer is

$$V_F = \frac{\theta_{SH}^F e L \Gamma_{eff}^F f \sin^2 \phi l_F}{\sigma_N t_N + \sigma_F t_F} \quad (2.69)$$

where $l_F \equiv \int_{-\infty}^0 dz F(z)$ can be related to the transverse coherence length, $l_F \approx \lambda_c$, and $\Gamma_{eff}^F = \Gamma(0) [1 - (1 - \delta)^2 \epsilon]$. Since the coherence length in FM layer is usually

much smaller than the spin diffusion length [32], the voltage signal contributed from the FM layer is one to two orders of magnitude smaller compared to that from the NM layer.

The electric voltage contributed from the interface is modeled by the inverse Edelstein effect [14, 15]. The spin current absorbed by the interface would convert into a spin accumulation of the interface layer which in turn creates a non-equilibrium charge current; this is the inverse process of the electric current induced spin accumulation in a 2d Rashba electron gas [13]. A simple relation between the charge current and spin current loss can be established within the constant relaxation time τ approximation,

$$j_e = \frac{\alpha_R \tau}{\hbar} [j_F(0) - j_N(0)]. \quad (2.70)$$

This is known as the inverse Edelstein effect and one may define an inverse Edelstein length $\lambda_{IEE} \equiv \alpha_R \tau / \hbar$ [14, 15]. The physical meaning is that the spin relaxation in the Rashba interface equals the rate of the spin current pumping at the steady state condition. By using the resistance-in-parallel model, one immediately finds the contribution of the electric voltage from the interface,

$$V_{Int} = \frac{\lambda_{IEE} e L \Gamma(0) \delta(1 + \epsilon - \delta\epsilon) f \sin^2 \phi}{\sigma_N t_N + \sigma_F t_F}. \quad (2.71)$$

When the layer thickness is comparable to the mean free path, we use the thickness dependent conductivities, see below.

2.7 Results and discussions

Our central result is that the induced electric voltage comes from all three regions—the FM layer, the NM layer and the interface. The total electric voltage is thus the summation of Eqs. (2.68), (2.69) and Eq. (2.71),

$$V = V_F + V_N + V_{Int}. \quad (2.72)$$

While V_F is generally smaller than the other two, it could be important when the other two are absent. For example, for NiFe/YIG bilayer where YIG is an insulator and thus $V_N = 0$. Also, one expects that the RSOC is much smaller than that of NiFe/Pt interface and therefore V_{Int} is small. Indeed, Hyde *et al.* [57] had observed that the induced electric voltage in NiFe/YiG comes from the NiFe layer. In the following, we only consider metallic bilayers such as NiFe/Pt and will discard V_F in our numerical calculations.

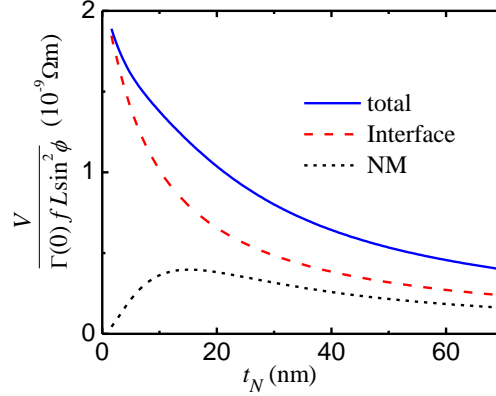


FIGURE 2.5. NM layer thickness dependence of the electric voltage calculated from Eq. (2.68) and (2.71). The parameters are: $\theta_{SH}^N = 0.1$, $\lambda_{IEE} = 0.06nm$, $\lambda_{sd} = 7.7nm$ and $\delta = 0.9$, $\sigma_F = 3.3 \times 10^6 \Omega^{-1}m^{-1}$, $t_F = 10nm$. The spin diffusion length used here is the value from ref. [40].

To apply Eqs. (2.68) and (2.71) to experimental systems, one needs to have a reasonable estimate on all parameters. We choose these parameters either from the experimental data or from “consensus” theoretical assumptions. In Figure 2.5, we show the bulk and interface contributions to the electric voltage as well as their sum. The parameters are indicated in the figure caption. A particular choice of a large RSOC of $\delta = 90\%$ was in accordance with the experimental result that a spin memory loss of NiFe/Pt interface is about 90% as far as the spin transport is concerned [55]. The backflow parameter is taken as about 50%. The conductivity of the bilayer entering the denominator of Eqs. (2.68) and (2.71) is modeled by the limiting value of Fuchs-Sondheimer theory in which the thickness dependence of the Pt conductivity is approximated by,

$$\rho(t_N) = \rho_\infty \left[1 + \frac{3l}{8(t_N - h)} \right] \quad (2.73)$$

where l is the mean free path in bulk and h is the interface roughness; we have chosen these parameters from ref. [58], $h = 0.8nm$, $l = 4.1nm$, $\rho_\infty = 3.28 \times 10^7 \Omega m$. Clearly, with the choice of the parameters given in Fig. 2.5, the interface contribution to the electric voltage is generally larger than that of the bulk.

Prior to our work, the spin pumping induced electric voltage is exclusively analysed via the ISHE. We believe that the omission of the interface contribution to the electric

voltage is the origin of a few erroneous conclusions. First, the experimental fit to the enhanced damping parameters and the induced electric voltage often contradicted each other in terms of the spin diffusion length. Some results are unphysical since the spin diffusion length derived from fitting to the bulk ISHE is much smaller than the mean free path. Due to the co-existence of the interface and bulk contribution, the single exponential fit on the thickness dependence of the NM layer used in the early fitting procedure is doomed to fail. Second, the backflow parameter ϵ is not consistent with the reasonable choice of parameters. Often, an extra-large value of the backflow is needed for better fitting [40, 111]; this is incompatible with the notion that Pt is a good spin sink and ϵ is small. Third, recent experiments have in fact showed that the electric voltage can be induced by spin pumping without a NM layer as a spin sink [15, 57].

In Fig. 2.5, we compare our calculated results with the experimental data from ref. [40] by using our Eq. (11). In our calculation, we considered the elliptical magnetization dynamics to compare with experiment. Since in real experiments, the precession orbit is no more a circle due to the contribution to the effective field from the ferromagnet magnetization [61]. We use the experimental values of the thickness dependent conductivity, $\sigma_{N(F)} = 4.1(3.5) \times (1 - e^{t_{N(F)}/29.6(9.8)}) \times 10^6 \Omega^{-1} m^{-1}$, in order to reduce the uncertainty of the model parameters. Interestingly, the dependence of the electric voltage on the FM layer thickness shows non-monotonic behavior; this is due to 1) the precession angle generated by a fixed power microwave source is inversely proportional to the thickness of the FM layer, and 2) the conductance of the bilayer increases with the thickness of the FM layer. With the best fit, we have used the microwave frequency magnetic field $\mu_0 h_{rf} = 1.7 \times 10^{-4} T$ which is directly related to the precession angle, where μ_0 is the vacuum permeability. The spin diffusion length is found to be $\lambda_{sd} = 11.8$ nm; this is the longest value reported recently. The inverse Edelstein length for NiFe/Pt interface is $0.055 nm$, smaller than the recent result for NiFe/Ag/Bi multi-layers [14, 15].

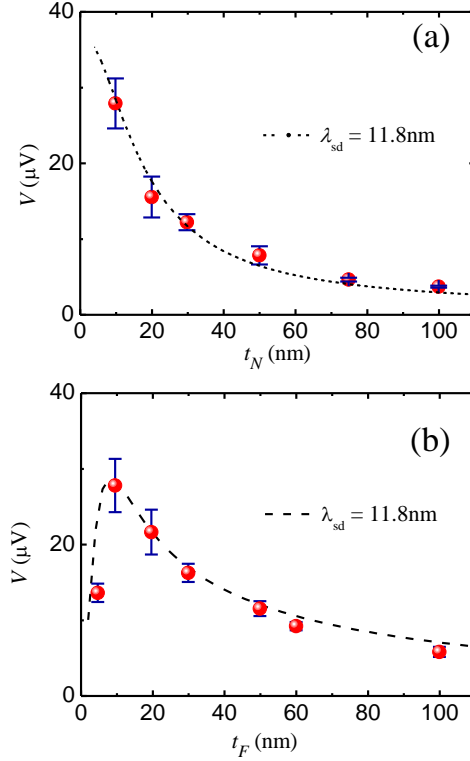


FIGURE 2.6. The comparison of the thickness dependence of the electric voltage between our theory and experiments of Nakayama *et al.* [40]. In our calculation, we used the values $L = 1.6 \text{ mm}$, $f = 9.44 \text{ GHz}$, $\mu_0 M s = 0.72 T$ which are from ref. [40]. We use $\delta = 0.9$ as the interface spin memory loss. With the best fit, we find $\theta_{SH}^N = 0.035$, $\lambda_{sd} = 11.8 \text{ nm}$, $\mu_0 h_{rf} = 1.7 \times 10^{-4} T$, $\Gamma(0) = 3.02 \times 10^{19} \text{ m}^{-2}$, $\lambda_{IEE} = 0.055 \text{ nm}$. (a) dependence on the FM layer thickness for a fixed $t_N = 10 \text{ nm}$, and (b) dependence on the NM layer for a fixed t_F .

CHAPTER 3

SPIN HALL MEASUREMENT IN SPIN PUMPING AND SPIN TRANSFER TORQUE

Spin Hall angle characterizes the efficiency of spin-charge current conversion and it has become one of the most important material parameters for spintronics physics and device application. A long standing controversy is that the spin Hall angles for a given material measured by the spin pumping and by the spin Hall torque experiments are inconsistent and they could differ as large as an order of magnitude. By using the linear response spin transport theory, we explicitly formulate the relation between the spin Hall angle and measured variables in different experiments. We find that the non-local conductivity inherited in the layered structure plays a key role to resolve conflicting values of the spin Hall angle. We provide a generalized scheme for extracting spin transport coefficients from experimental data.

3.1 Experiments Measurement of spin Hall angle

Spin Hall (SH) and inverse spin Hall (ISH) effects provide an efficient way to convert charge-to-spin and spin-to-charge currents [3, 4]. Spin Hall angle θ_H quantitatively characterizes the conversion efficiency: SH yields a spin current $j_s = \theta_H(\hbar/2e)j_e$ from the applied electric current density j_e , and ISH generates an electric current $j_e = \theta_H(2e/\hbar)j_s$ from the injected spin current j_s . Since there is no “spin current meters” to directly measure the spin current, one relies on indirect measurement in which the spin current produces some measurable consequences. The first measurement of the SH effect was achieved via optical Keer effect where spin accumulation at the edge of the sample is detected [62], but electrical methods are more desirable for nanostructure. Spin transfer torques (STT) [63–71] and ISH voltage [39–42, 72, 73] from spin pumping (SP) or spin Seebeck (SS) are two established electrical measurements of the spin current. Both methods are based on a bilayer structure made of a ferromagnetic (FM) layer and a non-magnetic (NM) layer. Typically, the non-magnetic layer is a heavy metal or a topological layer of which the spin Hall angle is measured. In STT, an applied in-plane charge current in the heavy metal converts to the spin current flowing perpendicularly to the layers, and subsequent spin current absorption

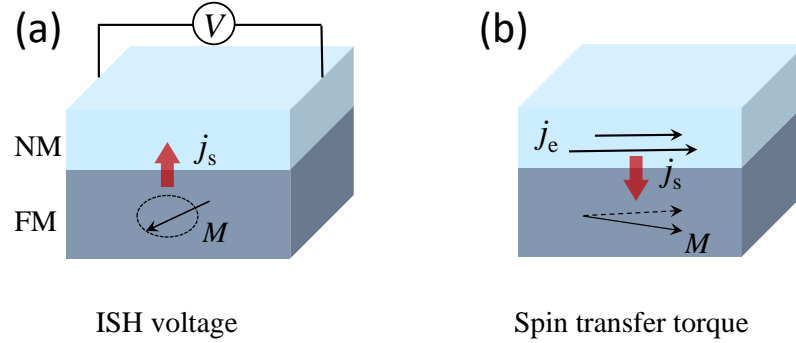


FIGURE 3.1. Illustration of spin Hall measurement. (a) A precessing magnetic layer pumps the spin current into the heavy metal. An electric field (or a charge voltage) from the ISH effect is measured. (b) An applied in-plane electric current accompanies a spin current flowing perpendicular to the layer due to SH effect. The spin current exerts a torque on the ferromagnetic layer which is being measured. The table of the spin Hall angles shows a wide range of values for these two classes of measurement.

creates a spin torque on the ferromagnetic layer. Thus, the spin Hall angles are determined through the measurement of the current-induced spin torque. In ISH voltage measurement, a spin current is generated by either the spin pumping from the precessing ferromagnetic layer or by a thermal gradient in the magnetic layer. The spin current injected to the heavy metal by SP or SS subsequently converts to an electric charge current in the plane of the layer, yielding a measurable voltage. While both methods have been widely studied for different materials, the experimentally deduced values of θ_H have consistently differed by a large margin, from several tens to a few hundred percentage, see Table 3.1 for the experimental data from literature.

In spite of extensive measurement for materials such as Pt, W, Ta, there is no consensus agreement on the proper value of the spin Hall angle due to apparently conflicting results among experimental groups. In this letter, we theoretically formulate the relation between the spin Hall angle and the measured variables of the above experimental measurements. As the layer thickness of the experimental bilayers are often of the order of the electron mean free path, we find the non-local conductivity in these experiments plays crucial roles, and thereby significant corrections to the previously claimed spin Hall angles in different experiments are required.

TABLE 3.1. Spin Hall angles reported by inverse spin Hall voltage and spin transfer torque experiments.

Heavy Metal	θ_H from ISH	θ_H from STT
Pt	0.012 [41], 0.013 [40], 0.013 [39], 0.027 [42], 0.03 [72], 0.08 [73], 0.1 [74]	0.04 [68], 0.08 [63], 0.19 [67]
Ta	-0.02 [72], -0.07 [74]	-0.15 [69], -0.2 [66]
W	-0.14 [74]	-0.2 [70], -0.3 [64], -0.5 [71]

3.2 Role of non-local spin Hall conductivity

3.2.1 Role of None Local Conductivity in Spin Hall Measurement

We start with the ISH method (spin pumping or spin Seebeck) in which a spin current j_s is injected from the ferromagnetic layer to the heavy metal. By considering the process of the spin diffusion and spin current backflow, the spin current in the heavy metal decays as $j_s(z) = j_s(0) \sinh[(d_N - z)/\lambda_s] / \sinh(d_N/\lambda_s)$ where $j_s(0)$ is the spin current density at the interface and λ_s is the spin diffusion length and d_N is the thickness of the NM layer [39]. The spin current yields an in-plane electric field $E_{sh}(z) = \theta_H \rho_N j_s(z)$ where ρ_N is the resistivity of the *bulk* heavy metal; for simplicity we take $\hbar = e = 1$ so that the unit of spin current is same as that of the charge current. The use of the bulk value of the resistivity indicates that θ_H is defined as to the spin Hall angle of the bulk. This electric field drives an electric current in the plane of the layers (CIP) and a charge accumulation at the sample boundary is built-up in the steady state, resulting in a *measured* electric field E_m . The total electric field, $E_{sh}(z) + E_m$, must satisfy the open boundary condition, i.e., the total electric current is zero,

$$\int_{-d_F}^{d_N} j_e(z) dz = \int_{-d_F}^{d_N} dz \int_{-d_F}^{d_N} dz' \sigma_{||}(z, z') [E_m + E_{sh}(z')] = 0 \quad (3.1)$$

where $\sigma_{||}(z, z')$ is the in-plane two-point conductivity tensor of the bilayer. Solving for the measured electric field from the above equation, we have

$$E_m = G_t^{-1} \rho_N \theta_{sh} \int_0^{d_N} dz \sigma_{||}(z) j_s(z) \quad (3.2)$$

where $\sigma_{||}(z) = \int dz' \sigma_{||}(z, z')$ is the position-dependent conductivity, $G_t = \int \sigma_{||}(z) dz$ is the total conductance, and we assume the ISH current only exists in the heavy metal. While the total conductance of the bilayer G_t can be experimentally measured and the spin current $j_s(z)$ has been indirectly measured via the enhanced damping parameter [39], the position-dependent conductivity $\sigma_{||}(z)$ is needed in order to determine θ_H from the measured electric field E_m . At present, the experimental data were fitted to the above equation by taking the conductivity by the bulk value, i.e., $\sigma_{||}(z) = \rho_N^{-1}$, i.e., the spin Hall angle was simply fitted by $\theta_H^0 = \rho_N^{-1} G_t \bar{j}_s$ where \bar{j}_s is the average current density in the heavy metal. Thus, the ratio R of the spin Hall angle θ_H from Eq. (3.2) and θ_H^0 of the previous value for a given experimentally measured value E_m is

$$R \equiv \frac{\theta_H}{\theta_H^0} = \frac{\int_0^{d_N} \sinh[(d_N - z)/\lambda_s] dz}{\rho_N \int_0^{d_N} \sigma_{||}(z) \sinh[(d_N - x)/\lambda_s] dz} \quad (3.3)$$

Clearly, $\sigma_{||}(z)$ from the two-point conductivity tensor in the bilayer includes the scattering from the interfaces and it could be much smaller than that of the conductivity of the bulk materials ρ_N^{-1} when the thickness of the layer is comparable or smaller than the mean free path. Thus, the spin Hall angle determined previously by the SP or SS was significantly underestimated, particular for those structure with a thin layer thickness.

Next we consider whether a similar correction is needed for the measurement of the spin Hall angle by the STT. When an external electric field E_0 applied in the plane of the layer, a non-uniform charge current $j_e(z) = \int dz' \sigma_{||}(z, z') E_0 dz' \equiv \sigma_{||}(z) E_0$ generates a spin Hall electric field $E_s(z) = \theta_H \rho_N j_e(z)$ that drives a spin current perpendicular to the plane of the layers (CPP). The spin current then generates a spin accumulation $\mu_s(z)$ so that the effective spin electric field $E_s^{\text{eff}}(z)$ is

$$E_s^{\text{eff}}(z) = \theta_H \rho_N j_e(z) - \frac{d\mu_s}{dz}. \quad (3.4)$$

The linear response relation, $j_s(z) = \int \sigma_{\perp}(z, z') E_s^{\text{eff}}(z') dz'$, where $\sigma_{\perp}(z, z')$ is the two point conductivity for the CPP, should be used to self-consistently solving for $E_s^{\text{eff}}(z')$. In a previous study of the CPP spin transport, an approximate solution could be obtained when the spin diffusion length is much longer than the mean free path [75]: briefly, we invert the response function by writing $E_s^{\text{eff}}(z) = \int \rho_s(z, z') j_s(z')$ and note that $j_s(z)$ varies with the length scale of spin diffusion length while the resistivity tensor $\rho_s(z, z')$ varies within the mean free path. We integrate over ρ_s , which yields

a local resistivity ρ_N , i.e, the local Ohm's law $E_s^{\text{eff}}(z) = \rho_N j_s(z)$ is valid [75], or

$$j_s(z) = \theta_H j_e(z) - \rho_N^{-1} \frac{d\mu_s}{dz} \quad (3.5)$$

By placing it to the rate equation of the spin current, $\nabla \cdot \mathbf{j}_s = -\mu_s g_e / \tau_{sf}$ where τ_{sf} is the spin-flip time and g_e is the electron density of states, we have,

$$\frac{d^2 \mu_s}{dz^2} - \frac{\mu_s}{\lambda_s^2} = \rho_N \theta_H \frac{dj_e(z)}{dz} \quad (3.6)$$

where λ_s is the diffusion length. Note that the above diffusion equation has a source term at the right side of the equation when the in-plane current density varies spatially. To solve Eqs. (5-6), we use the boundary condition at the outer boundary, $j_s(d_N) = 0$, and at the interface, $j_s(0) = -g_{mix} \mu_s$ where g_{mix} is the mixing conductance. We further use the fact that the source term varies with the mean free path while μ_s with λ_{sd} , and thus we replace $j(z)$ by its average and find

$$j_s(0) = \theta_H \frac{g_{mix} \left(1 - \text{sech} \frac{d_N}{\lambda_s}\right)}{g_N \tanh \frac{d_N}{\lambda_s} + g_{mix}} \frac{1}{d_N} \int_0^{d_N} j_e(z) dz \quad (3.7)$$

where we have introduced $g_N = 1/(\rho_N \lambda_s)$. The STT measures the current induced spin torque which is equivalent to the transverse component of spin current relative to the magnetization direction of the magnetic layer. Clearly, the spin Hall angle measurement based on the STT does not contain the factor $\rho_N \sigma_{||}(z)$. However, we point out, the determination of the current in the heavy metal $\int_0^{d_N} j_e(z) dz$ in Eq. (3.7) could be nontrivial if the interface carries a significant portion of the applied current; we will discuss this case later.

It is interesting to compare Eq. (3.2) and Eq. (3.7) with the giant magnetoresistance (GMR) of magnetic multilayers in the CIP and CPP geometries [1,2]. For CIP, the electric field is independent of position, and thus the spin and electric current densities are given by the two-point conductivity which has a length scale of the mean free path. If two magnetic layers are separated more than the mean free path by the nonmagnetic layer, the resistivity in one magnetic layer would be independent of the other magnetic layers and the magnetoresistance vanishes [76–78]. For the CPP case, the spin current densities are constant within the spin diffusion length, while the total electric field (the applied plus the induced ones) depends on position. If one similarly introduces a two-point resistivity tensor, $\rho_{\perp}(z, z') = [\sigma_{\perp}(z, z')]^{-1}$, one finds a local Ohm's law remains valid, i.e., $E_s^{\text{eff}}(z) = \rho(z) j_s$; this is the model of resistance

in series and the current density will be determined by the resistance in series in all the layers. The CPP magnetoresistance does not decay exponentially with the mean free path, instead, the much longer spin diffusion length is the relevant length scale for the CPP GMR [75, 79]. Equations (3.2) and (3.7) involve essentially the same mathematical features for the CIP and CPP spin transport.

3.2.2 Calculation of Conductivity in Thin Films

We now proceed to evaluate the position-dependence of the current density. For the SP or SS, we need to find $\rho_N \sigma_{||}(z)$, while for STT, we determine the average current density in the non-magnetic layer compared to the total applied current. We summarize our model and calculation below; the detailed derivation are given in the Appendix A. Several different interfaces will be considered. When there is no interface states, the simplest way to calculate $\sigma_{||}(z)$ is by using the semiclassical Boltzmann equation in which the position dependent distribution function is obtained via boundary conditions [80, 81]. Johnson and Camley [82] extended this approach by including the spin-dependent scattering at the interface and in the bulk to model the giant magnetoresistance effect in magnetic multilayers. Since the distribution function varies at the scale of the mean-free path, the interface current density is usually comparable to the bulk. Another approach is to utilize the linear response theory or the Kubo formula to evaluate the two point conductivity, which can be expressed in terms of real space Green's functions [31, 77, 83]. The position-dependent conductivity, with varying impurity distribution, layer thickness and interface roughness, has been calculated across the magnetic multilayers. All of these approaches assume that the role of the interface is to scatter conduction electrons, i.e., the interface is treated as a boundary condition for the distribution function. We should extend the approach of Ref. [31, 77, 83] by explicitly including the cases when the differences in the electronic states for the interface and for the bulk are present.

A simple model Hamiltonian of the bilayer is chosen,

$$H = H_0 + H' \quad (3.8)$$

where $H_0 = H_L + H_R + H_{int}$ is the sum of the Hamiltonians for the left layer, the right layer, and the interface monolayer, H' describes the coupling between the interfacial monolayer and the left/right layers. More explicitly,

$$H_L = -t \sum_{\langle i,j \rangle \in L, \mathbf{k}_{||}} \left(c_{i\mathbf{k}_{||}}^+ c_{j\mathbf{k}_{||}} + h.c. \right) + \sum_{i \in L} c_{i\mathbf{k}_{||}}^+ \varepsilon_{\mathbf{k}_{||}}^L c_{i\mathbf{k}_{||}} \quad (3.9)$$

for the left layer and similarly for the right layer (replacing L by R in the above equation), where t is the hopping strength between the two nearest neighbors, $c_{i\mathbf{k}_\parallel}^+ = (c_{i\mathbf{k}_\parallel\uparrow}^+, c_{i\mathbf{k}_\parallel\downarrow}^+)$ is conduction electron creation operator at site i , expressed in the spinor form. Note that we have written the Hamiltonian in the mixed space-momentum representation: the translation invariance in the plane of the layer allows us to use the in-plane momentum \mathbf{k}_\parallel as a quantum number while we retain the layered index i to represent the growth direction.

The Hamiltonian of the interface is

$$H_{int} = \sum_{\mathbf{k}_\parallel} c_{0\mathbf{k}_\parallel}^+ \varepsilon_{0\mathbf{k}_\parallel} c_{0\mathbf{k}_\parallel} \quad (3.10)$$

where the sub-index “0” indicates the interface layer, and $\varepsilon_{0\mathbf{k}_\parallel}$ is the interface energy dispersion which could be spin-dependent.

The interaction between the interface and left/right layers is modeled by

$$H' = -t_L \sum_{\mathbf{k}_\parallel} c_{0\mathbf{k}_\parallel}^+ c_{-1\mathbf{k}_\parallel} - t_R \sum_{\mathbf{k}_\parallel} c_{0\mathbf{k}_\parallel}^+ c_{1\mathbf{k}_\parallel} + h.c. \quad (3.11)$$

where $t_{L/R}$ is the hopping parameter between the interface and the left/right layer. Note that the left (right) layer is indexed with a negative (positive) integer i representing the atomic position at $z = ia$; thus $i = -1$ and $i = 1$ are two atomic layers in contact with the interface layer $i = 0$.

The two-point conductivity for the layered structure can be obtained by the Kubo formula [31, 77]

$$\sigma_{\parallel}(i, j) = \frac{\hbar e^2}{\pi a^3} \sum_{\mathbf{k}_\parallel} v_{\mathbf{k}_\parallel}(i) A(i, j; E_F, \mathbf{k}_\parallel) v_{\mathbf{k}_\parallel}(j) A(j, i; E_F, \mathbf{k}_\parallel) \quad (3.12)$$

where $A(i, j; E_F, \mathbf{k}_\parallel) = \frac{i}{2} [G_a(i, j; E_F, \mathbf{k}_\parallel) - G_r(i, j; E_F, \mathbf{k}_\parallel)]$ is the spectral density function, $G_{a/r}$ is the advanced/retarded Green's function, $v_{\mathbf{k}_\parallel} = \partial\varepsilon_{\mathbf{k}_\parallel}/\hbar\partial\mathbf{k}_\parallel$ is the velocity operator of the local bands for left, interface or right layers. Note that Green's function and the velocity are spinors if the Hamiltonian is spin-dependent.

3.2.3 Controversy between differently measured spin Hall angle

We now apply the above two-point conductivity to a particular bilayer consisting of NiFe and Pt layers. We first assume there is no interface state and define a specular reflection parameter p ($p = 0$ for completely rough interface and $p = 1$ is completely

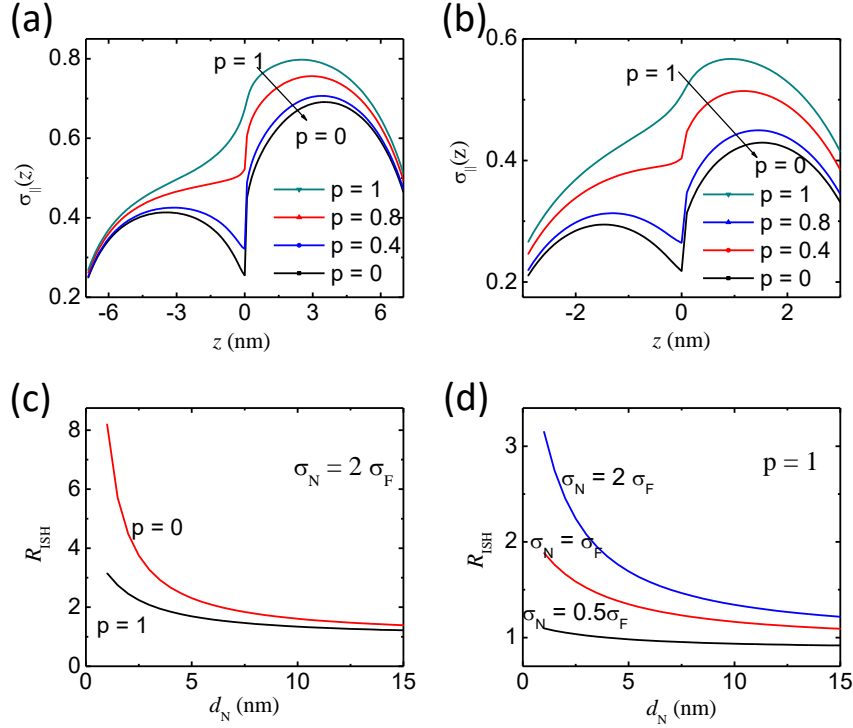


FIGURE 3.2. (a) and (b): Spatial dependence of the electric conductivity across a FM ($z < 0$)/NM ($z > 0$) bilayer for different film thickness. The magnitude of the conductivity is normalized by the bulk value of the NM layer. (c): The correction factor R as a function of NM layer thickness. In above calculation, we have taken the density of states and for the FM and NM to be the same so that the conductivity conductivity ratio is identical to the ratio of electron mean free path. In In Fig. 2(a-c) we take the mean free path as $\lambda_N = 10$ nm and $\lambda_F = 5$ nm and the spin diffusion length as $\lambda_s = 10$ nm. In Fig 2(d), three different $\lambda_F = 20, 10, 5$ nm are shown.

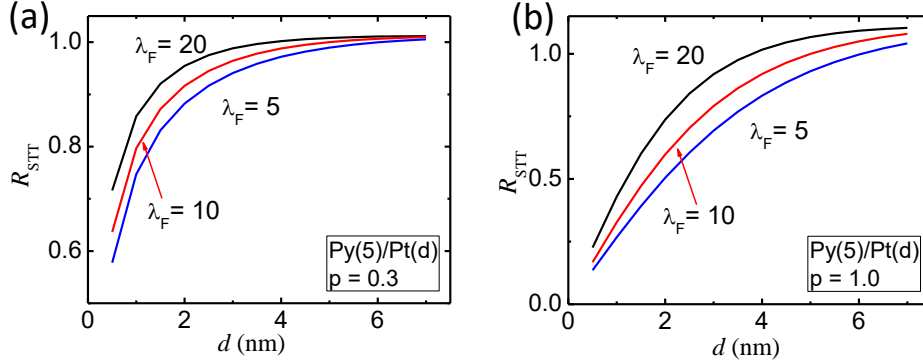


FIGURE 3.3. The conductivity of a thin film with and without surface states as a function of layer thickness, λ is the electron mean free path in the bulk. When there is no surface states, the semiclassical continuous model (black square line) and our tight-binding approach (red circle line) are approximately same. In the presence of the surface state (c), the conductivity increases at the small thickness. The details of the parameters used are given in the Appendix A.

smooth interface, and we takes $p = 0$ at the outer boundaries), as introduced by Fuchs [80]. We treat both NiFe and Pt as free electron gases with typical room-temperature resistivity values $\rho_{\text{NiFe}} = 40 \mu\Omega\text{cm}$, and $\rho_{\text{Pt}} = 25 \mu\Omega\text{cm}$ [42]. In Fig. 2 (a) and (b), we show the position-dependence of the reduced conductivity $\sigma_r \equiv \rho_N \sigma_{\parallel}(z)$ for two different thickness and interface specular parameters. The σ_r is always smaller than 1 in the non-magnetic layer due to additional scattering from the interface. The reduction of σ_r is more profound for smaller thickness: it is averaged as 0.5 for $d_N = 7$ nm, and $0.3 \sim 0.4$ for $d_N = 3$ nm; this is consistent with the enhancement contribution of the resistivity from the surface/interface scattering. Using these numerical values, we can readily show the correction of the spin Hall angle to the previous measured θ_H , as plotted in Fig. 2(c). The enhancement of the spin Hall angle is approximately given by the average over the inverse over σ_r . For example, for $d_N = 7$ nm and a rough interface $p = 0$, we find $R = 2$. The ferromagnetic conductivity can affect the enhancement factor as well. In Fig. 2(d), we show R as a function of NM layer thickness for three different FM conductivity without interface roughness ($p = 1$). Clearly, the influence of the ferromagnetic layer is diminished when the interface is rough ($p = 0$).

Recently, there is growing evidence that the spin-charge conversion also takes place at the interface [49, 65, 84–90]. In the presence of large spin-orbit coupling known as

the Rashba interaction, a spin helix state exists at the transition metal interface, but not in the bulk. In this case, the current density distribution at the interface could significantly differ from the bulk. In the extreme case of doped magnetic/non-magnetic topological insulator bilayer, the interface conduction is much higher than in the bulk, and thus the proper determination of the spin and charge currents in the layer and at the surface becomes a challenging issue. As an example, if we model the interface dispersion by,

$$\varepsilon_{0\mathbf{k}} = \varepsilon_0 + \hbar v_F (\mathbf{k} \times \boldsymbol{\sigma}) \cdot \hat{z}, \quad (3.13)$$

several additional physics enter: the interface carries a significant in-plane current, contributes spin Hall signal, and absorbs the spin current. In the SP, the interface leads to the spin memory loss [21, 50, 91], in the meanwhile, it creates an interface inverse Edelstein effect [14]. For the STT, there are complications on the relative contributions of the spin torque from the interface and bulk. We show in Fig. 3, that in the present of the above interface states, the current has a higher density than that in the bulk. In general, the quantitative determination of the interface versus bulk from the present experiments of SP and STT is difficult, we nevertheless propose that if the spin Hall and inverse spin Hall effects have independent contribution from the interface and from the bulk, a simple additive formula for the measured electric field by the spin pumping or spin Seebeck is,

$$E_m = G_t^{-1} j_s(0) \left[\rho_N \theta_H \int_0^{d_N} dz \sigma_{||}(z) \sinh \frac{d_N - z}{\lambda_s} + (1 - \delta)^{-1} \theta_i d_i \right] \quad (3.14)$$

where θ_i is the spin Hall angle of the interface, d_i the effective thickness of the interface, δ is the spin memory loss factor that characterizes the reduction of the spin current by the interface spin-flip process [21]. Similarly, for the STT experiment, one includes the interface contribution,

$$j_s(0) = \theta_H \frac{g_{mix} \left(1 - \operatorname{sech} \frac{d_N}{\lambda_s} \right)}{g_N \tanh \frac{d_N}{\lambda_s} + g_{mix}} \frac{1 - \delta}{d_N} \int_0^{d_N} j_e(z) dz + \theta_i j_e^i \quad (3.15)$$

where j_e^i is the electrical current at the interface. Through a detailed thickness-dependent measurement, it is possible to extract the spin Hall angle parameters of the interface and bulk with a reasonably acceptable accuracy.

CHAPTER 4

SPIN CONDUCTANCE AT MAGNETIC INTERFACES

Angular momentum transport in magnetic multilayered structures plays a central role in spintronic physics and devices. The angular momentum currents or spin currents are carried by either quasi-particles such as electrons and magnons, or by macroscopic order parameters such as local magnetization of ferromagnets. Based on the generic interface exchange interaction, we develop a microscopic theory that describes interfacial spin conductance for various interfaces among non-magnetic metals, ferromagnetic and antiferromagnetic insulators. Spin conductance and its temperature dependence are obtained for different spin batteries including spin pumping, temperature gradient and spin Hall effect. As an application of our theory, we calculate the spin current in a trilayer made of a ferromagnetic insulator, an antiferromagnetic insulator and a non-magnetic heavy metal. The calculated results on the temperature dependence of spin conductance quantitatively agree with the existing experiments.

4.1 Motivation

In spintronics, one of the most important variables is spin current which describes the propagation of angular momentum information through magnetic and non-magnetic media [92]. There are a number of different carriers that contribute to spin current. In non-magnetic metals, the carriers are conduction electrons while for magnetic insulators, the angular momentum carriers are magnons or spin waves. When these different carriers meet at interfaces, they transfer the angular momentum via interfacial exchange interaction. For example, the spin pumping describes a precessing ferromagnet transferring its long wavelength magnon current to an electron spin current in the adjacent metallic layer [25, 93], and the spin Seebeck effect addresses the spatially non-uniform thermal magnon diffusion [94–97].

Recent experiments have shown that angular momentum current transfer at interfaces is a general phenomenon for many combinations of materials as long as the low-energy carriers (quasi-particles or order parameters) of the materials have nonzero angular momentum [20, 98–106]. In a trilayer made of a ferromagnetic insulator (FI) layer (YIG) sandwiched between two non-magnetic metallic layers (Pt), it has been

observed that a charge current applied in one of the metal layers can result in a charge current in the other layer via magnon-mediated spin current propagation [98–102]. The observed signal is much more profound at high temperature, indicating that a simple model based on a temperature independent interfacial mixing conductance would fail to describe the experimental findings [100, 102]. Other recent experiments demonstrated that the spin current can flow from a ferromagnetic insulator to a non-magnetic metallic (NM) layer with a thin antiferromagnetic insulator (AFI) in between [20, 103–105]. Furthermore, the spin propagation efficiency is much enhanced at high temperature when compared with the device without the AFI layer [20, 104]. These findings call for a more comprehensive theoretical model which is capable of addressing the angular momentum current across interfaces between different materials at finite temperature.

There are a number of existing theoretical models for the spin conductance (SC) near interfaces. In spin pumping, the SC or mixing conductance between a ferromagnetic layer and non-magnetic metallic layer has been calculated at zero temperature using first principle methods [107]. In spin Seebeck effect, the SC between the FI and NM layers has been studied by model Hamiltonians and the resulting SC is highly temperature dependent [16]. Thus, the spin conductances for the thermally driven spin Seebeck effect and for the spin pumping are quite different even though the interface is identically same. There are also theoretical studies involving AFI layer. Ohnuma *et al.* calculated the spin current due to a temperature difference across the AFI and NM interface [108]. Cheng *et al.* studied spin pumping from an AFI layer to a NM layer [109]. Recently, Rezende *et al.* introduced a mixing conductance for the interfaces between FI and AFI layers phenomenologically without calculating its temperature or material dependence [110].

In this chapter, we develop a theory to formulate the SC for interfaces with different material combinations by using a generic interface exchange Hamiltonian, with an emphasis on the temperature dependence of the SC.

4.2 Magnons and Spin batteries

4.2.1 Three spin Batteries

The interface SC is defined as the ratio of the spin or angular momentum current across the interface to the spin voltage drop at the two sides of the interface. The spin voltage is provided by a spin battery. Followed the three spin current generators introduced in Ref. [111], we define the spin battery voltage in each case before

calculating the SC.

First, the spin voltage of the “spin pumping battery” [112], which is generated by an external microwave source such that the magnetization of ferromagnetic layer undergoes precession motion in the ferromagnetic resonance (FMR) condition, can be defined as

$$\mathbf{V}_{\text{sp}} = \frac{\hbar}{4\pi} \mathbf{m} \times \frac{d\mathbf{m}}{dt}, \quad (4.1)$$

where \mathbf{m} is the dimensionless unit vector representing the direction of the magnetization of the layer. It is understood that the spin pumping battery provides non-equilibrium magnons with zero wave number ($k = 0$).

The second spin battery is created by a temperature gradient across a FI layer [16, 116]. The presence of the position-dependent temperature $T = T(x)$ in the FI layer ($x < 0$) leads to a non-uniform local magnon density

$$n(x) = \int d\varepsilon_{\mathbf{q}} g_m^{\text{F}}(\varepsilon_{\mathbf{q}}) N_0(\varepsilon_{\mathbf{q}}, T)$$

where $N_0(\varepsilon_{\mathbf{q}}, T) = [e^{\varepsilon_{\mathbf{q}}/k_B T} - 1]^{-1}$ is the Bose-Einstein distribution function and $g_m^{\text{F}}(\varepsilon_{\mathbf{q}})$ is the FI magnon density of states. The magnon diffusion generates a magnon current in the FI layer. When the magnon current flows to the interface, a non-equilibrium magnon density is accumulated near the interface. These non-equilibrium magnon accumulation becomes a spin voltage that can excite spin degree of freedom at the other side of the interface. In the open circuit condition (i.e., an isolated FI layer without a contacting layer), the magnon accumulation is proportional to the magnon diffusion length. Thus, we define the thermally driven spin battery voltage as

$$\mathbf{V}_{\text{th}} = \lambda_{\text{F}} \frac{d(k_B T)}{dx} \mathbf{m} \quad (4.2)$$

where k_B is the Boltzmann constant and λ_{F} is the magnon diffusion length within the FI layer.

The third battery is built up in a non-magnetic layer such as Pt with a large spin Hall angle. When an in-plane current is applied to the NM layer, a spin Hall current flowing perpendicular to the charge current is generated. Similar to the magnon accumulation for magnetic materials, electron spin accumulation is built near the interface and scales with the spin diffusion length in the open circuit condition [12]. The spin Hall battery voltage in this case is

$$\mathbf{V}_{\text{sh}} = e\theta_{\text{sh}}\rho\lambda_{\text{N}}\hat{\mathbf{z}} \times \mathbf{j}_e \quad (4.3)$$

where e is the electron charge, θ_{sh} is the spin Hall angle, λ_{N} is the spin diffusion length within the NM material, ρ is the resistivity, $\hat{\mathbf{z}}$ is the unit vector normal to the interface, and \mathbf{j}_e is the electron current density.

We emphasize a few points on the above definitions: 1) we have chosen the unit of the spin battery to be that of energy, 2) the spin battery is a vector which characterizes the direction of the angular momentum (note that the spin pumping battery is transverse to \mathbf{m} and the temperature gradient battery is parallel to \mathbf{m}), 3) the battery “stores” different forms of spin angular momenta: zero-wave number magnons for spin pumping battery, magnon accumulation with a broad distribution of wave numbers for the thermal battery, and electron spin accumulation for the spin Hall battery.

These spin batteries, in Eqs. (4.1), (4.2), and (4.3), are defined for an isolated layer, i.e, in the absence of spin current. When the battery is connected to a layer which is capable of carrying spin momenta, a spin current flows in the neighboring layer as well as in the battery layer. Thus, both internal spin current (within the battery layer) and external spin current will “consume” spin angular momentum. However, the comparison between charge and spin batteries on the internal and external resistance or conductance shows one fundamental difference: the electric current is conserved but the spin current is not, thus the addition of the resistance in series is no longer valid for the spin resistance [125]; we shall illustrate in later sections on how to calculate the spin current with many layers or many spin conductors in series. The main goal of the present paper is to calculate the SC at finite temperatures, for interfaces between different materials and for three different batteries. We shall first tabulate our calculated results in Table I. The explanation of the Table I is given below and the detailed derivation of these results will be given in the next Section.

Table I shows the spin conductance for three spin batteries. In the first two cases in which the battery layer is a FI, we consider two bilayers, FI/NM and FI/AFI. In the third case, the battery is the NM layer and we consider NM/FI and NM/AFI interfaces. In all bilayers, the total spin current also depends on the backflow [54]: when the battery generates a spin current in the neighboring layer, a spin or magnon accumulation will be established in the layer, which in turn, flows a portion of the spin current back to the battery, resulting a smaller interface spin current. The backflow parameter, ϵ , is determined by the ratio of the spin conductance at the interface to that in the layers. In a bilayer structure, the backflow parameter for three batteries has the same form, $\epsilon = G_{\text{int}}/G_{\text{L}} + G_{\text{int}}/G_{\text{R}}$ where $G_{\text{L/R}}$ is the spin conductance of the left/right layer, see next section for details.

TABLE 4.1. List of spin conductance $G_{\text{int}}a^2$ (a is the lattice constant) of several magnetic interfaces driven by different batteries. In these bilayer structures, the spin current across the interface is $\mathbf{j}_s = G_{\text{int}}\mathbf{V}/(1+\epsilon)$ where ϵ characterizes a backflow spin current and will be calculated in late sections. The Table gives the dependence of the SC on temperature T , interface coupling strength J_{int} , electron density of states at Fermi level $g_e(E_F)$, Curie temperature T_C , and Néel temperature T_N .

Batteries	Interface	H_{int}	$G_{\text{int}}a^2$
Spin pumping	FI/NM	$J_{\text{int}}a_0^+c_{\mathbf{k}\uparrow}^+c_{\mathbf{k}\downarrow}$	$\left(J_{\text{int}}g_e(E_F)\right)^2$
	FI/AFI	$J_{\text{int}}a_{\mathbf{q}1}^+a_{\mathbf{q}2}a_0\beta_{\mathbf{q}3}$	$\frac{J_{\text{int}}^2}{(k_B T_C)(k_B T_N)}\left(\frac{T}{T_C}\right)^2\left(\frac{T}{T_N}\right)^3$
Temperature gradient	FI/NM	$J_{\text{int}}a_{\mathbf{q}}^+c_{\mathbf{k}\uparrow}^+c_{\mathbf{k}\downarrow}$	$\left(J_{\text{int}}g_e(E_F)\right)^2\left(\frac{T}{T_C}\right)^{3/2}$
	FI/AFI	$J_{\text{int}}a_{\mathbf{q}}^+\alpha_{\mathbf{q}}$	$\frac{J_{\text{int}}^2}{(k_B T_C)(k_B T_N)}\left(\frac{T}{T_C}\right)^{1/2}\left(\frac{T}{T_N}\right)^3$
Spin Hall	NM/FI ($\boldsymbol{\mu}_s \perp \mathbf{m}$)	$J_{\text{int}}a_0^+c_{\mathbf{k}\uparrow}^+c_{\mathbf{k}\downarrow}$	$\left(J_{\text{int}}g_e(E_F)\right)^2$
	NM/FI ($\boldsymbol{\mu}_s \parallel \mathbf{m}$)	$J_{\text{int}}a_{\mathbf{q}}^+c_{\mathbf{k}\uparrow}^+c_{\mathbf{k}\downarrow}$	$\left(J_{\text{int}}g_e(E_F)\right)^2\left(\frac{T}{T_C}\right)^{3/2}$
	NM/AFI ($\boldsymbol{\mu}_s \parallel \mathbf{n}$)	$J_{\text{int}}(\alpha_{\mathbf{q}}^+ + \beta_{\mathbf{q}})c_{\mathbf{k}\uparrow}^+c_{\mathbf{k}\downarrow}$	$\left(J_{\text{int}}g_e(E_F)\right)^2\left(\frac{T}{T_N}\right)^4$

For spin pumping at FI/NM interfaces, the angular momentum current conversion occurs between the zero wave number magnons in the FI layer and the conduction electron spins in the NM layer [93]. The spin conductance in this case has been identified as the mixing conductance. The temperature dependence is unimportant since the conduction electron distribution is weakly dependent on temperature. For other interfaces, i.e., FI/AFI, the spin conductance involves conversion from FI magnons to AFI magnons with broadly distributed wave numbers. Since the density of the magnons is highly temperature dependent, one expects a similar dependence for the SC. The SC in Table I is for low temperatures (lower than Néel or Curie temperatures) where the temperature dependence can be analytically derived. For higher temperatures, analytical expressions are unavailable; we will present the numerical results in later Sections. The spin conductances for the temperature gradient battery are shown with the same two interfaces, FI/NM and FI/AFI. In both cases, there are strong temperature dependence.

Spin conductance for the spin Hall battery is also summarized. It is interesting to note that the electron spin current from the spin Hall battery can excite two types of magnons: coherent zero wave number magnons which represent the uniform

magnetization precession or spin transfer torque ($\boldsymbol{\mu}_s \perp \mathbf{m}$), and incoherent magnons that produce a dc magnon current ($\boldsymbol{\mu}_s \parallel \mathbf{m}$ or $\boldsymbol{\mu}_s \parallel \mathbf{n}$). When driven by the spin Hall effect, the interface spin conductance is either same as the spin pumping conductance or the thermal conductance depending on the relative direction between the electron spin accumulation and the magnetization. We will further discuss these in next section. It is noted that the magnetic metal is not included in this paper because of an additional complication: a magnetic metal has both magnons and conduction electron spins, and thus spin current in different layers will involve much more channels; we will leave such complication for further studies.

4.2.2 Magnons in Ferromagnets and Anti-ferromagnets

For nonmagnetic metals, the spin current carriers are conduction electrons whose dispersion relations are described by free electron model, i.e., $\varepsilon_k = (\hbar k)^2/2m_e$. For FI or AFI, we model the spin Hamiltonian below,

$$H = \pm J_{ex} \sum_{\langle i,j \rangle} \mathbf{S}_i \cdot \mathbf{S}_j - H_{\text{ext}} \sum_i S_i^z - K \sum_i (S_i^z)^2 \quad (4.4)$$

where J_{ex} is the exchange constant between nearest neighbors, H_{ext} is the external magnetic field applied in the z direction and K is the easy axis anisotropy constant.

When choosing the minus sign in the above Hamiltonian, the spin lattice has a ferromagnetic ground state. Within the spin wave approximation, one can readily obtain the low-energy quasiparticle spectrum as

$$H_{\text{F}} = \sum_{\mathbf{q}} \varepsilon_{\mathbf{q}}^{\text{F}} a_{\mathbf{q}}^+ a_{\mathbf{q}} \quad (4.5)$$

where $\varepsilon_{\mathbf{q}}^{\text{F}} = 2J_{ex}SZ(1 - \gamma_{\mathbf{q}}) + 2KS + \gamma_0 H_{\text{ext}}$ is the magnon dispersion, Z is the number of nearest neighbors, S the magnitude of each atomic spin and $\gamma_{\mathbf{q}} = 1/Z \sum_{\boldsymbol{\delta}} e^{i\mathbf{q} \cdot \boldsymbol{\delta}}$ where $\boldsymbol{\delta}$ runs over all nearest neighbor positions. $\Delta_{\text{F}} = 2KS$ is the FI magnon gap.

With the positive sign, the Hamiltonian describes an antiferromagnetic lattice. Within the spin wave approximation, the magnon spectra are

$$H_{\text{A}} = \sum_{\mathbf{q}} (\varepsilon_{\mathbf{q}}^{\alpha} \alpha_{\mathbf{q}}^+ \alpha_{\mathbf{q}} + \varepsilon_{\mathbf{q}}^{\beta} \beta_{\mathbf{q}}^+ \beta_{\mathbf{q}}) \quad (4.6)$$

where $\alpha_{\mathbf{q}}$ and $\beta_{\mathbf{q}}$ represent two branches of magnon and

$$\varepsilon_{\mathbf{q}}^{\alpha, \beta} = J_{ex}SZ \sqrt{(1 + 2K/JZ)^2 - \gamma_{\mathbf{q}}} \pm \gamma_0 H_{\text{ext}}.$$

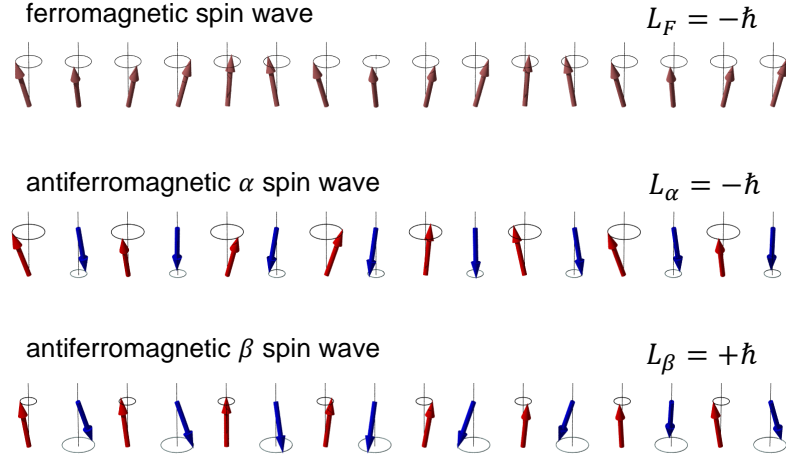


FIGURE 4.1. Spin waves in ferromagnets and antiferromagnets. The brown, red and blue arrows are the spins on the FI lattice, AFI sublattice A and AFI sublattice B , respectively.

$\Delta_A = \sqrt{2KS \times J_{ex}SZ}$ is the AFI magnon gap .

There are four important distinctions between the FI and AFI magnons which distinguishes the spin convertance at AFI interface from that at FI interface. First, the FI magnon has a small energy gap determined by the anisotropy while the AFI magnon has a much larger gap because it scales with the geometrical average of the exchange constant and the anisotropy. Another distinction is that each F magnon carries an angular momentum $-\hbar$ with respect to the magnetization direction while in the AF lattice, a magnon in one branch ($\alpha_{\mathbf{q}}$) carries $-\hbar$ and the other ($\beta_{\mathbf{q}}$) carries \hbar . In Fig. 4.1, we depict spin configuration of a FI magnon and a AFI magnon in each of the two branches. A $\alpha_{\mathbf{q}}$ magnon represents the mode with a larger precession angle for sublattice A (Red) than B (Blue), i.e., $\theta_A > \theta_B$. While both θ_A and θ_B depend on \mathbf{q} , the angular momentum is $L_\alpha = -N_A S \hbar [(\theta_A^A)^2 - (\theta_B^B)^2] \equiv -\hbar$ for a α magnon and $L_\beta = \hbar$ for a β magnon, where N_A is the number of spins in the AFI lattice. In the absence of the external magnetic field, $\alpha_{\mathbf{q}}$ and $\beta_{\mathbf{q}}$ magnons have exactly same energy, indicating that these two degenerate magnon branches are equally populated at any temperature, and thus there is no net magnetization or spin current at equilibrium. Third, the ferromagnetic magnon has identical precession angle which is independent of magnon wave vector or energy. While the AF magnons have different precession angles which has on influence on temperature dependence of the spin convertance.

Last, the ferromagnetic magnon wave vector takes up to the whole Brillouin zone while the AF magnon wave vectors only occupy half of that. Such difference leads to Umklapp scattering at the interface of anti-ferromagnets.

Having specified the angular momentum carriers in each layer, we now introduce the spin interaction between two materials in contact. A generic exchange interaction at the interface between two spins would be simplest and universal,

$$H_{\text{int}} = -J_{\text{int}} \sum_i \mathbf{S}_i^{(L)} \cdot \mathbf{S}_i^{(R)} \quad (4.7)$$

where $\mathbf{S}_i^{(L)}$ ($\mathbf{S}_i^{(R)}$) represents the spin at the interface of the left (right) layer. For the FI or AFI layers, S_i refers to the spin at the local site, while for the NM, S_i denotes the spin of conduction electrons at the interface.

4.3 Spin convertace dirven by Various Batteries

4.3.1 Spin conductance of a spin pumping battery

The spin pumping battery has widely been used for the generation of the spin current in NM layers. The SC has first been formulated via interfacial reflection and transmission coefficients in the scattering approach [54]. Other models [93], including a simple linear response theory [21], yield essentially same result. Here we briefly re-derive it with Eq. (4.7) for the FI/NM interface and then continue with the derivation for the FI/AFI interface.

The second quantization of Eq. (4.7) at the FI/NM interface is

$$H_{\text{int}} = -J_{\text{int}} \sqrt{2S_{\text{F}}} \sum_{\mathbf{k}\mathbf{k}'\mathbf{q}} (a_{\mathbf{q}}^+ c_{\mathbf{k}'\uparrow}^+ c_{\mathbf{k}\downarrow} + H.c.) \delta_{\mathbf{k}',\mathbf{k}+\mathbf{q}} \quad (4.8)$$

where $c_{\mathbf{k}\sigma}^+$ ($c_{\mathbf{k}\sigma}$) is the conduction electron creation (annihilation) operator, N_{F} (N_{N}) is number of lattice sites of FI (NM) at the interface and S_{F} is the magnitude of each FI spin. The spin current across the interface is,

$$j_s = \left\langle \frac{1}{iA_I} \left[\sum_{\mathbf{q}} a_{\mathbf{q}}^+ a_{\mathbf{q}}, H_{\text{int}} \right] \right\rangle \quad (4.9)$$

where $[,]$ is the quantum commutator, $\langle \rangle$ refers to the average over all states and A_I is the interface cross area. Use the rough interface approximation, we don't impose

the momentum conservation in Eq. (4.8). By placing Eq. (4.8) into Eq. (4.9) and by utilizing the random phase approximation, we find

$$j_s = \frac{2\pi J_{\text{int}}^2 S_{\text{F}}}{N_{\text{F}} N_{\text{N}} A_{\text{I}}} \sum_{\mathbf{k}\mathbf{k}'\mathbf{q}} [(N_{\mathbf{q}}^{\text{F}} + 1)(1 - f_{\mathbf{k}\uparrow})f_{\mathbf{k}'\downarrow} - N_{\mathbf{q}}^{\text{F}} f_{\mathbf{k}\uparrow}(1 - f_{\mathbf{k}'\downarrow})] \delta(\varepsilon_{\mathbf{q}}^{\text{F}} + \varepsilon_{\mathbf{k}} - \varepsilon_{\mathbf{k}'}) \quad (4.10)$$

where $N_{\mathbf{q}}^{\text{F}}$ and $f_{\mathbf{k}'s}$ are the magnon and electron distribution functions. In thermal equilibrium, the magnons and electrons can be described by the Boson and Fermion statistics.

For the spin pumping voltage, the magnon distribution is the sum of the thermal magnon $N_0(\varepsilon_{\mathbf{q}}, T)$ and coherent $q = 0$ magnons $\delta_{\mathbf{q}0} N_{\text{F}} S_{\text{F}} \sin^2 \theta$ representing the uniform precession driven by microwave magnetic field, where θ is the magnetization precession angle. The energy of a $q = 0$ magnon is given by the FMR frequency ω , i.e., $\varepsilon_{q=0}^{\text{F}} = \hbar\omega$. Inserting the distribution function into Eq. (4.10), we find

$$j_s^{\text{sp,NM}} = 2\pi\hbar J_{\text{int}}^2 S_{\text{F}}^2 a_{\text{N}}^4 g_e^2(E_{\text{F}}) \omega \sin^2 \theta \quad (4.11)$$

where a_{N} is the lattice constant of the NM material and $g_e(E_{\text{F}})$ the electron density of states near Fermi energy. Under the FMR condition, we identify $\omega \sin^2 \theta$ as the dc component of $\mathbf{m} \times \frac{d\mathbf{m}}{dt}$. Compare with the definition of the spin conductance $\mathbf{j}_s = G_{\text{F/N}}^{\text{sp}} \mathbf{V}_{\text{sp}}/2\pi$, we find,

$$G_{\text{F/N}}^{\text{sp}} = 8\pi^2 J_{\text{int}}^2 S_{\text{F}}^2 a_{\text{N}}^4 g_e^2(E_{\text{F}}). \quad (4.12)$$

The above SC is also known as the mixing conductance [54]. After discarding the unimportant constants, Eq. (4.12) is listed in the first row of Table 4.1. We note that Ohnuma *et al.* have already derived the SC using similar method, but expressed the result in terms of ferromagnetic susceptibility [93]. By replacing the susceptibility with the Lindhard susceptibility of a non-magnetic metal, one will directly get the mixing conductance derived here.

Next, we calculate the spin pumping conductance for a FI/AFI interface. The second quantization of H_{int} in Eq. (4.7) gives the coupling between FI and AFI magnons. The lowest order terms refer to two magnon interactions. The angular momentum conservation limits the possible two-magnons processes to $a_0(\alpha_{\mathbf{q}'}^+ + \beta_{\mathbf{q}'})$ and its complex conjugate. However, such process is prohibited by the energy conservation: the energy of the FMR frequency or $q = 0$ magnon is too small to excite any magnon in the AFI. Thus, the angular momentum current across the interface must go through at least four magnon processes. By expanding Eq. (4.7) to four magnon operators, we obtain a number of terms which satisfy both energy and angular momentum

conservation. For example, the term $a_{\mathbf{q}_1}^+ a_0 a_{\mathbf{q}_2} \beta_{\mathbf{q}_3}$ represents the transfer of the angular momentum in the FI by annihilating a $q = 0$ and two thermal magnon of the FI layer, and simultaneously annihilating a β magnon in the AFI layer, as long as $\varepsilon_{\mathbf{q}_1}^F = \varepsilon_0^F + \varepsilon_{\mathbf{q}_2}^F + \varepsilon_{\mathbf{q}_3}^\alpha$. After tedious but straightforward calculations, we find the spin current across the interface via such four magnon processes can be written as

$$j_s^{\text{sp,AFI}} = \frac{\pi J_{\text{int}}^2 S_A}{8 N_F N_A} \sum_{\mathbf{q}_1 \mathbf{q}_2 \mathbf{q}_3} (\zeta_{\mathbf{q}_3}^2 + \zeta_{\mathbf{q}_3}^{-2}) \delta(\varepsilon_{\mathbf{q}_1}^F - \varepsilon_{\mathbf{q}_2}^F - \varepsilon_{\mathbf{q}_3}^\alpha - \varepsilon_0^F) \quad (4.13)$$

$$[(N_{\mathbf{q}_1}^F + 1) N_{\mathbf{q}_2}^F N_{\mathbf{q}_3}^\alpha N_{q=0}^F - N_{\mathbf{q}_1}^F (N_{\mathbf{q}_2}^F + 1) (N_{\mathbf{q}_3}^\alpha + 1) (N_{q=0}^F + 1)]$$

where $\zeta_{\mathbf{q}}^2 = |(\theta_A - \theta_B)/(\theta_A + \theta_B)|$ [118] and θ_A (θ_B) is the precession angle for a given spin wave mode, $N_{\mathbf{q}_{1/2}}^F$ and $N_{q=0}^F$ are the FI magnon distribution functions, and $N_{\mathbf{q}_3}^\alpha$ are the distribution functions of AFI α magnons; in the long wavelength limit, $\zeta_{\mathbf{q}}^2 \simeq \varepsilon_{\mathbf{q}}/J_{ex} S_A Z$. By inserting the ferromagnetic resonance driven magnon distribution function, $N_{\mathbf{q}} = N_0(\varepsilon_{\mathbf{q}}, T) + \delta_{\mathbf{q}0} N_F S_F \sin^2 \theta$, we find the SC at FI/AFI interface due to the $a_{\mathbf{q}_1}^+ a_0 a_{\mathbf{q}_2} \beta_{\mathbf{q}_3}$ process, $G_{\text{A/F}}^{\text{sp}} = 2\pi \mathbf{j}_s^{\text{sp,AFI}}/\mathbf{V}_{\text{sp}}$, is

$$G_{\text{A/F}}^{\text{sp}} = a_F^5 a_A^2 \frac{J_{\text{int}}^2 S_A}{32 k_B T} \int d\varepsilon_{\mathbf{q}} \int d\varepsilon_{\mathbf{q}'} \left(\zeta_{\mathbf{q}'}^2 + \zeta_{\mathbf{q}'}^{-2} \right) g_m^F(\varepsilon_{\mathbf{q}}) g_m^A(\varepsilon_{\mathbf{q}'}) g_m^F(\varepsilon_{\mathbf{q}} + \varepsilon_{\mathbf{q}'}) \quad (4.14)$$

$$\text{csch}^2 \frac{\varepsilon_{\mathbf{q}}}{2k_B T} \text{csch}^2 \frac{\varepsilon_{\mathbf{q}'}}{2k_B T} \text{csch}^2 \frac{\varepsilon_{\mathbf{q}} + \varepsilon_{\mathbf{q}'}}{2k_B T}$$

where a_F (a_A) is the FI (AFI) lattice constant and $g_m^{\text{A/F}}(\varepsilon)$ is the AFI/FI magnon density of states. For temperatures much lower than the Curie and Néel temperatures, Eq. (4.14) reduces to the value listed in the second row of Table 4.1 where the unimportant numerical factors are discarded. The term $a_{\mathbf{q}_1}^+ a_0 a_{\mathbf{q}_2} \alpha_{\mathbf{q}_3}^+$ makes identical contribution to the spin conductance that shown in Eq. (4.14). Notice that the interaction in Eq. (4.7) also contains other four magnon terms involving three AFI magnons and one $q = 0$ FI magnon like $a_0 \alpha_{\mathbf{q}_1}^+ \alpha_{\mathbf{q}_2}^+ \alpha_{\mathbf{q}_3}$ and so on. Below the Néel temperature, the spin pumping conductance from those terms can be estimated as $a_F^{-1} a_A^{-1} \frac{J_{\text{int}}^2}{k_B^2 T_C T_N} \left(\frac{T}{T_N} \right)^5$. The total spin pumping conductance is the sum of all these contributions.

As we have discussed earlier, the total spin current depends on the backflow. The backflow can be easily included if the layer thickness is much larger than the relevant length scales such as the spin or magnon diffusion lengths. The spin current provided by the spin battery decays in the layer; this creates a spin accumulation or magnon accumulation that drive a backflow spin current. One may introduce a spin conductance $G_N = (h/2e^2)(1/\rho\lambda_N)$ as the spin conductance for the NM layer and similarly, G_F and G_A for the FI and AFI layers. The Onsager reciprocal relation can

be used to determine the backflow current [26] such that the total spin current across the interface is reduced by $(1 + \epsilon)^{-1}$ where the backflow factor $\epsilon = G_{\text{int}}^{\text{SP}}(G_{\text{F}}^{-1} + G_{\text{N}}^{-1})$. We will discuss the relative magnitudes of these SCs when we apply our theory to a concrete multilayer.

4.3.2 Spin conductance of a temperature gradient spin battery

The spin Seebeck current across a FI/NM bilayer has been theoretically studied in different methods [113–116]. In this work, we follow the magnon diffusion theory used in Refs. [115, 116]. Far from the interface, the temperature gradient perpendicular to the interface drives a magnon current. The magnon current leads to a non-equilibrium magnon accumulation near the interface. In contrary to the spin pumping case where the non-equilibrium magnons only exists for $q = 0$, there is a broad magnon spectrum distribution. For the FI/NM interface, the interaction in the spin wave approximation is same as Eq. (4.8) and the expression of Eq. (4.10) remains valid. However, we need to replace the magnon distribution by,

$$N_{\mathbf{q}}^{\text{F}} = \frac{1}{e^{(E_{\mathbf{q}} - \mu_m(x))/k_B T} - 1} \quad (4.15)$$

where we have introduced the spatial dependent magnon chemical potential, $\mu_m(x)$. At equilibrium, $\mu_m(x)$ is identically zero. In the presence of magnon accumulation, $\mu_m(x)$ characterizes the number of the non-equilibrium magnons,

$$\delta n(x) \simeq g_m^{\text{F}}(T) \mu_m(x). \quad (4.16)$$

where $g_m^{\text{F}}(T) = - \int d\varepsilon g_m^{\text{F}}(\varepsilon) \partial_{\varepsilon} N_0(\varepsilon, T)$. By inserting the non-equilibrium distribution functions, $N_{\mathbf{q}}^{\text{F}}$ and $f_{\mathbf{k}\sigma} = f_0 - \frac{\partial f_0}{\partial E_{\mathbf{k}}} \mu_{\sigma}(0^+)$ into Eq. (4.10), we find the spin current at the interface is,

$$j_s^{\text{th,NM}}(0) = \frac{G_{\text{F/N}}^{\text{th}}}{2\pi} [\mu_m(0^-) - \mu_s(0^+)] \quad (4.17)$$

where $\mu_s(0^+) = \mu_{\uparrow}(0^+) - \mu_{\downarrow}(0^+)$ is the spin split chemical potential at the interface and

$$G_{\text{F/N}}^{\text{th}} = \frac{\pi^2 J_{\text{int}}^2 S_{\text{F}}}{k_B T} a_{\text{N}}^3 a_{\text{F}}^4 g_e(E_{\text{F}})^2 \int d\varepsilon_{\mathbf{q}} g_m^{\text{F}}(\varepsilon_{\mathbf{q}}) \varepsilon_{\mathbf{q}} \text{csch}^2 \frac{\varepsilon_{\mathbf{q}}}{2k_B T} \quad (4.18)$$

is the thermal driven interface spin conductance. If the temperature is lower than the Curie temperature of the FI, the SC reduces to a simple $T^{3/2}$ power law listed in Table 4.1. The inclusion of the backflow can be similarly done; the calculated backflow parameter ϵ has same forms as that of the spin pumping, with one distinction: in the present case, G_{F} is the spin conductance for the longitudinal spin current

(proportional to the magnon-diffusion length), while G_F in the spin pumping battery is for the transverse spin current where the spin dephasing length is much smaller.

The second interface for the thermally driven spin battery is the FI/AFI interface in which the thermal magnons in the FI transfer to the magnons in the AFI layer. In contrast to the spin pumping battery where the two magnon process is prohibited, the thermal magnons have a broad spectrum of the magnon energy in the FI layer and thus it is possible to directly transfer one FI magnon to one AFI magnon, i.e., the interface spin exchange interaction in the form of $J_{\text{int}}a_{\mathbf{q}}\alpha_{\mathbf{q}'}^+$ leads to a spin current across the interface,

$$j_s^{\text{th,AFI}} = \frac{2\pi J_{\text{int}}^2 S_F S_A}{A_I} \sum_{\mathbf{q}\mathbf{q}'} (\zeta_{\mathbf{q}'}^2 + \zeta_{\mathbf{q}}^{-2}) [N_{\mathbf{q}}^F (N_{\mathbf{q}'}^\alpha + 1) - (N_{\mathbf{q}}^F + 1) N_{\mathbf{q}'}^\alpha] \delta(\varepsilon_{\mathbf{q}}^F - \varepsilon_{\mathbf{q}'}^\alpha) \quad (4.19)$$

where $N_{\mathbf{q}}^F$ and $N_{\mathbf{q}'}^\alpha$ are the FI and AFI magnon distribution functions respectively. Notice that only the transmission from FI magnon to the α_q branch of AFI magnon can conserve energy and angular momentum at the same time. Following the similar procedure in deriving the SC of FI/NM spin interface, we find the interface current

$$j_s^{\text{th,AFI}}(0) = \frac{G_{\text{F/A}}^{\text{th}}}{2\pi} [\mu_m(0^-) - \mu_m(0^+)] \quad (4.20)$$

where $\mu_m(0^{-/+})$ measures the non-equilibrium FI/AFI magnon accumulation at the interface, and the interface conductance is

$$G_{\text{F/A}}^{\text{th}} = \frac{\pi^2 J_{\text{int}}^2 S_F S_A}{k_B T} a_F^2 a_A^2 \int d\varepsilon_{\mathbf{q}} (\zeta_{\mathbf{q}}^2 + \zeta_{\mathbf{q}}^{-2}) g_m^F(\varepsilon_{\mathbf{q}}) g_m^A(\varepsilon_{\mathbf{q}}) \text{csch}^2 \frac{\varepsilon_{\mathbf{q}}}{2k_B T} \quad (4.21)$$

4.3.3 Spin conductance with the spin Hall battery

The sources of the spin current in previous two batteries reside in the FI layer. We next consider a non-magnetic layer with a large spin Hall angle as a spin battery. As we have introduced earlier, an in-plane charge current creates a spin voltage in the direction of $\hat{\mathbf{z}} \times \mathbf{j}_e$ due to the spin Hall effect. For a ferromagnetic layer in contact with the spin Hall battery, the spin current would depend on the relative direction between the magnetization \mathbf{m} and the spin voltage. If \mathbf{m} is perpendicular to the spin voltage $\hat{\mathbf{z}} \times \mathbf{j}_e$, the spin current entering the ferromagnetic layer decays within very small length, resulting a spin torque at the interface. This spin conductance at the FI/NM interface is the same as the mixing conductance defined in Eq. (4.12). There are quite extensive studies on the magnetization switching by the spin Hall

current [66, 119]. In the case where $\mathbf{m} \parallel \hat{\mathbf{z}} \times \mathbf{j}_e$, the spin Hall battery creates non-equilibrium magnons in the FI layer. The spin conductance for the parallel case is identical to the $G_{\text{F/N}}^{\text{th}}$ shown in Eq. (4.18). Both spin conductances have been already calculated previously [16, 17], we have listed them in Table 4.1. Here we present the calculation for the NM/AFI interfaces.

The Hamiltonian in Eq. (4.7) within the spin wave approximation is

$$H_{\text{int}} = -J_{\text{int}} \sqrt{2S_A} \sum_{\mathbf{k}\mathbf{k}'\mathbf{q}} [\zeta_{\mathbf{q}}(\alpha_{\mathbf{q}}^+ + \beta_{\mathbf{q}})c_{\mathbf{k}\downarrow}^+ c_{\mathbf{k}',\uparrow} + H.c.] \delta_{\mathbf{k}',\mathbf{k}+\mathbf{q}} + [\zeta_{\mathbf{q}}^{-1}(\alpha_{\mathbf{q}}^+ - \beta_{\mathbf{q}})c_{\mathbf{k}\downarrow}^+ c_{\mathbf{k}',\uparrow} + H.c.] \delta_{\mathbf{k}',\mathbf{k}+\mathbf{q}+\mathbf{G}} \quad (4.22)$$

where the first term is normal scattering, the second term stands for the Umklapp scattering [109] and \mathbf{G} is half of the reciprocal NM lattice vector. Again, we don't impose the momentum conservation at the interface in the following calculation. The angular momentum current across the interface is

$$j_s = \frac{2\pi J_{\text{int}}^2 S_A}{N_A N_N A_I} \sum_{\mathbf{k}\mathbf{k}'\mathbf{q}} (\zeta_{\mathbf{q}}^2 + \zeta_{\mathbf{q}}^{-2}) [(N_{\mathbf{q}}^{\alpha} + 1)(1 - f_{\mathbf{k}\uparrow})f_{\mathbf{k}'\downarrow} - N_{\mathbf{q}}^{\alpha} f_{\mathbf{k}\uparrow} (1 - f_{\mathbf{k}'\downarrow})] \delta(\varepsilon_{\mathbf{k}} + \varepsilon_{\mathbf{q}}^{\alpha} - \varepsilon_{\mathbf{k}'}) - (\zeta_{\mathbf{q}}^2 + \zeta_{\mathbf{q}}^{-2}) [(N_{\mathbf{q}}^{\beta} + 1)f_{\mathbf{k}\uparrow}(1 - f_{\mathbf{k}'\downarrow}) - N_{\mathbf{q}}^{\beta} (1 - f_{\mathbf{k}\uparrow}) f_{\mathbf{k}'\downarrow}] \delta(\varepsilon_{\mathbf{k}} - \varepsilon_{\mathbf{q}}^{\beta} - \varepsilon_{\mathbf{k}'}) \quad (4.23)$$

By placing the non-equilibrium distribution of the battery into Eq. (4.23), we find,

$$G_{\text{N/A}}^{\text{th}} = \frac{2\pi^2 J_{\text{int}}^2 S_A}{k_B T} g_e^2(E_F) a_N^4 a_a^3 \int d\varepsilon_{\mathbf{q}} (\zeta_{\mathbf{q}}^2 + \zeta_{\mathbf{q}}^{-2}) g_m^A(\varepsilon_{\mathbf{q}}) \varepsilon_{\mathbf{q}} \text{csch}^2\left(\frac{\varepsilon_{\mathbf{q}}}{2k_B T}\right). \quad (4.24)$$

The above SC is applied to the case when the spin battery is parallel to the staggered magnetization of the AFI. The superscript ‘‘th’’ (thermal) indicates the above spin conductance involves the spin convertance between conduction electrons and magnons across the whole spectrum instead of only the $k = 0$ mode. When they are perpendicular, a spin current driven spin torque on the AFI has been proposed; this will involve the coherent AFI magnon generation by the spin Hall battery [109].

4.4 Spin current enhancement via insertion of thin NiO layer

In Table 4.1, we have listed the interface spin current and conductance of bilayers with semi-infinite thickness for each layer. Experimentally, there can be more than two layers whose thicknesses are comparable to the spin or magnon decaying length. Furthermore, experiments are usually carried out at room temperature which is not

much lower than the Curie or Néel temperatures. For example, the spin current with a thin NiO is largest near the Néel temperature [20, 103, 104]. Thus, in the following, we describe how the interface SCs in Table 4.1 are applied to multilayers with finite thickness and how these SCs changes at temperatures near or above critical temperatures.

4.4.1 Boundary conditions for spin currents in multilayers

Similar to the electron spin transport in metallic multilayers, we need boundary conditions and the spin/magnon diffusion equations within each layer. The SC in Table 4.1 will be used as boundary conditions at $x = 0$,

$$j_s(0^+) = j_s(0^-) = \frac{G_{\text{int}}}{2\pi} [\mu(0^+) - \mu(0^-)] \quad (4.25)$$

where G_{int} is the interface SC for a particular interface, and $\mu(0^+)$ [$\mu(0^-)$] represents the chemical potential of the electrons or magnons at the right [left] interface. Within each layer, including the battery layer, the spin current is given by

$$j_s(x) = j_b(x) - \sigma \frac{d\mu(x)}{dx} \quad (4.26)$$

where $j_b(x)$ is the source spin current in the battery layer and is zero elsewhere. To illustrate how these boundary conditions along with the diffusion equations determine the spin current in the entire multilayers, we take an example of a trilayer consisting of FI/AFI/NM, driven by a temperature gradient battery across the FI layer. The spin/magnon chemical potentials in each layer has the following forms: $\mu_m = C_1 \exp(x/\lambda_F)$ in the FI layer ($x < 0$), $\mu_m(x) = C_2 \exp(-x/\lambda_A) + C_3 \exp(x/\lambda_A)$ in the AFI layer ($0 < x < d_A$) and $\mu_s(x) = C_3 \exp(-x/\lambda_N)$ in the NM layer ($x > d_A$) where d_A is the thickness of the AFI layer, λ_F , λ_A , and λ_N are the diffusion lengths in each layers. of the AFI layer. By using the boundary conditions, Eq. (4.25) for the interfaces FI/AFI and AFI/NM at $x = 0$ and $x = d_A$, four constants of integration C_i ($i = 1 - 4$) are readily determined. While the expression of the spin current is rather lengthy and cumbersome for an arbitrary thickness of the AFI, it takes a particularly simple form if we assume 1) the thickness of the AFI is much smaller than λ_A so that there is no spin current decay in the AFI layer, and 2) the interface spin conductance of the FI/AFI is much larger than that of the NM/AFI interface. We find the spin current in the NM layer is

$$\mathbf{j}_s^{\text{tri}}(x) = \frac{G_{\text{N/A}}^{\text{th}} \exp(-x/\lambda_N)}{1 + G_{\text{N/A}}^{\text{th}}/G_{\text{F}} + G_{\text{N/A}}^{\text{th}}/G_{\text{N}}} \frac{\mathbf{V}_{\text{th}}}{2\pi} \quad (4.27)$$

If we further approximate the FI as a good spin sink so that one may neglect the second term in the denominator [116]. Comparing the spin current above to that of the bilayer FI/NM, i.e., without the AFI insertion, we have

$$\eta_{\text{th}} \equiv \frac{j_s^{\text{tri}}}{j_s^{\text{bi}}} = 1 + \frac{(a-1)G_{\text{N}}}{G_{\text{N/A}}^{\text{th}} + G_{\text{N}}} \quad (4.28)$$

where

$$a = \frac{G_{\text{N/A}}^{\text{th}}}{G_{\text{F/N}}^{\text{th}}} = C' \left(\frac{J_{\text{NiO/Pt}}}{J_{\text{YIG/Pt}}} \right)^2 \left(\frac{T}{T_{\text{N}}} \right)^2 \left(\frac{T}{T_c} \right)^{-3/2} \quad (4.29)$$

C' is a numerical constant of the order of 1, $J_{\text{NiO/Pt}}$ and $J_{\text{YIG/Pt}}$ are the interface exchange constants and we have used the interface SC of Table 4.1.

Interestingly, if $a \gg 1$, i.e., the spin conductance for NiO-Pt interface is much larger than YIG-Pt interface, the enhancement with an AFI layer insertion is significant and the largest occurs at high temperatures. We will further address the enhancement in the next subsection. Next, we consider the same trilayer structure by replacing the thermal battery with a spin pumping battery. Within the same approximation, the spin current in the NM layer is

$$\mathbf{j}_s^{\text{sp,tri}}(x) = \frac{\hbar}{4\pi} \frac{G_{\text{F/A}}^{\text{sp}} \exp(-x/\lambda_{\text{N}})}{1 + G_{\text{F/A}}^{\text{sp}}/G_{\text{N/A}}^{\text{th}} + G_{\text{F/A}}^{\text{sp}}/G_{\text{N}}} \mathbf{m} \times \frac{d\mathbf{m}}{dt}. \quad (4.30)$$

Notice that at the YIG/NiO interface, the battery is magnetization precession in the YIG layer. Thus, we use $G_{\text{F/A}}^{\text{sp}}$ as the interface conductance. At the NiO/Pt interface, the spin battery is the magnon accumulation with broad wave number distribution, and the interface spin conductance is given by $G_{\text{N/A}}^{\text{th}}$. Again, the spin pumping current vanishes at low temperature, reflecting the fact that magnon or spin current is blocked by either the FI/AFI or AFI/NM interface at low temperatures. The spin current enhancement with the AFI layer is,

$$\eta_{\text{sp}} = 1 + \frac{(b-1)(G_{\text{N}} + G_{\text{F/N}}^{\text{sp}})}{G_{\text{F/A}}^{\text{sp}} \left(1 + G_{\text{N}}/G_{\text{N/A}}^{\text{th}} \right) + G_{\text{N}}} \quad (4.31)$$

where $b = G_{\text{F/A}}^{\text{sp}}/G_{\text{F/N}}^{\text{sp}}$.

4.4.2 Modeling spin current at elevated temperatures

As our theory is built on the spin wave approximation, one would expect the theory not applicable to high temperatures, in particular, near the transition temperature.

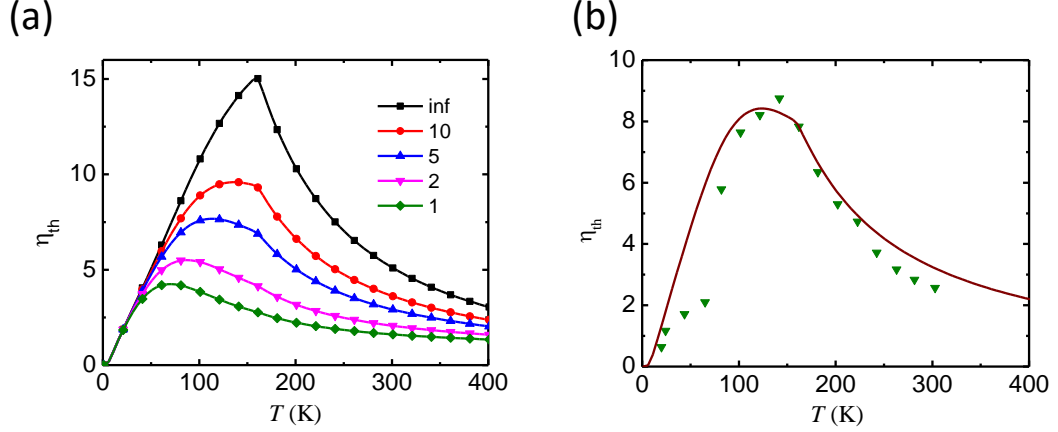


FIGURE 4.2. The spin Seebeck signal enhancement factor, η_{th} , as a function of temperature for various spin conductance of the NM layer from $G_N = 1, 2, 5, 10, \infty$ (10^{18}m^{-2}), calculated by using Eq. (4.28). The parameters are $a_F = 1.39$ nm, $a_A = 0.42$ nm, $T_C = 560$ K, $T_N = 160$ K ($t_{\text{NiO}} = 0.6$ nm), $g_e(E_F) = 3n_e/2E_F$ with $n_e = 5 \times 10^{22} \text{cm}^{-3}$ and $E_F = 5$ eV. $J_{\text{YIG/Pt}} = 0.07$ eV and $J_{\text{NiO/Pt}} = 0.13$ eV are the sd constant at the interface. (a) The enhancement factor for a number of spin conductance of the NM layer. (b) Comparison of the experimental points [20] with the theoretical curve for $G_N = 6.7 \times 10^{18} \text{m}^{-2}$.

However, the most interesting features with the AFI layers discovered experimentally occur at a temperature near or even above the Néel temperature [20, 103]. Thus, it is desirable to extend the formalism with reasonably approximations.

The spin transport near transition temperatures is in general an unresolved theoretical issue. While there are a number of approximate methods to treat the critical phenomena, no rigorous theory exists for a wide range of temperatures. Here we should remain to use the spin wave approximation with one limitation: above the transition temperature, the spin wave approximation breaks down since spin correlation length becomes finite. In early theories and neutron scattering experiments, it was indeed found that the spin wave with long wavelengths loses its meaning, but the short wavelength magnon remains intact [120, 121]. For example, the spin correlation length of NiO is

$$\iota = l \left(\frac{T - T_N}{T_N} \right)^{-\nu} \quad (4.32)$$

where $l = 1.2a_{\text{NiO}}$, $a_{\text{NiO}} = 0.42$ nm is the lattice constant of NiO and $\nu = 0.64$ [121].

The magnon whose wavelength is shorter than ι has well-defined dispersion relation [120], indicating the presence of short-range AF spin correlations. We thus modify our spin wave approximation by assuming a cutoff energy $\hbar\omega_{q_c}$ where $q_c = 1/\iota$ such that $N_q = 0$ for $q < q_c$. When the temperature increases, the long wavelength magnons do not participate transport. With this modification, we are able to address the spin current propagation for a wide range of temperatures.

As an example, we consider the same FI/AFI/NM (YIG/NiO/Pt) trilayer. At high temperatures, we no longer use Table 4.1 for the interface SC. Instead, we will use the general expression, Eqs. (4.18) and (4.24) by placing the cutoff energy as a lower bound of the integration. In Fig. 4.2(a), we show the spin current enhancement as a function of the temperature for a thermal battery for different NM spin conductance. As the temperature increases, the number of magnons and the interface conductance increase, thus the spin current, mediated by the magnons in the AFI layer increases. When the temperature reaches to the Néel temperature of the AFI (Note that the Curie temperature of YIG is much higher), the number of magnons participating the angular momentum transport begins to decrease due to removing of the long wavelength magnons. Meanwhile, the spin current in the bilayer structure keeps increasing with temperature when $T_N < T < T_C$. Thus, both the spin conductance $G_{N/A}^{\text{th}}$ and the enhancement factor η_{th} are maximum near the Néel temperature. We notice that spin current peak at the transition temperature has been obtained by Okamoto by using a different approach [124]. The enhancement is reduced as the NM layer SC decreases due to enhanced back flow, consistent with Eq. (4.29). Interestingly, the peak position occurs at a lower temperature for smaller SC of the NM layer; this can be explained as follows. When $G_{N/A}^{\text{th}}$ becomes larger than G_N , the spin current in the YIG/NiO/Pt trilayer saturates, while for the YIG/Pt bilayer, spin current continues to increase with temperature since $G_{N/F}^{\text{th}}$ remains smaller than G_N . Notice that the calculated η_{th} deviates the $T^{1/2}$ law even at low temperatures due to the large AF magnon gap. In Fig. 4.2(b), we compare our calculations with G_N measured in previous publication [41]; the agreement is considered to be excellent [20].

4.4.3 Discussions and conclusions

We have developed a theory based on spin current transfer at interfaces. The different spin current carriers are mutually converting via an interfacial spin exchange Hamiltonian. Within the spin wave approximation, we are able to explicitly formulate the SC for different sources of the spin current (spin batteries) and for different interfaces at finite temperature.

We point out that the SC studied here is for quasi-particle spin transport, i.e., the spin current carriers are incoherent low-energy quasiparticles, which is different from the “super-current” carried by the macroscopic classical magnetization (coherent magnons), or the order parameter. For the quasiparticle transport, the quantum statistics governs the temperature dependent properties. In general, both incoherent and coherent magnons contribute to the spin transport.

Our theory is particularly effective to be used for multilayered structure at finite temperature with arbitrary layer thickness. Using the diffusion equation for each layer along with the interface SCs, one is able to determine the spatial and temperature dependence of the spin current. The spin battery, which is an extension of the spin pumping battery introduced earlier [112], is a convenient concept that can be used to describe the spin current flow. In analogy with an electric battery: the spin battery has just one terminal while the electrical battery must have at least two terminals because of the conservation law imposed to the charge current. The non-conservative nature of spin current has also been studied by Camsari *et al.* in a recent publication [125]. For the spin battery, one can still use spin Ohm’s law, i.e., $dV_s(x)/dx = j_s(x)G_s^{-1}(x)$ where $G_s^{-1}(x)$ is a local spin resistivity. Due to non-conservative nature of the spin current, the spin current $j_s(x)$ is no longer a constant throughout the layers. Thus, the spin Ohm’s law alone (even if G_s is known) cannot determine the spin current. In this paper, we have provided a general scheme for computing the spin current.

Our theory provides a natural explanation to the temperature dependence of current propagation through FI and AFI insulators. Recent experiments on Pt/YIG/Pt have confirmed our earlier prediction [16]. The spin current enhancement by inserting a thin NiO layer at the interface of the YIG/NM [20, 103], quantitatively supports our theory. The other theories based on the order parameter spin transport [122, 123] have not taken into account finite temperature effects.

4.5 Other Remarks

4.5.1 Magnon density vs Magnon chemical potential

In Eq. (4.17) and (4.18), we build the boundary condition for a metal/FI interface where there are thermal incoherent magnons in ferromagnetic layers. In [16, 115], the same case has been addressed using similar method. In their result, the magnon accumulation is denoted by spin density instead of chemical potential.

Here, we choose to use the magnon chemical potential which allows us to write the interface spin conductance just like contact conductance. A large interface spin conductance leads to the continuity of chemical potentials at two sides of the interface. While using spin density to address the magnon accumulation, one has to introduce two different interface conductances [16] which makes the boundary conditions more tedious. However, the magnon chemical potential can be ill defined in some cases which makes the current formalism troublesome. Consider a ferromagnetic magnon band, the magnon chemical potential can be calculated using the magnon density of states,

$$\mu_m = \delta n / g_m^F(T) \quad (4.33)$$

where δn is the non-equilibrium density and $g_m^F(T)$ is the magnon density of states defined below Eq. (4.16). For a gapless quadratic magnon band, $g_m^F(T)$ diverges. Even such an issue is well known, magnon chemical potential is still used in many theoretical works including ours.

4.5.2 Different formalism of spin pumping

In current and previous chapters, we have mentioned four different formulas for spin pumping which are summarized below. For comparison, we only consider the dc part of the spin pumping current. In the original spin pumping theory [25], the spin current is calculated using mixing conductance?

$$j_s^{\text{SP}} = \frac{\hbar}{4\pi} g_{\text{mix}} \omega \sin^2 \theta \quad (4.34)$$

In another paper [93], Ohnuma *et al.* calculate the spin pumping into ferromagnetic metals. The spin current is expressed in terms of susceptibility of the metal,

$$j_s^{\text{SP}} = \frac{J_{sd}^2 S^2}{\hbar^2} \sum_k \frac{\text{Im} \chi_k(\omega)}{\omega} \omega \sin^2 \theta. \quad (4.35)$$

In our work, we proposed the real space Green's function approach and the spin conductance formula Eq. (4.11).

In Chapter 2, we have demonstrated that the equivalence between our Green's function approach and the mixing conductance in the limiting case. By replacing the susceptibility in Eq. (4.35) with Lindhard susceptibility one can show that the result is identical to our spin conductance formula. In Ref. [93], the authors show that their results are identical to the mixing conductance in the nonmagnetic case. Though all results are identical in the limiting case, one should find one of them more convenient in some particular cases.

CHAPTER 5

SPIN TRANSPORT IN WEAK SCATTERING MEDIA IN THE PRESENCE OF SPIN-ORBIT COUPLING

Conventional spin diffusion equation, based on the presence of spin-split local chemical potentials, has successfully described spin accumulation attendant to diffusive transport in spintronics. Recent experiment shows that spin accumulation far exceeds the limit set by such spin diffusive theory when the mean free path is longer than the spin dephasing length. By introducing the momentum and spin dependent chemical potential, we develop a generalized spin transport equation that is capable of addressing spin transport in systems where ballistic processes are embedded in the overall diffusive conductor. We find that the ballistic spin injection through a barrier into a diffusive non-magnetic layer with strong spin-orbit coupling can enhance spin accumulation by an order of magnitude when compared to the conventional theory.

5.1 Spin diffusion equation and spin injection into disordered medium

Spin accumulation (SA), a non-equilibrium spin density created by external sources such as spin injection across a tunnel barrier, and spin currents (SC), the difference between the electric currents carried by spin up and down electrons, play central roles in spintronics. At present, the macroscopic description of SA and SC relies on the spin diffusion equation in which the spatial and temporal dependence of SA, $\mathbf{m}(\mathbf{r}, t)$, satisfies,

$$\frac{\partial \mathbf{m}}{\partial t} = D \nabla^2 \mathbf{m} - \frac{\mathbf{m}}{\tau_{sf}} \quad (5.1)$$

and the diffusion SC is given by the spin-dependent Ohm's law, $\mathbf{j}_s = -D \nabla \mathbf{m}$ where D is the diffusion constant and τ_{sf} is the spin flip scattering time. It is understood that the above equation can be used to determine the local SA and SC at length scales larger than the mean free path (MFP) [79, 126]. While Eq. (5.1) has been successfully applied to explain and predict spin transport phenomena in almost all spintronic devices [5], recent experimental result has challenged the validity of this theory: the SA could be much larger than that predicted by Eq. (5.1) when the

distance between the spin injector and detector in a non-local spin-valve geometry is less than the mean free path [27, 128].

Before introducing the new spin injection experiment results, we first go through the conventional spin injection experiments and results. In Fig. 5.1, we show the illustration of spin injection in lateral spin valve. The spin valve consists of a charge current source, a voltmeter, a spin injector, a spin detector and a non-magnetic channel which is the gray layer at the bottom. The spin injector polarizes the charge current injected into the NM channel, which in turn builds up a spin accumulation in the NM channel. Such spin accumulation can be detected by the voltmeter, the magnitude depends on the relative direction of the magnetization of the spin injector and spin detector. When we sweep a magnetic field from large negative to large positive, the relative direction between the magnetization of the spin injector and spin detector changes from parallel to antiparallel, and then back to parallel.

In Fig. 5.1(b), we show the typical reading of the voltmeter when sweeping the magnetic field, where $R_s = V/I_c$ is the voltage normalized by the charge current. The peak height of in R_s has been calculated based on the spin diffusion equation [131]

$$R_s = p_j p_d \rho \lambda A^{-1} \exp(-L/\lambda) \quad (5.2)$$

where $p_{j/d}$ is the spin current polarization at the spin injector/detector, and ρ is the resistivity of the NM material at bottom, λ is the spin diffusion length of NM material, A the cross-area and L is the distance between spin injector and spin detector.

In [27], the author reported the results on similar spin injection experiments. They use a high mobility 2 dimensional electron gas as the NM channel, and a magnetic tunneling contact as both spin injector and spin detector. When using above equation to estimate the spin current polarization at the injector, 650% was obtained while the polarization of a charge current should never exceeds 100%. Another controversy reported is that the observed spin diffusion length is even smaller than the electron mean free path which can be deduced from material conductivity and electron density. This finding calls for a new theory beyond the conventional spin diffusion equation. Several earlier attempts [129–132] by incorporating quantum and ballistic effects have not been able to predict an enhanced spin accumulation in the ballistic regime.

Recall that the above spin diffusive equation was established based on the assumption that the SDL is much larger than MFP, it would be inevitably fails in the opposite limit: the spin-dependent local chemical potentials (LCP) without specifying the direction of electron momentum becomes meaningless. In ballistic transport in which the relevant spatial length is shorter than the mean free path, the LCP is

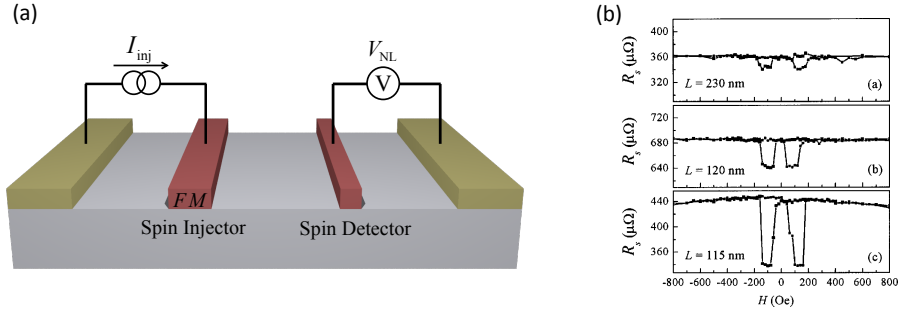


FIGURE 5.1. Illustration of spin injection in lateral spin valve. In subfigure (a), we show the structure of a lateral spin valve. (b) shows the typical results of spin injection results taken from [127] where L is the distance between spin injector and spin detector.

ill-defined since the “chemical potential” (CP) of electrons at a given spatial point depends on the direction of electron momentum. If the entire system is ballistic, the standard mesoscopic transport assumption would be that the left-going (right-going) electrons has a CP of the right (left) reservoir [30]. To address the SA within the length scale of mean free path, the ballistic nature of the transport must be included. One attempt would be completely giving up the concept of chemical potentials and instead, directly solve the distribution function from the generalized semiclassical integro-differential Boltzmann equation. Such approach is numerically complicated in general, and the obtained numerical results may not give arise significant physical insight. Alternatively, we derive a set of useful macroscopic spin transport equations, similar to Eq. (5.1), but take into account ballistic processes embedded in a diffusive conductor. The key component is to introduce the *spin and directional dependence of the LCP*, namely, the left-going and right-going electrons have different CPs, in addition to the spin-dependent CP. We find that macroscopic equations of these CPs can be established by approximately solving the spinor Boltzmann equation in the presence of spin-orbit coupling (SOC), e.g., of the Dresselhaus form. The new spin ballistic-diffusion equations are solved for the spin injection from a magnetic tunnel junction to a non-magnetic (NM) layer. We show that the SA in the NM layer can largely exceed the classical limit set by the conventional spin diffusion theory when the mean free path is longer than the spin-orbit coupling induced spin dephasing length. Our calculated results successfully explain recent experimental observations [27].

The Chapter is organized as follows. In Sec. 5.2, we start from the Boltzmann

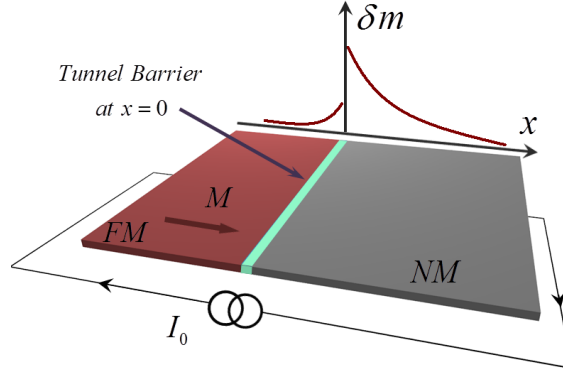


FIGURE 5.2. A model bilayer consists of a ferromagnet and a non-magnetic metallic layer separated by a tunnel barrier at $x = 0$. The spin-dependent transmission and reflection coefficients are T_σ and R_σ . The spin accumulation at both sides of the barrier is also shown and will be quantitatively calculated.

equation and derive the spin transport equations within a 2d electron gas (2DEG) in the presence of Dresselhaus SOC. In Sec. 5.3, by utilizing our newly derived spin transport equations together with appropriate boundary conditions, we study the spin injection into a 2DEG across a tunnel barrier. Compared to the spin injection into a diffusive material, we find that there is an enhancement of the spin accumulation when the mean free path is larger than the spin relaxation length within the 2DEG.

5.2 Spin transport equation in ballistic medium

We start by considering a simple bilayer structure shown in Fig. 5.2 where a ferromagnetic (FM) layer injects spin-polarized electrons into a NM 2DEG through a tunnel barrier and we determine the SA in the NM 2DEG. An example of this layered structure is $\text{Ga}_{1-x}\text{Mn}_x\text{As}$ as the FM layer, $(\text{Al,Ga})\text{As}/\text{GaAs}$ interface as the NM layer, and tunnel barrier between them can be either a Schottky barrier or an insulator film spacer. Note that the actual experimental geometry in Ref. [27] involves a non-local spin valve for the measurement of the SA. The steady-state spinor distribution $\hat{F}(x, \mathbf{k})$ in the NM layer satisfies the Boltzmann equation [133],

$$\hat{v}_x \frac{\partial \hat{F}}{\partial x} + \frac{eE}{m} \frac{\partial \hat{F}}{\partial v_x} - \frac{1}{i\hbar} [\hat{H}_{SO}, \hat{F}] = -\frac{\hat{F} - \bar{F}}{\tau_m} - \frac{\bar{F} - (1/2)\hat{I}\text{Tr}(\bar{F})}{\tau_{sf}} \quad (5.3)$$

where E is the electric field in x - direction, $\hat{H}_{SO} = (\hbar/2)\mathbf{\Omega}_\mathbf{k} \cdot \hat{\boldsymbol{\sigma}}$ is the Hamiltonian for the spin-orbit coupling, the bar over F indicates an average over the momentum,

τ_m and τ_{sf} are momentum and spin relaxation times due to impurity scattering, and \hat{I} is the 2×2 unit matrix. In the presence of SOC, the velocity is a spinor $\hat{v}_x = \hbar k_x \hat{I} + \partial \hat{H}_{SO} / \partial k_x$ which leads to spin-charge transport coupling, namely, the charge density and charge current are dependent on the spin density and spin current, and vice versa. In Eq. (5.3), $\hat{v}_x \frac{\partial \hat{F}}{\partial x}$ stands of the anti-commutator, $\frac{1}{2} \{ \hat{v}_x, \frac{\partial \hat{F}}{\partial x} \}$. In Ref. [134] and [135], a set of coupled spin and charge transport equations in a diffusive conductor have been derived. In the present work, we first simply take $v_x = \hbar k_x$ in Eq. (5.3) such that the spin and charge currents are not coupled. We show in Appendix B.1 that the spinor velocity could be included but the resulting transport equations are far more cumbersome. Since our present focus is on the ballistic contribution to spin accumulation and spin current, we consider the limit that spin-orbit coupling remains small compared to the Fermi energy, i.e., $E_{SO}/E_F \ll 1$ such that the charge and spin transport are separated, as shown in Appendix B.1.

One may explicitly separate the equilibrium F_0 and non-equilibrium parts of the distribution function,

$$\hat{F} = F_0 \hat{I} + \left(-\frac{\partial F_0}{\partial \varepsilon} \right) \left(f_0 \hat{I} + \mathbf{f}_1 \cdot \boldsymbol{\sigma} \right) \quad (5.4)$$

where f_0 and \mathbf{f}_1 characterize the spin-independent and spin-dependent parts of the non-equilibrium distributions. By placing Eq. (5.4) into Eq. (5.3), and only keeping the term linear in the electric field, one finds,

$$v_x \frac{\partial f_0}{\partial x} + eE v_x = -\frac{f_0 - \bar{f}_0}{\tau_m} \quad (5.5)$$

$$v_x \frac{\partial \mathbf{f}_1}{\partial x} - \boldsymbol{\Omega}_{\mathbf{k}} \times \mathbf{f}_1 = -\frac{\mathbf{f}_1 - \bar{\mathbf{f}}_1}{\tau_m} - \frac{\bar{\mathbf{f}}_1}{\tau_{sf}}. \quad (5.6)$$

To establish macroscopic equations for SA and SC from the above integro-differential equation, Eq. (5.5) and (5.6), for arbitrary ratios of the mean free path and spin dephasing length, we introduce left-going and right-going CPs for spin and charge,

$$f_0 = \mu_0^>(x)\theta(k_x) + \mu_0^<(x)\theta(-k_x) - g_0(k_x, x), \quad (5.7)$$

$$\mathbf{f}_1 = \boldsymbol{\mu}_1^>(x)\theta(k_x) + \boldsymbol{\mu}_1^<(x)\theta(-k_x) - \mathbf{g}_1(k_x, x) \quad (5.8)$$

where $\theta(k_x)$ is a step-function; thus we identify $\mu_c \equiv (\mu_0^> + \mu_0^<)/2$ as the CP of charge and $\mu_{cb} \equiv \mu_0^> - \mu_0^<$ is the ballistic component of the CP. Similarly, we define that $\boldsymbol{\mu}_s \equiv (\boldsymbol{\mu}_1^> + \boldsymbol{\mu}_1^<)/2$ is the spin CP and $\boldsymbol{\mu}_b \equiv \boldsymbol{\mu}_1^> - \boldsymbol{\mu}_1^<$ is its ballistic part, see Appendix

B.1. Next, we specify the spin-orbit coupling $\mathbf{\Omega}_{\mathbf{k}}$. For systems with either structure-inversion or bulk-inversion symmetry-breaking, $\mathbf{\Omega}_{\mathbf{k}}$ is usually taken as linear with respect to the momentum \mathbf{k} , i.e., $\mathbf{\Omega}_{\mathbf{k}} = 2\alpha/\hbar(\mathbf{k} \times \hat{\mathbf{z}})$ for the Rashba Hamiltonian, and $\mathbf{\Omega}_{\mathbf{k}} = 2\alpha/\hbar(k_x, -k_y, 0)$ for the Dresselhaus Hamiltonian where α is the Rashba or Dresselhaus constant. By placing the above definitions in Eqs. (5.5) and (5.6), we have shown in the Appendix B.1 that following macroscopic equations can be obtained for the Dresselhaus SOC (similarly for Rashba SOC),

$$\frac{d^2}{dx^2}\boldsymbol{\mu}_b - \frac{2}{\lambda} \frac{d}{dx}(\hat{\mathbf{e}}_x \times \boldsymbol{\mu}_b) = \frac{1}{l_{eff}^2}\boldsymbol{\mu}_b + \frac{1}{\lambda^2}(\hat{\mathbf{e}}_z \cdot \boldsymbol{\mu}_b)\hat{\mathbf{e}}_z \quad (5.9)$$

and

$$\frac{d^2}{dx^2}\boldsymbol{\mu}_s - \frac{2}{\lambda} \frac{d}{dx}(\hat{\mathbf{e}}_x \times \boldsymbol{\mu}_s) = \frac{1}{\lambda^2}[\boldsymbol{\mu}_s + (\hat{\mathbf{e}}_z \cdot \boldsymbol{\mu}_s)\hat{\mathbf{e}}_z] + \frac{1}{2l_0} \frac{d}{dx}\boldsymbol{\mu}_b - \frac{1}{2l_0\lambda}\hat{\mathbf{e}}_x \times \boldsymbol{\mu}_b \quad (5.10)$$

where $l_0 = v_F\tau_m/\sqrt{2}$ is the mean free path, $\lambda \equiv \hbar^2/2(m_e\alpha)$ is the spin dephasing length due to spin-orbit coupling, and $l_{eff} = (1/l_0^2 + 1/\lambda^2)^{-1/2}$ is the effective mean free path (EMFP).

One immediately notes from Eq. (5.9) that the ballistic spin-dependent potential $\boldsymbol{\mu}_b$ has a length scale determined by the EMFP. In the weak spin-orbit coupling limit where $l_0 \ll \lambda$, or $l_{eff} \approx l_0$, the ballistic CP approaches zero beyond the length scale of l_0 while the spin CP or spin diffusion survives up to a larger scale of the order of λ . This is the conventional scenario. In the opposite limit where $l_0 \gg \lambda$, the ballistic CP and the spin CP have a common length scale, $l_{eff} \approx \lambda$.

The salient feature of spin ballistic-diffusion equation, Eq. (5.10), is that the spin CP $\boldsymbol{\mu}_s$ depends on the ballistic components of the chemical potential $\boldsymbol{\mu}_b$. In addition to the precession term, Eq. (5.10) contains the gradient of $\boldsymbol{\mu}_b$, indicating that the SA within the length scale of l_{eff} could differ from that of the conventional theory.

The presence of the ballistic CP also modifies the spin-dependent Ohm's law. The SC \mathbf{j}_s and the SA $\delta\mathbf{m}$ can be expressed in terms of these CPs, see Appendix B.1,

$$\mathbf{j}_s\rho = -\frac{d\boldsymbol{\mu}_s}{dx} + \frac{\boldsymbol{\mu}_b}{2l_0} + \frac{1}{\lambda}\hat{\mathbf{e}}_x \times \boldsymbol{\mu}_s \quad (5.11)$$

$$\delta\mathbf{m} = \boldsymbol{\mu}_s - \frac{l_0}{2} \frac{d\boldsymbol{\mu}_b}{dx} + \frac{l_0}{2\lambda}\hat{\mathbf{e}}_x \times \boldsymbol{\mu}_b \quad (5.12)$$

where ρ is the Drude resistivity.

Equations (5.9) and (5.10), along with (5.11) and (5.12), are generalizations of the macroscopic spin diffusion and spin-dependent Ohm's law. The crucial ingredient is

the existence of the ballistic CPs. If one places $\mu_b = 0$, these equations are identical to the conventional results. How and when does μ_b becomes non-zero? For a mesoscopic system where the sample size is smaller than the mean free path, μ_b naturally exists since there is no scattering to establish a well-defined local potential in the sample, i.e., the left-going electrons have the CP of the right reservoir while the right-going electrons have the CP of the left reservoir. For a diffusive conductor, such as magnetic metals, μ_b is identically zero inside the sample. For magnetic tunnel junctions where a tunnel barrier is imbedded in the diffusive layers, as shown in Fig. 5.2, μ_b is non-zero in the vicinity of the tunnel barrier because the transport across the barrier is governed by the quantum (ballistic) tunneling rather than diffusive scattering. To determine μ_b in this bilayer system, a set of boundary conditions are needed.

5.3 Spin injection into ballistic medium

In this section, we study the spin injection into a 2DEG across a tunnel barrier characterized by the spin dependent transmission and reflection coefficients T_σ and R_σ where $\sigma = \uparrow, \downarrow$ and $T_\sigma + R_\sigma = 1$. In principle, these coefficients are momentum dependent as well. For our macroscopic description, we simply consider them as their average values. Within the ballistic picture, the CPs for the incoming and outgoing electrons are related by these coefficients,

$$\mu_\sigma^>(+0) = T_\sigma \mu_\sigma^>(-0) + R_\sigma \mu_\sigma^<(+0) \quad (5.13)$$

and

$$\mu_\sigma^<(-0) = T_\sigma \mu_\sigma^<(+0) + R_\sigma \mu_\sigma^>(-0). \quad (5.14)$$

The next boundary condition involves the definition of contact resistance at the interface that connects the spin current to the CPs between the left and right sides of the interface,

$$\mu_\sigma^>(-0) - \mu_\sigma^<(+0) = R_j^\sigma j_\sigma(0) \quad (5.15)$$

where $R_j^\sigma = (h/Ne^2)(R_\sigma/T_\sigma)$ is the interface resistance of spin channel σ , and N is the number of modes within the layer per unit cross-section area [30, 136, 137]. By combining Eqs.(5.13) through (5.15), we immediately find

$$\mu_\sigma^>(-0) - \mu_\sigma^<(-0) = \mu_\sigma^>(+0) - \mu_\sigma^<(+0) = j_\sigma \frac{h(1 - T_\sigma)}{e^2 N}. \quad (5.16)$$

From the definition $\mu_b = (\mu_\uparrow^> - \mu_\downarrow^>) - (\mu_\uparrow^< - \mu_\downarrow^<)$, we have

$$\mu_b(+0) = \mu_b(-0) = j_{eff} \left(\frac{h}{e^2 N} \right), \quad (5.17)$$

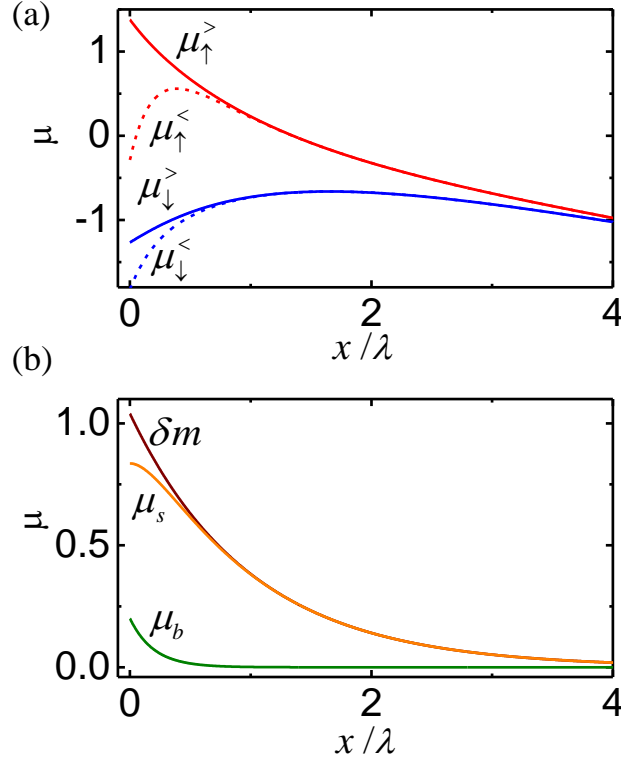


FIGURE 5.3. Spin injection through a tunnel barrier ($T_{\sigma} \ll 1$) into a diffusive NM layer, $l_0/\lambda = 0.2$, the polarization of the barrier resistance is $p_J = 0.5$. We plot CPs and spin accumulation in unit of $\rho j_e p_J \lambda$. (a) The directional and spin dependence of chemical potentials in the NM layer for left-going, right-going, spin up and spin down electrons. (b) the spin-dependent CP μ_s and its ballistic part μ_b , as well as the spin accumulation δm derived from CPs shown in top panel.

where we have defined the effective spin polarization $p_{eff} \equiv [(1 - T_{\uparrow})j_{\uparrow} - (1 - T_{\downarrow})j_{\downarrow}]/(j_{\uparrow} + j_{\downarrow})$.

The above boundary conditions result in three interesting consequences: 1) the ballistic CP is continuous across the junction which is in direct contrast with the diffusive CP which has a jump if there is interface roughness scattering or if the interface is treated as a diffusive resistor, 2) the ballistic CP is zero if $T_{\sigma} = 1$, i.e., if there is no tunnel barrier; this is evident since the entire bilayer is diffusive, and 3) if T_{σ} is small, the ballistic CP is always non-zero, indicating the fundamental difference between tunneling and diffusive scattering.

These boundary conditions together with the continuity of current and the spin

ballistic-diffusion equations, Eqs. (5.9-5.12), completely determine the position dependence of the CP, spin accumulation, and spin current. To gain further insight on the roles of ballistic CP, we present the detailed solution for a simple case where the magnetization of the FM layer is parallel to $\hat{\mathbf{e}}_x$ such that the precession terms (the terms with cross products) in Eqs. (5.9-5.12) vanish and $\boldsymbol{\mu}_s = \mu_s \hat{\mathbf{e}}_x$ and $\boldsymbol{\mu}_b = \mu_b \hat{\mathbf{e}}_x$,

$$\frac{d^2 \mu_b}{dx^2} = \frac{\mu_b}{l_{eff}^2}, \quad (5.18)$$

and

$$\frac{d^2 \mu_s}{dx^2} = \frac{\mu_s}{\lambda^2} + \frac{1}{2l_0} \frac{d\mu_b}{dx}. \quad (5.19)$$

The solutions are

$$\begin{aligned} \mu_b &= A \exp\left(-\frac{x}{l_{eff}}\right) \\ \mu_s &= -\frac{l_0}{2l_{eff}} A \exp\left(-\frac{x}{l_{eff}}\right) + A' \exp\left(-\frac{x}{\lambda}\right), \end{aligned} \quad (5.20)$$

where A and A' are integration constants determined by the boundary conditions. The general expressions for spin accumulation, spin current, and CPs for arbitrary parameters are given in the Appendix B.2. Here, we illustrate some limiting cases. In Fig. 5.3, we show four CPs (spin up and down with the momentum right and left-going) as well as μ_s , μ_b and δm at $x > 0$ where we have chosen a small ratio of the mean free path to the spin diffusion length, $l_0/\lambda = 0.2$; this is the case valid for the conventional spin-diffusion equation. The left-going and right-going CP merges to a single value after $x = l_0$, but a spin-split CP exists up to λ . Equivalently, μ_b approaches zero for $x > l_0$ and μ_s survives between l_0 and λ . For $l_0 < x < \lambda$, δm arises purely from μ_s . Thus, we conclude that the conventional spin-diffusion equation, describes the transport well in this limit, even though the ballistic transmission through the tunnel barrier is not a diffusive process.

Next, we consider the case, $l_0 > \lambda$. Within the conventional spin diffusion theory, the SA in the non-magnetic layer is $\delta m_0 = p_J j_e \rho \lambda \exp(-x/\lambda)$, where p_J is the spin polarization at the interface, j_e is the electric current density and ρ is the resistivity [8,9]. In Fig. 5.4(a) we show four CPs and the corresponding μ_s , μ_b ; in Fig. 5.4(b) we show the SA. On comparison with the conventional result for δm_0 one immediately sees that the SA is greatly enhanced.

The enhancement of the SA originates from the existence of the ballistic CP, i.e., the second term of Eq. (5.12). By recalling that $\boldsymbol{\mu}_b$ characterizes the difference in

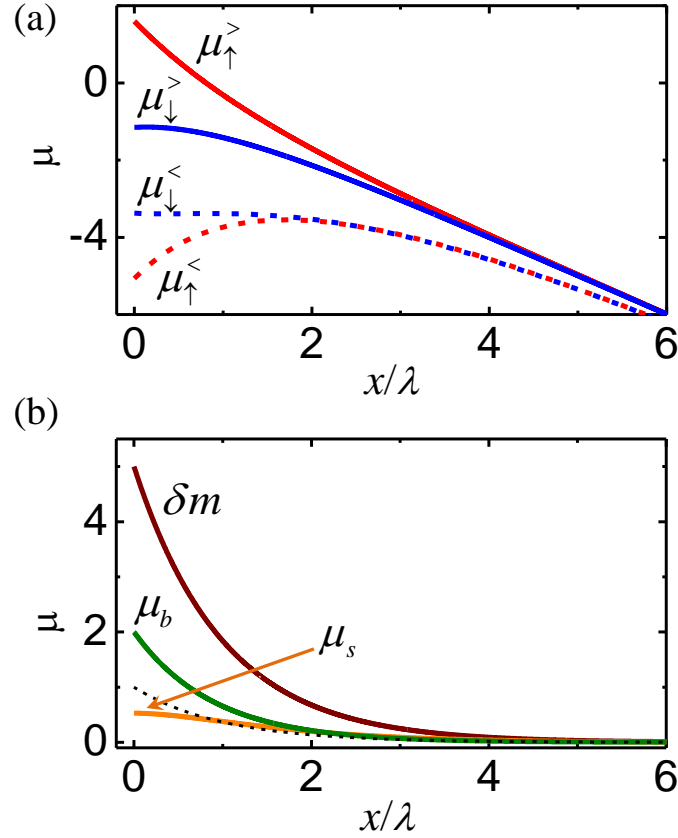


FIGURE 5.4. Spin injection through a tunnel barrier into a weak scattering NM layer where we choose $l_0/\lambda = 2$ and $p_J = 0.5$. All CPs and spin accumulation are plotted in unit of $\rho j_e p_J \lambda$. (a) The directional and spin dependence of chemical potentials in the NM layer for left-going, right-going, spin up and spin down electrons. (b) the spin-dependent CP μ_s and its ballistic part μ_b , as well as the spin accumulation δm . The dotted line shows $\delta m_0 = \rho j_e p_J \lambda e^{-x/\lambda}$.

the number of electron spins moving to the left and right, we may loosely consider μ_b as a source of spin current. The divergence of the spin current generates a spin accumulation, therefore $-l_0 d\mu_b/dx \propto (l_0/l_{eff})\mu_b$ is the ballistic contribution to SA. More quantitatively, when we carry out the detailed algebra in the limit of a large tunnel resistance (see the Appendix B.2) we find,

$$\delta m = \left(1 + \frac{l_0^2}{\lambda^2}\right) j_e p_J \rho \lambda \exp(-x/\lambda). \quad (5.21)$$

Thus the enhancement factor of the SA, which is defined as the ratio of SA to the

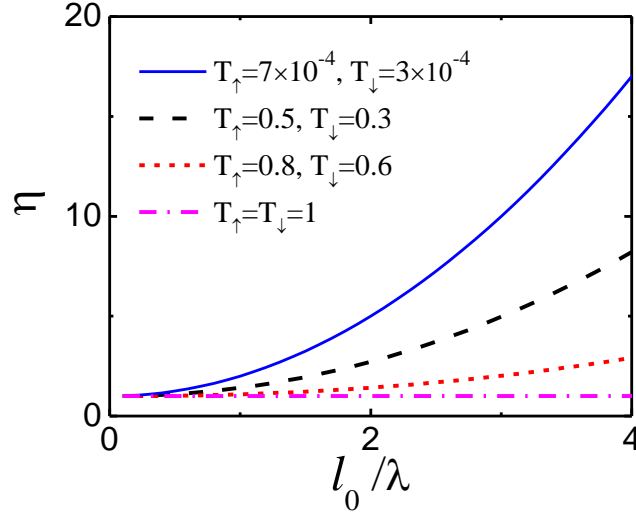


FIGURE 5.5. The enhancement factor of spin accumulation as a function of the ratio of the mean free path and spin dephasing length for various transmission coefficients. The other parameters are, $\rho_F \lambda_F = 5$, $\rho_{F\sigma} l_{F\sigma} = 2$, $p_F = 0.5$, $\rho l_0 = 1$, $(h/e^2 N) = 2$, where $\rho_{F\sigma}$ ($l_{F\sigma}$) is the resistivity (mean free path) in FM layer for spin channel σ , $p_F = (\rho_{F\downarrow} - \rho_{F\uparrow}) / (\rho_{F\downarrow} + \rho_{F\uparrow})$, λ_F is the spin diffusion length of the FM layer and $\rho_F = \rho_{F\uparrow} \rho_{F\downarrow} / (\rho_{F\downarrow} + \rho_{F\uparrow})$.

conventional one, $\eta \equiv \delta m / \delta m_0$, in the limiting case $T_\sigma \ll 1$ is

$$\eta = 1 + l_0^2 / \lambda^2. \quad (5.22)$$

In Fig. 5.5, we show the SA enhancement factor as a function of the ratio l_0/λ for various tunnel transmission coefficients. When $l_0/\lambda \ll 1$, there is no enhancement, $\eta = 1$ for all transmission coefficients; as l_0/λ increases, the enhancement depends on the transmission coefficient. As T increases η decreases. Thus we conclude that the large enhancement must simultaneously satisfy two conditions: a spin-dependent barrier resistance that dominates over the bulk resistance, and a long mean free path compared to the spin dephasing length. Our results are consistent with experimental results [27]: η could be as large as 6 when the temperature is lowered such that the mean free path exceeds the spin dephasing length in the 2d electron gas at a (Al, Ga)As/GaAs interface when a spin current is injected through a tunnel barrier.

Finally, we wish to emphasize a few points on the role of the ratio of the mean free path relative to the spin dephasing length. First, in quantum wells, the D'yakonov-

Perel' relaxation [138, 139] has been well studied theoretically and experimentally in both strong and weak scattering limits [140–143]. One might ask whether the ballistic components have to be considered in the weak scattering limit as well. The answer relies on the initial or boundary conditions; if the SA is optically injected over a large spatial region, which is the case for most experiments on semiconductor, the ballistic chemical potentials remain zero even if $l_0/\lambda > 1$ because there is no mechanism to introduce a non-zero μ_b . Second, the spin-orbit coupling has various forms due to different growth directions of quantum wells [144, 145] or the coexistence of Rashba and Dresselhaus SOC [143, 144], therefore the resulting spin ballistic-diffusions, Eqs. (5.9) and (5.10), would be modified. In these cases, the solutions becomes rather tedious and complex. However, the physics on the spin accumulation enhancement from the ballistic transport remains the same.

APPENDIX A

CONDUCTIVITY IN LAYERED THIN FILMS

In this Appendix, we show the detailed calculations of the position dependent conductivity which are omitted from the main text. This supplemental material is organized as follows: We introduce our model Hamiltonian for a bilayer system with interface states in Sec. A.1. The Green's functions in thin films and multilayers are derived in Sec. A.2. In Sec. A.3, We show that our calculated conductivity is identical with semiclassical results in limiting case by comparing the results of a single thin film. We show example calculations where interface states is in presence in Sec. A.4.

A.1 Model Hamiltonian

A simple model Hamiltonian of the bilayer is chosen,

$$H = H_0 + H' \quad (\text{A.1})$$

where $H_0 = H_L + H_R + H_{int}$ is the sum of the Hamiltonians for the left layer, the right layer, and the interface monolayer, H' describes the coupling between the interfacial monolayer and the left/right layers. More explicitly,

$$H_L = -t \sum_{\langle i,j \rangle \in L, \mathbf{k}_{\parallel}} \left(c_{i\mathbf{k}_{\parallel}}^+ c_{j\mathbf{k}_{\parallel}} + h.c. \right) + \sum_{i \in L} c_{i\mathbf{k}_{\parallel}}^+ \varepsilon_{\mathbf{k}_{\parallel}}^L c_{i\mathbf{k}_{\parallel}} \quad (\text{A.2})$$

for the left layer and similarly for the right layer (replacing L by R in the above equation), where t is the hopping strength between the two nearest neighbors, $c_{i\mathbf{k}_{\parallel}}^+ = \left(c_{i\mathbf{k}_{\parallel}\uparrow}^+, c_{i\mathbf{k}_{\parallel}\downarrow}^+ \right)$ is conduction electron creation operator at site i , expressed in the spinor form. Note that we have written the Hamiltonian in the mixed space-momentum representation: the translation invariance in the plane of the layer allows us to use the in-plane momentum \mathbf{k}_{\parallel} as a quantum number while we retain the layered index i to represent the growth direction.

The Hamiltonian of the interface is

$$H_{int} = \sum_{\mathbf{k}_{\parallel}} c_{0\mathbf{k}_{\parallel}}^+ \varepsilon_{0\mathbf{k}_{\parallel}} c_{0\mathbf{k}_{\parallel}} \quad (\text{A.3})$$

where the sub-index “0” indicates the interface layer, and $\varepsilon_{0\mathbf{k}_\parallel}$ is the interface energy dispersion which could be spin-dependent.

The interaction between the interface and left/right layers is modeled by

$$H' = -t_L \sum_{\mathbf{k}_\parallel} c_{0\mathbf{k}_\parallel}^+ c_{-1\mathbf{k}_\parallel} - t_R \sum_{\mathbf{k}_\parallel} c_{0\mathbf{k}_\parallel}^+ c_{1\mathbf{k}_\parallel} + h.c. \quad (\text{A.4})$$

where $t_{L/R}$ is the hopping parameter between the interface and the left/right layer. Note that the left (right) layer is indexed with a negative (positive) integer i representing the atomic position at $z = ia$; thus $i = -1$ and $i = 1$ are two atomic layers in contact with the interface layer $i = 0$.

A.2 Tight binding Green’s function in thin film

In this appendix, we briefly outlined how the Green’s functions used in the main text are calculated. We start from an infinite lattice of which the Hamiltonian is

$$H_{NM} = -t \sum_{\langle i,j \rangle, \mathbf{k}_\parallel} \left(c_{i\mathbf{k}_\parallel}^+ c_{j\mathbf{k}_\parallel} + h.c. \right) + \varepsilon_{\mathbf{k}_\parallel} \sum_{i \in L} c_{i\mathbf{k}_\parallel}^+ c_{i\mathbf{k}_\parallel}. \quad (\text{A.5})$$

The energy dispersion in such a lattice is

$$E = -2t \cos ka + \varepsilon_{\mathbf{k}_\parallel} \quad (\text{A.6})$$

The Green’s function of which can be found in many quantum mechanics textbooks,

$$g^\infty(i, j; E, \mathbf{k}_\parallel) = \frac{\pm e^{\pm ika|i-j|}}{2it \sin ka} \quad (\text{A.7})$$

where k is determined from

$$-2t \cos ka = E - \varepsilon_{\mathbf{k}_\parallel} \pm i\Delta_{im} \quad (\text{A.8})$$

and Δ_{im} is the imaginary part of the self-energy. The Green’s function in an semi-infinite lattice and thin film can be calculated via the Dyson equation.

We first consider a potential

$$V = t \left(c_{n_0, \mathbf{k}_\parallel}^+ c_{n_0-1, \mathbf{k}_\parallel} + h.c. \right) \quad (\text{A.9})$$

which breaks the hopping between site $i = n_0$ and $n_0 - 1$. The infinite lattice breaks into two separated semi-infinite lattice. The Green’s function a semi-infinite lattice

can be calculated using following Dyson equation, for $i, j \geq n_0$,

$$\begin{aligned} g^{semi}(i, j; E, \mathbf{k}_{\parallel}) &= g^{\infty}(i, j; E, \mathbf{k}_{\parallel}) \\ &+ t g^{\infty}(i, n_0 - 1; E, \mathbf{k}_{\parallel}) g^{semi}(n_0, j; E, \mathbf{k}_{\parallel}) \\ &+ t g^{\infty}(i, n_0; E, \mathbf{k}_{\parallel}) g^{semi}(n_0 - 1, j; E, \mathbf{k}_{\parallel}) \end{aligned} \quad (\text{A.10})$$

where the last term vanish since $g^{semi}(n_0 - 1, j; E, \mathbf{k}_{\parallel}) = 0$, i.e., the site $n_0 - 1$ is disconnected from the right semi-infinite lattice. From above equation, we can solve the $g^{semi}(i, j; E, \mathbf{k}_{\parallel})$ after some straight forward calculation. Here, I list only the results for a semi-infinite lattice $z \geq n_0$,

$$g^{semi}(i, j \geq n_0; E, \mathbf{k}_{\parallel}) = \frac{\pm 1}{2it \sin ka} [e^{\pm ika|i-j|} - e^{ika(|i-n_0|+|n_0-j|)}] \quad (\text{A.11})$$

If we continue breaking the hopping between site $i = n_1$ and $n_1 + 1$, we can get the Green's function in a thin film, $n_0 \leq i \leq j \leq n_1$, which is

$$g^{film}(i, j; E, \mathbf{k}_{\parallel}) = \frac{1}{t \sin ka} \frac{\sin ka (i - n_0 + 1) \sin ka (n_1 - j + 1)}{\sin ka (d + 1)} \quad (\text{A.12})$$

where $d = n_1 - n_0 + 1$ is the number of atomic layers. For a special case, the tight binding Green's function at the interface of a thin film can be written by take $i = j = n_0/1$, we get

$$g^{film}(n_0, n_0; E, \mathbf{k}_{\parallel}) = g^{film}(n_1, n_1; E, \mathbf{k}_{\parallel}) = -\frac{\sin kad}{t \sin ka (d + 1)} \quad (\text{A.13})$$

For a monolayer, where $d = 1$, the above Green's function reduces to

$$g^{int}(n_0, n_0; E, \mathbf{k}_{\parallel}) = -\frac{1}{2t \cos ka} = \frac{1}{E - \varepsilon_{\mathbf{k}_{\parallel}}^{int} \pm i\Delta_{im}} \quad (\text{A.14})$$

where we used the results from Eq. (A.8).

A.3 Compare with Semiclassical Results

A.3.1 Comparison with Drude Model

The last equation from above section shows the Green's function of an atomic monolayer. Thus, the conductivity is obtained as,

$$\sigma(n_0) = \frac{\hbar e^2}{\pi a^3} \sum_{\mathbf{k}_{\parallel}} v_{\mathbf{k}_{\parallel}}^2 [A(n_0, n_0; E_F, \mathbf{k}_{\parallel})]^2. \quad (\text{A.15})$$

For the interfacial monolayer with a spin-independent quadratic band, $\varepsilon_{\mathbf{k}_{\parallel}}^{int} = tk_{\parallel}^2 a^2$, the above conductivity $\sigma(n_0) = ek_F v_F / (4\hbar\pi a \Delta_{im})$ is the Drude conductivity of the two-dimensional free-electron gas.

In the second limiting case, we consider an infinite lattice. The Green's function between any two sites is,

$$g_{a/r}^0(i, j; E_F, \mathbf{k}_{\parallel}) = \frac{\pm 1}{2it \sin ka} e^{\pm ika|i-j|}. \quad (\text{A.16})$$

where k is the solution of $-2t \cos ka = E_F - tk^2 a^2 \pm \Delta_{im}$. The conductivity can be calculated using the following equation,

$$\sigma(i) = \frac{\hbar e^2}{\pi a^3} \sum_{\mathbf{k}_{\parallel}, j} v_{\mathbf{k}_{\parallel}}^2 [A(i, j; E_F, \mathbf{k}_{\parallel})]^2 \approx \frac{\hbar e^2}{\pi a^3} \sum_{\mathbf{k}_{\parallel}, j} v_{\mathbf{k}_{\parallel}}^2 g_a(j, i; E_F, \mathbf{k}_{\parallel}) g_r(i, j; E_F, \mathbf{k}_{\parallel}). \quad (\text{A.17})$$

By inserting above Green's function and taking the small wave vector approximation, $\sin ka \sim ka$, one finds

$$\sigma(i) = \frac{ek_F^2 v_F}{6\hbar\pi^2 \Delta_{im}} \quad (\text{A.18})$$

which is exactly Drude conductivity of three dimensional electron gas.

A.3.2 Comparison with results of Boltzmann Equation

We now consider a single thin film. Eq. (A.12) shows two-site Green's function when assuming the interface is perfectly reflective which corresponds to the $p = 1$ case in the Fuchs model. The calculated conductivity uniform across the thin film and the magnitude is same as that in a large bulk, which is same as the semiclassical results. While the Green's function also indicates oscillation near the interface with the range of $1/k_F$ which is neglected in the semiclassical approach.

Another limiting case can be easily compared is that when the outer interface is completely rough so that all momentum information is lost when electron is reflected by the interface. The Green's function in such a case is the same as the one in an infinite lattice,

$$g_{a/r}(i, j; E_F, \mathbf{k}_{\parallel}) = \frac{\pm 1}{2it \sin ka} e^{\pm ika|i-j|}. \quad (\text{A.19})$$

One can easily calculate the conductivity at site i and also the average conductivity across the film. Here it is,

$$\sigma(i) = \frac{\hbar e^2}{\pi a^3} \sum_{\mathbf{k}_{\parallel}, j} v_{\mathbf{k}_{\parallel}}^2 [A(i, j; E_F, \mathbf{k}_{\parallel})]^2 \approx \frac{\hbar e^2}{\pi a^3} \sum_{\mathbf{k}_{\parallel}, j} v_{\mathbf{k}_{\parallel}}^2 g_a(j, i; E_F, \mathbf{k}_{\parallel}) g_r(i, j; E_F, \mathbf{k}_{\parallel}). \quad (\text{A.20})$$

Now we use the free electron dispersion to compare with the Fuchs' results and we have $k = \sqrt{k_F^2 - k_{\parallel}^2} + \frac{k_F \Delta_{im}}{2E_F \sqrt{1 - k_{\parallel}^2/k_F^2}}$. Above conductivity can be written as

$$\sigma(x) = \frac{e^2}{2\pi^2 \hbar} \int_0^d dx' \int dk_{\parallel} \frac{k_{\parallel}^3}{k_F^2 \cos \theta^2} \exp\left(\frac{-|x - x'|}{|\cos \theta| \lambda}\right) \quad (\text{A.21})$$

where we have introduced $\sqrt{1 - k_{\parallel}^2/k_F^2} = \cos \theta$ and $\lambda = \frac{E_F}{\Delta_{im} k_F}$ is the mean free path. One can simplify above results

$$\sigma(x) = \frac{e^2 k_F}{2\pi^2 \hbar} \int_0^{\pi/2} d\theta \sin^3 \theta \left[2 - \exp\left(\frac{-|d - x|}{\cos \theta \lambda}\right) - \exp\left(\frac{-|x|}{\cos \theta \lambda}\right) \right] \quad (\text{A.22})$$

The spatial averaged conductivity is

$$\sigma = \frac{1}{d} \int dx \sigma(x) = \frac{e^2 k_F}{\pi^2 \hbar} \int_0^{\pi/2} d\theta \sin^3 \theta \left[1 - \frac{\lambda \cos \theta}{d} (1 - e^{-d/\cos \theta \lambda}) \right] \quad (\text{A.23})$$

which is the same as Fuchs' results.

A.4 spatial dependence of conductivity in the presence of interface states

The interface states depend on many factors. Due to spatial broken symmetry at the interface, interface states are usually no longer an extended state in the direction of the growth. For example, a Rashba interaction which requires a spatial inversion symmetry-breaking exists at the interface, but not in the bulk, and thus the helix spin states are limited to the interface. The interface states could also be affected by interface disorders. In the following, we describe the current density distribution in the bilayer for several interface states.

We next discuss the current density with interface states that take a variety of forms. In semiconductor heterostructure, the band mismatch of two layers could generate an interface band structure hosting a 2D-electron gas and the electron conduction is strictly limited at the interface region. In the presence of large spin-orbit coupling known as the Rashba interaction, a spin helix state exists at the transition metal interface, but not in the bulk. Let's first consider generic two-dimensional states formed at the interface and the coupling between the 2d states and nearest neighbor atoms is modeled by Eq. (A.17). The conductivity at the interface can be written as

$$\sigma(0) = \sigma(0, 0) + \sum_j \sigma(0, j) \quad (\text{A.24})$$

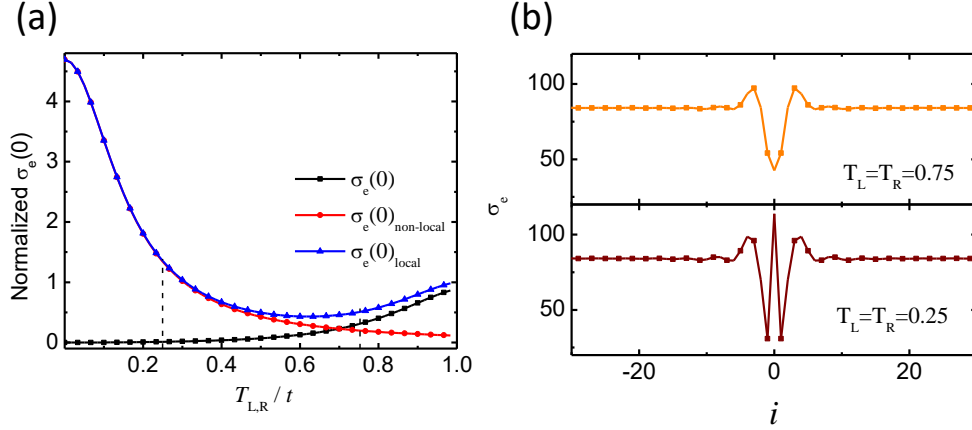


FIGURE A.1. (a). The local and nonlocal contributions to the interface conductance as a function of the coupling between 2d and 3d states. In our calculation, we took $k_F a = 1$. (b). The current distribution throughout the bilayer for fixed hopping parameters.

which contains both the local and non-local contributions.

In Eq. (A.14), we show the Green's function at the isolated interface. With finite interlayer hopping, one can show that the Green's function has a similar form,

$$G_{a/r}^0(0, 0; E_F, \mathbf{k}_{\parallel}) = \frac{1}{E_F - \varepsilon_{0\mathbf{k}_{\parallel}} \pm i(\Delta_{im} + \Delta_T)} \quad (\text{A.25})$$

where

$$\Delta_T \equiv t_L^2 \text{Im}[G^0(-1, -1; E_F, \mathbf{k}_{\parallel})] + t_R^2 \text{Im}[G^0(1, 1; E_F, \mathbf{k}_{\parallel})] \quad (\text{A.26})$$

is the self-energy introduced by hopping. So that when considering the interface conductivity, the hopping has two roles: on one hand it increases the self-energy at the interface and increases the non-local conductivity.

When the hopping parameters between 2d and 3d states are turned off, the interface and bulk current densities are independent. In terms of the Green's function, we have $G_{R/A}(0, i) = 0$. In Fig. A.1(a), we show the interface conductance $\sigma(0)$ when $t_L = t_R$ turns on. The contribution from the $\sigma_L = \sigma(0, 0)$ decreases as the hopping increases, due to the enhanced relaxation from 2d states to 3d states, Eqs (A.25, A.26). On the contrary, the non-local contribution $\sigma_{NL}(0) = \sum_{j \neq 0} \sigma(0, j)$ begins to show up. Interestingly, the total interface conductance $\sigma(0) = \sigma_L(0) + \sigma_{NL}(0)$ has a local minimum at around $t_L = t_R \simeq 0.6t$. If we take a fixed value of $t_L = t_R$, the position

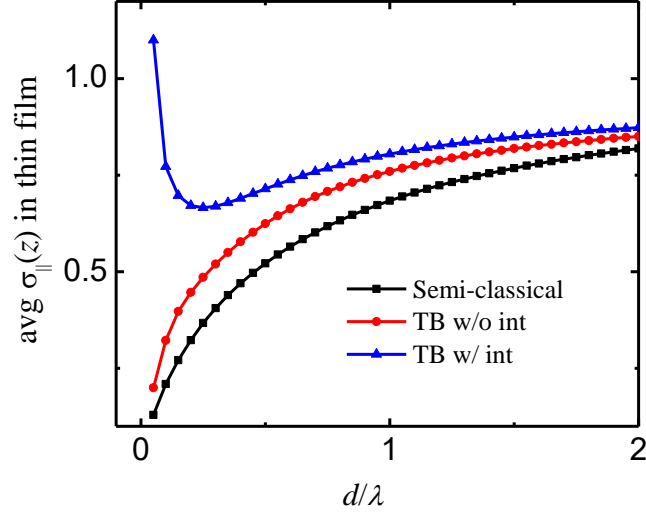


FIGURE A.2. The conductivity of a thin film with and without surface states as a function of layer thickness, λ is the electron mean free path in the bulk. When there is no surface states, the semiclassical continuous model (black square line) and our tight-binding approach (red circle line) are approximately same. In the presence of the surface state (c), the conductivity increases at the small thickness. The parameters used here: Rashba split is $0.2E_F$, mean free path 5 nm , the interfacial hopping $t_L/t = 0.4$.

dependent conductance are shown in Fig. A.1(b). We notice that the current density shows a non-monotonic variation, which results from the opposite dependence of the local and nonlocal contribution on the interlayer hopping. For small interlayer hopping, the conductivity at the interface is dominated by the local contribution, increasing $t_{L/R}$ increases the self-energy in Eq. (A.26) which in turn reduces the conductivity. For larger hopping, $t_{L/R} > 0.7t$, the self-energy in Eq. (A.26) is so large that the conductivity $\sigma(0)$ mainly comes from the non-local contribution. As $t_{L/R}$ keeps rising up, the Green's function $G(0, i)$ increases and so does the conductivity.

For another example, we consider the thickness dependence of the conductivity when interface states are at present. We model the interface dispersion by,

$$\varepsilon_{0\mathbf{k}} = \varepsilon_0 + \frac{\hbar^2 k^2}{2m} + \hbar\alpha_F (\mathbf{k} \times \boldsymbol{\sigma}) \cdot \hat{z}, \quad (\text{A.27})$$

we find the current has a higher density at the interface than that in the bulk. The average conductivity for a thin film is shown in Fig. A.2 for the plausible parameters indicated.

APPENDIX B

DERIVATION AND CALCULATION FOR SPIN TRANSPORT EQUATION IN BALLISTIC REGIME

B.1 Derivation of the ballistic spin transport equation

In this appendix, we show the derivation of Eqs. (5.9-5.12) starting from the Boltzmann equation, Eq. (5.3). We use the Dresselhaus Hamiltonian to model the SOC. Thus, $\hat{v}_x = v_x \hat{I} + \alpha \hat{\sigma}_x$, then Eq. (5.3) reads

$$v_x \frac{\partial \hat{F}}{\partial x} + \frac{1}{2} \alpha \left\{ \hat{\sigma}_x, \frac{\partial \hat{F}}{\partial x} \right\} + \frac{eE}{m} \frac{\partial \hat{F}}{\partial v_x} - \frac{1}{i\hbar} [\hat{H}_{SO}, \hat{F}] = -\frac{\hat{F} - \bar{F}}{\tau_m} - \frac{\bar{F} - (1/2)\hat{I}\text{Tr}(\bar{F})}{\tau_{sf}} \quad (\text{B.1})$$

Substitute the distribution function with equilibrium and non-equilibrium parts defined in Eq. (5.4), we get the equations for the spin and charge parts distribution functions,

$$v_x \frac{\partial f_0}{\partial x} + eE v_x + \frac{\alpha}{\hbar} \frac{\partial (\mathbf{f}_1 \cdot \hat{e}_x)}{\partial x} = -\frac{f_0 - \bar{f}_0}{\tau_m} \quad (\text{B.2})$$

$$v_x \frac{\partial \mathbf{f}_1}{\partial x} - \boldsymbol{\Omega}_{\mathbf{k}} \times \mathbf{f}_1 + \frac{\alpha}{\hbar} \frac{\partial f_0}{\partial x} \hat{e}_x = -\frac{\mathbf{f}_1 - \bar{\mathbf{f}}_1}{\tau_m} - \frac{\bar{\mathbf{f}}_1}{\tau_{sf}}. \quad (\text{B.3})$$

where the third terms on the left hand side are the spin charge coupling (SCC). Same equations have been derived in Ref. [134] except that we have taken the distribution function to be uniform along \hat{y} direction. We then neglect the spin flip term and assume the spin relaxation is dominated by the spin-orbit coupling.

Insert the left and right split CPs defined in Eqs. (5.7, 5.8), we start to derive our novel spin transport equations in the presence SOC. We only show the detailed derivation for the spin part, Eq. (B.3). For the charge part, the derivation is similar. With \mathbf{f}_1 substituted with CPs, Eq. (B.3) now reads,

$$\begin{aligned} & v_x \frac{\partial}{\partial x} [\boldsymbol{\mu}_1^{\gt} \theta(k_x) + \boldsymbol{\mu}_1^{\lt} \theta(-k_x) - \mathbf{g}_1(k_x, x)] - \boldsymbol{\Omega}_{\mathbf{k}} \times [\boldsymbol{\mu}_1^{\gt} \theta(k_x) + \boldsymbol{\mu}_1^{\lt} \theta(-k_x) - \mathbf{g}_1(k_x, x)] \\ & + \frac{\alpha}{\hbar} \frac{\partial}{\partial x} [\mu_0^{\gt}(x) \theta(k_x) + \mu_0^{\lt}(x) \theta(-k_x) - g_0(k_x, x)] \\ = & -\frac{\boldsymbol{\mu}_1^{\gt} \theta(k_x) + \boldsymbol{\mu}_1^{\lt} \theta(-k_x) - \mathbf{g}_1(k_x, x)}{\tau_m} + \frac{\boldsymbol{\mu}_1^{\gt} + \boldsymbol{\mu}_1^{\lt} - 2\bar{\mathbf{g}}_1}{2\tau_m} \end{aligned} \quad (\text{B.4})$$

where $\Omega_{\mathbf{k}} = \alpha/2(k_x, -k_y, 0)$.

Following the conventional protocol to establish the corresponding macroscopic equation from the Boltzmann equation, one needs to relate $\mathbf{g}_1(k_x, x)$ to $\boldsymbol{\mu}_1^>$ and $\boldsymbol{\mu}_1^<$. The common choice is

$$\begin{aligned} g_0(k_x, x) &= v_x \tau_m \frac{\partial}{\partial x} [\mu_0^> \theta(k_x) + \mu_0^< \theta(-k_x)] \\ \mathbf{g}_1(k_x, x) &= v_x \tau_m \frac{\partial}{\partial x} [\boldsymbol{\mu}_1^> \theta(k_x) + \boldsymbol{\mu}_1^< \theta(-k_x)] - \tau_m \Omega_{\mathbf{k}} \times [\boldsymbol{\mu}_1^> \theta(k_x) + \boldsymbol{\mu}_1^< \theta(-k_x)]. \end{aligned} \quad (\text{B.5})$$

The average over Fermi Circle is

$$\begin{aligned} \bar{\mathbf{g}}_1 &\approx \frac{l_0}{2} \left[\frac{\partial}{\partial x} (\boldsymbol{\mu}_1^> - \boldsymbol{\mu}_1^<) - \frac{1}{\lambda} \hat{e}_x \times (\boldsymbol{\mu}_1^> - \boldsymbol{\mu}_1^<) \right] \\ &= \frac{l_0}{2} \left(\frac{\partial}{\partial x} \boldsymbol{\mu}_b - \frac{1}{\lambda} \hat{e}_x \times \boldsymbol{\mu}_b \right) \end{aligned} \quad (\text{B.6})$$

where $l_0 = \sqrt{v_x^2} \tau_m = v_F \tau_m / \sqrt{2}$ is the mean free path, and we have approximated $|\bar{v}_x| \approx \sqrt{v_x^2} = v_F / \sqrt{2}$ to simplify the notation without changing essential results obtained below. We have also introduced the definition of the ballistic spin CP, $\boldsymbol{\mu}_b \equiv \boldsymbol{\mu}_1^> - \boldsymbol{\mu}_1^<$, as explained in the main text.

Inserting the above expression of $\mathbf{g}_1(k_x, x)$ and $\bar{\mathbf{g}}_1$ into Eq. (B4) and averaging over left ($k_x < 0$) and right ($k_x > 0$) half Fermi Circles separately, we get two equations,

$$\frac{\partial^2 \mu_1^>}{\partial x^2} - \frac{2}{\lambda} \hat{e}_x \times \frac{\partial \mu_1^>}{\partial x} - \Delta \left[\frac{1}{l_0} \frac{\partial \mu_0^>}{\partial x} - \frac{\partial^2 \mu_0^>}{\partial x^2} \right] \hat{e}_x = \frac{\mu_1^>}{l_0^2} - \frac{1}{l_0^2} \left[\mu_s - \frac{l_0}{2} \left(\frac{\partial}{\partial x} \boldsymbol{\mu}_b - \frac{1}{\lambda} \hat{e}_x \times \boldsymbol{\mu}_b \right) \right] + \Gamma \mu_1^> \quad (\text{B.7})$$

$$\frac{\partial^2 \mu_1^<}{\partial x^2} - \frac{2}{\lambda} \hat{e}_x \times \frac{\partial \mu_1^<}{\partial x} - \Delta \left[\frac{1}{l_0} \frac{\partial \mu_0^<}{\partial x} + \frac{\partial^2 \mu_0^<}{\partial x^2} \right] \hat{e}_x = \frac{\mu_1^<}{l_0^2} - \frac{1}{l_0^2} \left[\mu_s - \frac{l_0}{2} \left(\frac{\partial}{\partial x} \boldsymbol{\mu}_b - \frac{1}{\lambda} \hat{e}_x \times \boldsymbol{\mu}_b \right) \right] + \Gamma \mu_1^< \quad (\text{B.8})$$

where $\Delta = E_{SO}/E_F$ denotes the strength of SCC and Γ is a matrix which describes the anisotropic spin relaxation due to Dresselhaus spin-orbit coupling and

$$\Gamma = \begin{pmatrix} \lambda^{-2} & 0 & 0 \\ 0 & \lambda^{-2} & 0 \\ 0 & 0 & 2\lambda^{-2} \end{pmatrix}.$$

Linear combination of the above two equations leads to the following two differential equations,

$$\frac{\partial^2}{\partial x^2} \boldsymbol{\mu}_b - \frac{2}{\lambda} \hat{e}_x \times \frac{\partial}{\partial x} \boldsymbol{\mu}_b - \Delta \left[\frac{\partial}{l_0 \partial x} \mu_{cb} - 2 \frac{\partial^2}{\partial x^2} \mu_c \right] \hat{e}_x = \left(\frac{1}{l_0^2} + \Gamma \right) \boldsymbol{\mu}_b \quad (\text{B.9})$$

$$\frac{\partial^2}{\partial x^2} \mu_s - \frac{2}{\lambda} \hat{e}_x \times \frac{\partial}{\partial x} \mu_s - \Delta \left[\frac{\partial}{l_0 \partial x} \mu_c - \frac{1}{2} \frac{\partial^2}{\partial x^2} \mu_{cb} \right] \hat{e}_x = \frac{1}{2l_0} \left(\frac{\partial}{\partial x} \boldsymbol{\mu}_b - \frac{1}{\lambda} \hat{e}_x \times \boldsymbol{\mu}_b \right) + \Gamma \mu_s \quad (\text{B.10})$$

The above equations are equivalent to Eqs. (5.9) and (5.10) in the main text when the SCC is neglected ($\Delta = 0$). Similarly, one can get

$$\frac{\partial^2}{\partial x^2} \mu_{cb} - \Delta \left[\frac{\partial}{l_0 \partial x} \boldsymbol{\mu}_b \cdot \hat{e}_x - 2 \frac{\partial^2}{\partial x^2} \boldsymbol{\mu}_s \cdot \hat{e}_x \right] = \frac{\mu_{cb}}{l_0^2} \quad (\text{B.11})$$

$$\frac{\partial^2}{\partial x^2} \mu_c - \Delta \left[\frac{\partial}{l_0 \partial x} \boldsymbol{\mu}_s \cdot \hat{e}_x - \frac{1}{2} \frac{\partial^2}{\partial x^2} \boldsymbol{\mu}_b \cdot \hat{e}_x \right] = \frac{1}{2l_0} \frac{\partial}{\partial x} \mu_{cb} \quad (\text{B.12})$$

The spinor current density is defined as $\hat{j} = \frac{e}{2} \int \left\{ \hat{v}_x, \hat{F} \right\} d^2k$, where \hat{F} is the spinor distribution function. By separating the current density into the charge and spin and parts, $\hat{j} = j_e \hat{I} + \mathbf{j}_s \cdot \hat{\boldsymbol{\sigma}}$, and by utilizing \hat{F} defined in Eq. (5.10) and Eq. (B5), with $\hat{v}_x = \hbar k_x / m + \alpha \hat{\sigma}_x$, we obtain the expression for spin current \mathbf{j}_s ,

$$\mathbf{j}_s \rho = -\frac{\partial \mu_s}{\partial x} + \frac{\mu_b}{2l_0} + \frac{1}{\lambda} \hat{e}_x \times \boldsymbol{\mu}_s + \frac{\Delta}{l_0} \delta n \hat{e}_x \quad (\text{B.13})$$

Similarly for the charge current, j_e ,

$$j_e \rho = -\frac{\partial \mu_c}{\partial x} + \frac{\mu_{cb}}{2l_0} + \frac{\Delta}{l_0} \delta \mathbf{m} \cdot \hat{e}_x \quad (\text{B.14})$$

where ρ is the Drude conductivity for 2D electron gas. Similarly, we can derive the expression of the charge and spin accumulation by using the relation $\delta n \hat{I} + \delta \mathbf{m} \cdot \hat{\boldsymbol{\sigma}} = \int \hat{F} d^2k$, we find

$$\delta \mathbf{m} = \boldsymbol{\mu}_s - \frac{l_0}{2} \frac{\partial}{\partial x} \boldsymbol{\mu}_b + \frac{l_0}{2\lambda} \hat{e}_x \times \boldsymbol{\mu}_b \quad (\text{B.15})$$

$$\delta n = \mu_c - \frac{l_0}{2} \frac{\partial}{\partial x} \mu_{cb} \quad (\text{B.16})$$

Equations (B13) and (B15) are the spin-dependent Ohm's law used in the main text, Eqs. (5.11) and (5.12).

The effects of SCC on spin transport: In the main text, we discard the SCC in all equations, which is valid when $\Delta \ll 1$. When Δ cannot be neglected, the spin injection into the 2DEG with SOC can still be evaluated using above differential equations, Eqs. (B9-B12) and boundary conditions mentioned in the main text, Eqs. (5.13-5.15). We redo the calculation and keep up to the second order of Δ . We find the SCC reduces the spin relaxation length,

$$\frac{1}{\lambda'} = \frac{1}{\lambda} + \Delta^2 \left(\frac{1}{\lambda} + \frac{\lambda}{l_0^2} \right). \quad (\text{B.17})$$

where λ is the spin relaxation length defined in the main text which is merely determined by the spin-orbit coupling. When injecting spin into a 2DEG across a tunnel

barrier, the SCC modifies the spin accumulation enhancement in ballistic regime ($l_0 \gg \lambda$)

$$\delta m = [1 + (1 + 3\Delta^2)l_0^2/\lambda^2]\rho j_e p_J \lambda' e^{-x/\lambda'}. \quad (\text{B.18})$$

B.2 Detailed Calculation for spin injection into ballistic material

In the following, we first show the solution for a simple case where the polarization of the spin current is solely determined by the tunneling barrier between the FM and NM layer. We then solve the equation for general cases where the resistance of the layers are comparable to the tunnel resistance.

B.2.1 Resistance dominated by the tunnel barrier

If the resistance due to tunneling is much larger than the impurity scattering induced resistance in the layers, the injected current density and its spin polarization across the interface will be entirely determined by tunnel parameters, independent of the resistance in the layers, i.e.,

$$j_s(0) = j_e p_J \quad (\text{B.19})$$

where

$$p_J = \frac{R_J^\downarrow - R_J^\uparrow}{R_J^\downarrow + R_J^\uparrow} \quad (\text{B.20})$$

and $R_J^\sigma = (h/e^2)(R_\sigma/T_\sigma) \approx (h/e^2)(1/T_\sigma)$. From the boundary condition, Eq. (16),

$$\mu_b(+0) = j_e p_J R' \quad (\text{B.21})$$

where $R' = h/e^2 N$, we may directly obtain the solution of δm by using Eqs. (5.11-5.12) and Eq. (5.20),

$$\delta m = j_e p_J e^{-x/\lambda} \left[\frac{R' l_0 \lambda}{2 l_{eff}^2} + \rho \lambda \left(1 - \frac{R'}{2\rho l_0} \right) \right] \quad (\text{B.22})$$

The above expression can be simplified by relating the number of channels to the bulk resistivity and mean free path as we show below.

For an ideal conductor with N modes per unit cross-section area which connects two reservoirs, the current density flowing through the conductor carried by one spin channel is given by the Landauer formula,

$$j_e = \frac{e^2 N}{h} (\mu_L - \mu_R); \quad (\text{B.23})$$

where $\mu^{R/L}$ is the chemical potential of the left or right reservoir. In our case, the current density is given by

$$j_\sigma = \frac{1}{\rho_\sigma} \left[-\frac{\partial \mu_\sigma^>}{\partial x} - \frac{\partial \mu_\sigma^<}{\partial x} + \frac{1}{l_0} (\mu_\sigma^> - \mu_\sigma^<) \right] \quad (\text{B.24})$$

where the last term describes in the same way as contact potential from Eq. (B23). Thus, we can easily identify

$$\frac{1}{\rho_\sigma l_\sigma} = \frac{e^2 N}{h}. \quad (\text{B.25})$$

Insert this relation in to Eq. (B22) and take $\rho_\sigma = 2\rho$, $l_\sigma = l_0$ for the NM layer, we find

$$\delta m = \frac{l_0^2}{l_{eff}^2} j_e \rho \lambda p_J e^{-x/\lambda} \quad (\text{B.26})$$

which is the same as the Eq. (5.21) from the main text.

B.2.2 General solution and exact calculation

When the tunnel resistance is not much larger than that of the bulk, equivalently, when the transmission coefficient is not small (note that $T_\sigma = 1$ describes the transparent barrier or no barrier), one must solve the CPs for the entire bilayer, including the ferromagnetic layer. In this case, the spin polarization and spin accumulation depend on the detailed parameters of all layers in addition to the barrier transmission coefficients. We first write down the general solution of CPs according to Eqs. (B9-B12) (while the SCC terms are neglected) and then determine the coefficients by using the boundary conditions from main text.

In the NM layer ($x > 0$),

$$\mu_\uparrow^>(x) = \gamma_0 + \gamma_1 z + 2ce^{-x/\lambda} + ae^{-x/l_{eff}} \quad (\text{B.27})$$

$$\mu_\uparrow^<(x) = \gamma_0 + \gamma_1 z - ge^{-x/l_0} + 2ce^{-x/\lambda} + be^{-x/l_{eff}} \quad (\text{B.28})$$

$$\mu_\downarrow^>(x) = \gamma_0 + \gamma_1 z - 2ce^{-x/\lambda} - ae^{-x/l_{eff}} \quad (\text{B.29})$$

$$\mu_\downarrow^<(x) = \gamma_0 + \gamma_1 z - ge^{-x/l_0} - 2ce^{-x/\lambda} - be^{-x/l_{eff}} \quad (\text{B.30})$$

where $\mu_\sigma^> = \mu_0^> \pm \boldsymbol{\mu}_1^> \cdot \hat{e}_x$, $\sigma = \uparrow, \downarrow$. The Eq. (B10) also requires

$$a + b = -\frac{l_0}{l_{eff}}(a - b). \quad (\text{B.31})$$

For notation simplicity, we assume that the effective mean free path is same as the mean free path and the spin diffusion length is much longer in the FM layer ($x < 0$). The general solution in the FM layer is,

$$\mu_{\uparrow}^{\rightarrow}(x) = \gamma'_0 + \gamma'_1 z + \frac{\rho_F^{\uparrow}}{\rho_F} c' e^{x/\lambda_F} + a' e^{x/l_{F\uparrow}} \quad (\text{B.32})$$

$$\mu_{\uparrow}^{\leftarrow}(x) = \gamma'_0 + \gamma'_1 z + \frac{\rho_F^{\uparrow}}{\rho_F} c' e^{x/\lambda_F} \quad (\text{B.33})$$

$$\mu_{\downarrow}^{\rightarrow}(x) = \gamma'_0 + \gamma'_1 z - \frac{\rho_F^{\downarrow}}{\rho_F} c' e^{x/\lambda_F} + b' e^{x/l_{F\downarrow}} \quad (\text{B.34})$$

$$\mu_{\downarrow}^{\leftarrow}(x) = \gamma'_0 + \gamma'_1 z - \frac{\rho_F^{\downarrow}}{\rho_F} c' e^{x/\lambda_F}. \quad (\text{B.35})$$

where $\rho_F = \rho_{F\uparrow}\rho_{F\downarrow}/(\rho_{F\uparrow} + \rho_{F\downarrow})$, $\rho_{F\sigma} = \frac{\hbar}{e^2} \frac{\sqrt{2\pi}}{k_F l_{F\sigma}}$, and the polarization of the conductivity is

$$p_F = (\rho_F^{\downarrow} - \rho_F^{\uparrow}) / (\rho_F^{\downarrow} + \rho_F^{\uparrow}) = (l_{F\uparrow} - l_{F\downarrow}) / (l_{F\uparrow} + l_{F\downarrow}). \quad (\text{B.36})$$

There are many constants to be determined. γ_0 and γ'_0 are the voltages on two sides of the interface of which the difference addresses the voltage drop due to contact resistance. The total charge current density can be obtained from Eq. (A14)

$$-\gamma_1/\rho_F = -\gamma_1/\rho = j_e/2 \quad (\text{B.37})$$

where j_e is the injected charge current density and ρ_F, ρ are the resistivity of the FM and NM layer respectively. In Eq. (B37), we have assumed the cross-section area of the FM and NM layer to be the same for simplicity. With the boundary conditions from the main text, one can determine all the coefficients straightforward. The final results for the spin accumulation and spin polarization are

$$\delta \mathbf{m} = j_e \rho \lambda e^{-x/\lambda} \quad (\text{B.38})$$

$$p_{inj} = \frac{\frac{2p_F R_F}{1-p_F^2} + 2R' (T_{\downarrow}^{-1} - T_{\uparrow}^{-1}) - \frac{R_F}{1-p_F^2} (1 - \beta^2) T (p_F + p_J) + 2R' (1 - \beta^2) \frac{T_{\downarrow}^2 - T_{\uparrow}^2}{T_{\uparrow} T_{\downarrow}} + (T_{\uparrow} - T_{\downarrow}) R' (2 - \beta - 5\beta^2)}{\frac{2\beta^2 R_F}{1-p_F^2} + 2\beta^2 R' (T_{\downarrow}^{-1} + T_{\uparrow}^{-1}) + R_N [2 - (1 - \beta^2)(T)] + \beta(1 + 3\beta) R' T - 2\beta(1 + 5\beta) R'} \frac{\frac{2\beta^2 p_F R_F}{1-p_F^2} + 2\beta^2 R' (T_{\downarrow}^{-1} - T_{\uparrow}^{-1}) + [(1 - \beta^2) R_N - \beta(1 + 3\beta) R'] (T_{\uparrow} - T_{\downarrow})}{\frac{2\beta^2 R_F}{1-p_F^2} + 2\beta^2 R' (T_{\downarrow}^{-1} + T_{\uparrow}^{-1}) + R_N [2 - (1 - \beta^2)(T)] + \beta(1 + 3\beta) R' T - 2\beta(1 + 5\beta) R'} \quad (\text{B.39})$$

where $T = T_\uparrow + T_\downarrow$, $R_F \equiv \rho_F \lambda_F$, $R_N \equiv \rho \lambda$, $R' = 2\rho l_0$ and $\beta \equiv l_{eff}/l_0$. Below we show the results for two limiting cases.

Transparent Interface: By placing $T_\uparrow = T_\downarrow = 1$ into Eqs. (B38) and (B39), we have

$$p_{inj} = \frac{\frac{p_F R_F}{1-p_F^2}}{\frac{R_F}{1-p_F^2} + R_N} \quad (\text{B.40})$$

$$\delta m = j_e \rho \lambda p_J e^{-x/\lambda} \quad (\text{B.41})$$

Thus, there is no SC enhancement; this is because the transport is purely diffusive and the conventional spin diffusion theory applies.

Tunneling dominated Interface: For the resistance dominated by the tunneling interface, we take $T_\sigma \ll 1$, $R_J^\sigma \approx \frac{\hbar}{e^2 N} \frac{1}{T_\sigma}$, and $R_J^\downarrow, R_J^\uparrow \gg R_N, R', R_F$. Equations (B38) and (B21) are reduced to

$$p_{inj} = p_J = \frac{R_J^\downarrow - R_J^\uparrow}{R_J^\downarrow + R_J^\uparrow} \quad (\text{B.42})$$

$$\delta m = j_e \rho \lambda p_J e^{-x/\lambda} (1 + l_0^2/\lambda^2) \quad (\text{B.43})$$

where we used the definition of l_{eff} and $\beta^{-2} = l_0^2/l_{eff}^2 = 1 + l_0^2/\lambda^2$.

REFERENCES

- [1] G. Binasch, P. Grünberg, F. Saurenbach, and W. Zinn, Enhanced magnetoresistance in layered magnetic structures with antiferromagnetic interlayer exchange, *Phys. Rev. B* **39**, 4828(R) (1989).
- [2] M. N. Baibich, J. M. Broto, A. Fert, F. Nguyen Van Dau, F. Petroff, P. Etienne, G. Creuzet, A. Friederich, and J. Chazelas, Giant Magnetoresistance of (001)Fe/(001)Cr Magnetic Superlattices, *Phys. Rev. Lett.* **61**, 2472 (1988).
- [3] M.I.Dyakonov. and V.I.Perel, Current-induced spin orientation of electrons in semiconductors, *Phys. Lett. A* **35**, 459 (1971).
- [4] J. E. Hirsch, Spin Hall Effect, *Phys. Rev. Lett.* **83**, 1834 (2000).
- [5] A. Fert, Nobel Lecture: Origin, development, and future of spintronics, *Rev. Mod. Phys.* **80**, 1517 (2008).
- [6] J.C. Slonczewski, Current-driven excitation of magnetic multilayers, *J. Magn. Magn. Mater.* **159**, L1 (1996); J.C. Slonczewski, Excitation of spin waves by an electric current, *J. Magn. Magn. Mater.* **195**, L261 (1999).
- [7] L. Berger, Emission of spin waves by a magnetic multilayer traversed by a current, *Phys. Rev. B* **54**, 9353 (1996).
- [8] E. I. Rashba, Theory of electrical spin injection: Tunnel contacts as a solution of the conductivity mismatch problem, *Phys. Rev. B* **62**, R16267(R) (2000).
- [9] A. Fert, and H. Jaffrès, Conditions for efficient spin injection from a ferromagnetic metal into a semiconductor, *Phys. Rev. B* **64**, 184420 (2001).
- [10] Yu. A. Bychkov and E. I. Rashba, Properties of a 2D electron gas with lifted spectral degeneracy, *Sov. Phys. - JETP Lett.* **39**, 78-81 (1984)
- [11] D. Hsieh *et al.*, First observation of Spin-Momentum Helical Locking in Bi₂Se₃ and Bi₂Te₃ demonstration of Topological-Order at 300K and a realization of topological-transport-regime, *Nature (London)* **460**, 1101 (2009).
- [12] S. Zhang, Spin Hall Effect in the Presence of Spin Diffusion, *Phys. Rev. Lett.* **85**, 393 (2000).

- [13] A. Manchon and S. Zhang, Theory of spin torque due to spin-orbit coupling, *Phys. Rev. B* **79**, 094422 (2009).
- [14] Ka Shen, G. Vignale, and R. Raimondi, Microscopic Theory of the Inverse Edelstein Effect, *Phys. Rev. Lett.* **112**, 096601 (2014).
- [15] J. C. Rojas Sánchez, L. Vila, G. Desfonds, S. Gambarelli, J. P. Attané, J. M. De Teresa, C. Magén, and A. Fert, Spin-to-charge conversion using Rashba coupling at the interface between non-magnetic materials, *Nat. Commun.* **4**, 2944 (2013).
- [16] Steven S.-L. Zhang and Shufeng Zhang, Spin convertance at magnetic interface, *Phys. Rev. B* **86**, 214424 (2012).
- [17] A. Brataas, Y. V. Nazarov, and G. E.W. Bauer, Spin-transport in multi-terminal normal metal-ferromagnet systems with non-collinear magnetizations, *Eur. Phys. J. B* **22**, 99-110 (2001).
- [18] Kai Chen and Shufeng Zhang, Enhancement of spin accumulation in ballistic transport regime, *Phys. Rev. B* **92**, 214402 (2015).
- [19] Kai Chen, Weiwei Lin, C. L. Chien, and Shufeng Zhang, Temperature dependence of angular momentum transport across interfaces, *Phys. Rev. B* **94**, 054413 (2016).
- [20] W. Lin, K. Chen, S. Zhang, C. -L. Chien, Enhancement of Thermally Injected Spin Current through an Antiferromagnetic Insulator, *Phys. Rev. Lett.* **116**, 186601 (2016).
- [21] Kai Chen and Shufeng Zhang, Spin Pumping in the Presence of Spin-Orbit Coupling, *Phys. Rev. Lett.* **114**, 126602 (2015).
- [22] K. Chen and S. Zhang, Spin pumping induced electric voltages, *IEEE Magn. Lett.* **6**, 3000304 (2015).
- [23] K. Chen and S. Zhang, Roles of nonlocal conductivity on spin Hall angle measurement, *submitted for publication*
- [24] R. Urban, G. Woltersdorf, and B. Heinrich, Gilbert Damping in Single and Multilayer Ultrathin Films: Role of Interfaces in Nonlocal Spin Dynamics, *Phys. Rev. Lett.* **87**, 217204 (2001).

- [25] Y. Tserkovnyak, A. Brataas, and G. E. W. Bauer, Enhanced Gilbert Damping in Thin Ferromagnetic Films, *Phys. Rev. Lett.* **88**, 117601 (2002).
- [26] A. Brataas, Y. Tserkovnyak, G. E. W. Bauer, P. J. Kelly, Chapter from *Spin Current* edited by Sadamichi Maekawa, Sergio O. Valenzuela, Eiji Saitoh, and Takashi Kimura, Oxford Press (2012).
- [27] M. Oltcher, M. Ciorga, M. Utz, D. Schuh, D. Bougeard, and D. Weiss, Electrical Spin Injection into High Mobility 2D Systems, *Phys. Rev. Lett.* **113**, 236602 (2014).
- [28] M. Trott, and Ch. Schnittler, Construction and application of the Green's function for stepwise constant potentials, *Phys. Stat. Sol. B* **152**, 153 (1989).
- [29] K. Xia, P. J. Kelly, G. E. W. Bauer, A. Brataas, and I. Turek, Spin torques in ferromagnetic/normal-metal structures, *Phys. Rev. B* **65**, 220401 (2002); X.-T. Jia, K. Liu, K. Xia and G. E. W. Bauer, Spin transfer torque on magnetic insulators, *Europhys. Lett.* **96**, 17005 (2011).
- [30] S. Datta, *Electronic Transport in Mesoscopic Systems*, 1st Ed. (Cambridge University Press, Cambridge, UK, 1997).
- [31] H. E. Camblong, P. M. Levy, and S. Zhang, Electron transport in magnetic inhomogeneous media, *Phys. Rev. B* **51**, 16052(1995).
- [32] M. D. Stiles, and A. Zangwill, Anatomy of spin-transfer torque, *Phys. Rev. B* **66**, 014407 (2002).
- [33] Y. Tserkovnyak, A. Brataas, G. E. W. Bauer, and B. I. Halperin, Nonlocal magnetization dynamics in ferromagnetic heterostructures, *Rev. Mod. Phys.* **77** 1375 (2005).
- [34] V. Gasparian, T. Christen, and M. Büttiker, Partial densities of states, scattering matrices, and Greens functions, *Phys. Rev. A* **54**, 4022 (1996).
- [35] E. Šimánek, and B. Heinrich, Gilbert damping in magnetic multilayers, *Phys. Rev. B* **67**, 144418 (2003).
- [36] A. Takeuchi, K. Hosono, and G. Tatara, Diffusive versus local spin currents in dynamic spin pumping systems, *Phys. Rev. B* **81**, 144405 (2010).

- [37] G. D. Mahan, *Many-particle Physics*, 3rd Ed. (Plenum Publisher, New York, 2000).
- [38] D. Wei, M. Obstaum, M. Ribow, C. H. Back, and G. Woltersdorf, Spin Hall voltages from a.c. and d.c. spin currents, *Nat. Commun.* **5**, 3768 (2014).
- [39] O. Mosendz, J. E. Pearson, F. Y. Fradin, G. E. W. Bauer, S. D. Bader, and A. Hoffmann, Quantifying Spin Hall Angles from Spin Pumping: Experiments and Theory, *Phys. Rev. Lett.* **104**, 046601 (2010).
- [40] H. Nakayama, K. Ando, K. Harii, T. Yoshino, R. Takahashi, Y. Kajiwara, K. Uchida, Y. Fujikawa, and E. Saitoh, Geometry dependence on inverse spin Hall effect induced by spin pumping in Ni₈₁Fe₁₉/Pt films, *Phys. Rev. B* **85**, 144408 (2012).
- [41] Z. Feng, J. Hu, L. Sun, B. You, D. Wu, J. Du, W. Zhang, A. Hu, Y. Yang, D. M. Tang, B. S. Zhang, and H. F. Ding, Spin Hall angle quantification from spin pumping and microwave photoresistance, *Phys. Rev. B* **85**, 214423 (2012).
- [42] V. Vlaminck, J. E. Pearson, S. D. Bader, and A. Hoffmann, Dependence of spin-pumping spin Hall effect measurements on layer thicknesses and stacking order, *Phys. Rev. B* **88**, 064414 (2013).
- [43] W. Zhang, V. Vlaminck, J. E. Pearson, R. Divan, S. D. Bader, and A. Hoffmann, Determination of the Pt spin diffusion length by spin-pumping and spin Hall effect, *Appl. Phys. Lett.* **103**, 242414 (2013).
- [44] M. Obstbaum, M. Härtinger, H. G. Bauer, T. Meier, F. Swientek, C. H. Back, and G. Woltersdorf, Inverse spin Hall effect in Ni₈₁Fe₁₉/normal-metal bilayers, *Phys. Rev. B* **89**, 060407(R) (2014).
- [45] K. Ando, S. Takahashi, J. Ieda, H. Kurebayashi, T. Trypiniotis, C. H. W. Barnes, S. Maekawa, and E. Saitoh, Electrically tunable spin injector free from the impedance mismatch problem, *Nat. Mater.* **10**, 655 (2011).
- [46] I. Žutić, and H. Dery, Spintronics: Taming spin currents, *Nat. Mater.* **10**, 647 (2011).
- [47] E. Shikoh, K. Ando, K. Kubo, E. Saitoh, T. Shinjo, and M. Shiraishi, Spin-Pump-Induced Spin Transport in p-Type Si at Room Temperature, *Phys. Rev. Lett.* **110**, 127201 (2013).

- [48] Y. Shiomi, K. Nomura, Y. Kajiwara, K. Eto, M. Novak, K. Segawa, Y. Ando, and E. Saitoh, Spin-Electricity Conversion Induced by Spin Injection into Topological Insulators, *Phys. Rev. Lett.* **113**, 196601 (2014).
- [49] J.-C. Rojas-Sánchez, S. Oyarzún, Y. Fu, A. Marty, C. Vergnaud, S. Gambarelli, L. Vila, M. Jamet, Y. Ohtsubo, A. Taleb-Ibrahimi, P. Le Fèvre, F. Bertran, N. Reyren, J.-M. George, and A. Fert, Spin to Charge Conversion at Room Temperature by Spin Pumping into a New Type of Topological Insulator: α -Sn Films, *Phys. Rev. Lett.* **116**, 096602 (2016).
- [50] J.-C. Rojas-Sánchez, N. Reyren, P. Laczkowski, W. Savero, J.-P. Attané, C. Deranlot, M. Jamet, J.-M. George, L. Vila, and H. Jaffrès, Spin Pumping and Inverse Spin Hall Effect in Platinum: The Essential Role of Spin-Memory Loss at Metallic Interfaces, *Phys. Rev. Lett.* **112**, 106602 (2014).
- [51] Y. Wang, P. Deorani, X. Qiu, J. H. Kwon, and H. Yang, Determination of intrinsic spin Hall angle in Pt, *Appl. Phys. Lett.* **105**, 152412 (2014).
- [52] Mathias Weiler, Justin M. Shaw, Hans T. Nembach, and Thomas J. Silva, Phase-Sensitive Detection of Spin Pumping via the ac Inverse Spin Hall Effect, *Phys. Rev. Lett.* **113**, 157204 (2014).
- [53] C. R. Ast, J. Henk, A. Ernst, L. Moreschini, M. C. Falub, D. Pacilé, P. Bruno, K. Kern, and M. Grioni, Giant Spin Splitting through Surface Alloying, *Phys. Rev. Lett.* **98**, 186807 (2007).
- [54] Y. Tserkovnyak, A. Brataas, and G. E. W. Bauer, Spin pumping and magnetization dynamics in metallic multilayers, *Phys. Rev. B* **66**, 224403 (2002).
- [55] H. Kurt, R. Loloee, W. P. Pratt, Jr., and J. Bass, Spin-memory loss at 4.2 K in sputtered Pd and Pt and at Pd/Cu and Pt/Cu interfaces, *Appl. Phys. Lett.* **81**, 4787 (2002).
- [56] T. Yoshino, K. Ando, K. Harii, H. Nakayama, Y. Kajiwara, and E. Saitoh, Universality of the spin pumping in metallic bilayer films, *Appl. Phys. Lett.* **98**, 132503, (2011).
- [57] P. Hyde, L. Bai, D. M. J. Kumar, B. W. Southern, C.-M. Hu, S. Y. Huang, B. F. Miao, and C. L. Chien, Electrical detection of direct and alternating spin current

- injected from a ferromagnetic insulator into a ferromagnetic metal, Phys. Rev. B, **89**, 180404(R) (2014).
- [58] Althammer M *et al.*, Quantitative study of the spin Hall magnetoresistance in ferromagnetic insulator/normal metal hybrids, Phys. Rev. B **87**, 224401 (2013).
- [59] H. J. Jiao, G.E.W. Bauer, Spin Backflow and ac Voltage Generation by Spin Pumping and the Inverse Spin Hall Effect, Phys. Rev. Lett. **110**, 217602 (2013).
- [60] E. Saitoh, M. Ueda, H. Miyajima, G Tataru, Appl. Phys. Lett. **88**, 182509 (2006).
- [61] Ando K, Kajiwara Y, Takahashi S, Maekawa S, Takemoto K, Takatsu M, Saitoh E, Angular dependence of inverse spinHall effect induced by spin pumping investigated in a Ni₈₁Fe₁₉/Pt thin film, Phys. Rev. B **78**, 014413 (2008).
- [62] Y. K., Kato, R. C. Myers, A. C. Gossard, and D. D. Awschalom, Observation of the spin Hall effect in semiconductors, Science **306**, 1910-1913 (2004).
- [63] Luqiao Liu, Takahiro Moriyama, D. C. Ralph, and R. A. Buhrman, Spin-Torque Ferromagnetic Resonance Induced by the Spin Hall Effect, Phys. Rev. Lett. **106**, 036601 (2011).
- [64] C.-F. Pai, L. Liu, Y. Li, H. W. Tseng, D. C. Ralph, and R. A. Buhrman, Spin transfer torque devices utilizing the giant spin Hall effect of tungsten, Appl. Phys. Lett. **101**, 122404 (2012).
- [65] A. R. Mellnik, J. S. Lee, A. Richardella, J.L. Grab, P. J. Mintun, M. H. Fischer, A. Vaezi, A. Manchon, E.-A. Kim and N. Samarth, Spin-transfer torque generated by a topological insulator, Nature **511**, 449 (2014).
- [66] Luqiao Liu, Chi-Feng Pai, Y. Li, H. W. Tseng, D. C. Ralph, R. A. Buhrman, Spin torque switching with the giant spin Hall effect of tantalum, Science **336**, 555 (2012).
- [67] W. Zhang, W. Han, X. Jiang, S.-H. Yang and S. S. P. Parkin, Role of transparency of platinumferromagnet interfaces in determining the intrinsic magnitude of the spin Hall effect, Nat. Phys. **11**, 496-502 (2015).
- [68] X. Zhou, M. Tang, X. L. Fan, X. P. Qiu, and S. M. Zhou, Disentanglement of bulk and interfacial spin Hall effect in ferromagnet/normal metal interface, Phys. Rev. B **94**, 144427 (2016).

- [69] M. Cecot, L. Karwacki, W. Skowronski, J. Kanak, J. Wrona, A. Zywczyak, L. Yao, S. van Dijken, J. Barnas, T. Stobiecki, Influence of intermixing at the Ta/CoFeB interface on spin Hall angle in Ta/CoFeB/MgO heterostructures, *Sci. Reports* **7**, 968 (2017).
- [70] J. Kim, P. Sheng, S. Takahashi, S. Mitani, and M. Hayashi, Spin Hall Magnetoresistance in Metallic Bilayers, *Phys. Rev. Lett.* **116**, 097201 (2016).
- [71] K.-U. Demasius *et al.*, Enhanced spin-orbit torques by oxygen incorporation in tungsten films, *Nat. Commun.* **7**, 10644 (2016).
- [72] C. Hahn, G. de Loubens, O. Klein, M. Viret, V. V. Naletov, and J. Ben Youssef, Comparative measurements of inverse spin Hall effects and magnetoresistance in YIG/Pt and YIG/Ta, *Phys. Rev. B* **87**, 174417 (2013).
- [73] A. Azevedo, L. H. Vilela-Leão, R. L. Rodrãguez-Suárez, A. F. Lacerda Santos, and S. M. Rezende, Spin pumping and anisotropic magnetoresistance voltages in magnetic bilayers: Theory and experiment, *Phys. Rev. B* **83**, 144402 (2011).
- [74] H.L. Wang, C.H. Du, Y. Pu, R. Adur, P.C. Hammel, and F.Y. Yang, Scaling of Spin Hall Angle in 3d, 4d, and 5d Metals from Y3Fe5O12/Metal Spin Pumping, *Phys. Rev. Lett.* **112**, 197201 (2014).
- [75] H. E. Camblong, S. Zhang, and P. M. Levy, Magnetoresistance of multilayered structures for currents perpendicular to the plane of the layers, *Phys. Rev. B* **47**, 4735 (1993).
- [76] A. Barthelemy, A. Fert, Theory of the magnetoresistance in magnetic multilayers: Analytical expressions from a semiclassical approach, *Phys. Rev. B*, **43**, 13124 (1991).
- [77] A. Vedyayev, B. Dieny, N. Ryzhanova, Quantum Theory of Giant Magnetoresistance of Spin-Valve Sandwiches, *Europhys. Lett.*, **19** 329 (1992).
- [78] J. Barnas, Y. Bruynseraede, Electronic transport in ultrathin magnetic multilayers, *Phys. Rev. B*, **53**, 5449 (1996).
- [79] T. Valet, and A. Fert, Theory of the perpendicular magnetoresistance in magnetic multilayers, *Phys. Rev. B*, **48**, 7099 (1993).

- [80] K. Fuchs, The conductivity of thin metallic films according to the electron theory of metals, Proc. Camb. Phil. Soc. **34**, 100 (1938).
- [81] E. H. Sondheimer, A. H. Wilson, The theory of the magneto-resistance effects in metals, Proc. Royal Soc. **190** 435 (1947).
- [82] B.L. Johnson, R. E. Camley, Theory of giant magnetoresistance effects in Fe/Cr multilayers: Spin-dependent scattering from impurities, Phys. Rev. B **44**, 9997 (1991).
- [83] Y. Asano, A. Oguri, and S. Maekawa, Parallel and perpendicular transport in multilayered structures, Phys. Rev. B **48**, 6192 (1993).
- [84] A. Manchon and S. Zhang, Theory of nonequilibrium intrinsic spin torque in a single nanomagnet, Phys. Rev. B, **78**, 212405 (2008).
- [85] Jamali, M. et al., Spin-Orbit Torques in Co/Pd Multilayer Nanowires, Phys. Rev. Lett. **111**, 246602 (2013).
- [86] Miron, I. M. et al. Current-driven spin torque induced by the Rashba effect in a ferromagnetic metal layer, Nature Mater. **9**, 230-234 (2010).
- [87] Y. Fan *et al.*, Magnetization switching through giant spinorbit torque in a magnetically doped topological insulator heterostructure, Nat. Mater. **13**, 699 (2014).
- [88] X. Fan, H. Celik, J. Wu, C. Ni, K.-J. Lee, V. O. Lorenz and J. Q. Xiao, Quantifying interface and bulk contributions to spinorbit torque in magnetic bilayers, Nat. Commun. **5**, 3042 (2014).
- [89] A. Fert, and S. Zhang, Conversion between spin and charge currents with topological insulators, Phys. Rev. B, **94**, 184423 (2016).
- [90] F. Mahfouzi, N. Nagaosa, and B. K. Nikoliä, Spin-to-charge conversion in lateral and vertical topological-insulator/ferromagnet heterostructures with microwave-driven precessing magnetization, Phys. Rev. B **90**, 115432 (2014).
- [91] Mazin A. Khasawneh, Carolin Klose, W. P. Pratt, Jr., and Norman O. Birge, Spin-memory loss at Co/Ru interfaces, Phys. Rev. B **84**, 014425 (2011).
- [92] *Spin Current*, edited by S. Maekawa, S. O. Valenzuela, E. Saitoh, and T. Kimura (Oxford University, 2012).

- [93] Y. Ohnuma, H. Adachi, E. Saitoh, and S. Maekawa, Spin Seebeck effect in anti-ferromagnets and compensated ferrimagnets, *Phys. Rev. B* **87**, 014423 (2013).
- [94] K. Uchida, H. Adachi, T. Ota, H. Nakayama, S. Maekawa, and E. Saitoh, Observation of longitudinal spin-Seebeck effect in magnetic insulators, *Appl. Phys. Lett.* **97**, 172505 (2010).
- [95] K. Uchida, S. Takahashi, K. Harii, J. Ieda, W. Koshibae, K. Ando, S. Maekawa, and E. Saitoh, Observation of the spin Seebeck effect, *Nature* **455**, 778 (2008).
- [96] C. M. Jaworski, J. Yang, S. Mack, D. D. Awschalom, J. P. Heremans, and R. C. Myers, Observation of the spin-Seebeck effect in a ferromagnetic semiconductor, *Nat. Mater.* **9**, 898 (2010).
- [97] B. L. Giles, Z. Yang, J. S. Jamison, and R. C. Myers, Long-range pure magnon spin diffusion observed in a nonlocal spin-Seebeck geometry, *Phys. Rev. B* **92**, 224415 (2015).
- [98] Y. Kajiwara *et al.*, Transmission of electrical signals by spin-wave interconversion in a magnetic insulator, *Nature (London)* **464**, 262 (2010).
- [99] L. J. Cornelissen, J. Liu, R. A. Duine, J. Ben Youssef, and B. J. van Wees, Long-distance transport of magnon spin information in a magnetic insulator at room temperature, *Nat. Phys.* **11**, 1022 (2015).
- [100] S. T. B. Goennenwein, R. Schlitz, M. Pernpeintner, K. Ganzhorn, M. Althammer, R. Gross, and Hans Huebl, Non-local magnetoresistance in YIG/Pt nanostructures, *Appl. Phys. Lett.* **107**, 172405 (2015).
- [101] J. Li, Y. Xu, M. Aldosary, C. Tang, Z. Lin, S. Zhang, R. Lake, and J. Shi, Observation of magnon-mediated current drag in Pt/yttrium iron garnet/Pt(Ta) trilayers, *Nat. Commun.* **7**, 10858 (2016);
- [102] H. Wu, C. H. Wan, X. Zhang, Z. H. Yuan, Q. T. Zhang, J. Y. Qin, H. X. Wei, X. F. Han, and S. Zhang, Observation of magnon-mediated electric current drag at room temperature, *Phys. Rev. B* **93**, 060403 (2016).
- [103] Z. Qiu, J. Li, D. Hou, E. Arenholz, A. T. NDiaye, A. Tan, K. Uchida, K. Sato, Y. Tserkovnyak, Z. Q. Qiu, and E. Saitoh, Spin-current probe for phase transition in an insulator, *Nat. Commun.* **7**, 12670 (2016).

- [104] H. Wang, C. Du, P. C. Hammel, and F. Yang, Antiferromagnonic Spin Transport from Y3Fe5O12 into NiO, *Phys. Rev. Lett.* **113**, 097202 (2014).
- [105] C. Hahn, G. de Loubens, V. V. Naletov, J. Ben Youssef, O. Klein, and Michel Viret, Conduction of spin currents through insulating antiferromagnetic oxides, *Europhys. Lett.* **108**, 57005 (2015).
- [106] L. Frangou, S. Oyarzun, S. Auffret, L. Vila, S. Gambarelli, and V. Baltz, Enhanced Spin Pumping Efficiency in Antiferromagnetic IrMn Thin Films around the Magnetic Phase Transition, *Phys. Rev. Lett.* **116**, 077203 (2016).
- [107] K. Xia, P. J. Kelly, G. E.W. Bauer, A. Brataas, and I. Turek, *Phys. Rev. B* **65**, 220401 (2002); X.-T. Jia, K. Liu, K. Xia, and G. E.W. Bauer, Spin transfer torque on magnetic insulators, *Europhys. Lett.* **96**, 17005 (2011).
- [108] Y. Ohnuma, H. Adachi, E. Saitoh, and S. Maekawa, Enhanced dc spin pumping into a fluctuating ferromagnet near T_C , *Phys. Rev. B* **89**, 174417 (2014).
- [109] R. Cheng, J. Xiao, Q. Niu, and A. Brataas, Spin pumping and spin-transfer torques in antiferromagnets, *Phys. Rev. Lett.* **113**, 057601 (2014).
- [110] S. M. Rezende, R. L. Rodríguez-Suárez, and A. Azevedo, Diffusive magnonic spin transport in antiferromagnetic insulators, *Phys. Rev. B* **93**, 054412 (2016).
- [111] M. Weiler *et al.*, Experimental Test of the Spin Mixing Interface Conductivity Concept, *Phys. Rev. Lett.* **111**, 176601 (2013).
- [112] A. Brataas, Y. Tserkovnyak, G. E. W. Bauer, and B. I. Halperin, Spin battery operated by ferromagnetic resonance, *Phys. Rev. B* **66**, 060404(R) (2002).
- [113] J. Xiao, G. E. W. Bauer, K. C. Uchida, E. Saitoh, and S. Maekawa, Theory of magnon-driven spin Seebeck effect, *Phys. Rev. B* **81**, 214418 (2010).
- [114] H. Adachi, K. Uchida E. Saitoh and S. Maekawa, Theory of the spin Seebeck effect, *Rep. Prog. Phys.* **76**, 036501 (2013).
- [115] Steven S.-L. Zhang and S. Zhang, Magnon Mediated Electric Current Drag Across a Ferromagnetic Insulator Layer, *Phys. Rev. Lett.* **109**, 096603 (2012).
- [116] S. M. Rezende, R. L. Rodriguez-Suarez, R. O. Cunha, A. R. Rodrigues, F. L. A. Machado, G. A. Fonseca Guerra, J. C. Lopez Ortiz, and A. Azevedo, Magnon

- Mediated Electric Current Drag Across a Ferromagnetic Insulator Layer, *Phys. Rev. B* **89**, 014416 (2014).
- [117] F. Keffer, H. Kaplan and Y. Yafet, Am. Spin Waves in Ferromagnetic and Antiferromagnetic Materials, *J. Phys.* **21**, 250 (1953).
- [118] The $\zeta_{\mathbf{q}}^{-2}$ term in Eq. (13) emerges from the Umklapp scattering at the FI/AFI interfaces. Eq. (22) also includes such scattering for a NM/AFI interface, which has been pointed out in [109].
- [119] L. Liu, O. J. Lee, T. J. Gudmundsen, D. C. Ralph, and R. A. Buhrman, Current-Induced Switching of Perpendicularly Magnetized Magnetic Layers Using Spin Torque from the Spin Hall Effect, *Phys. Rev. Lett.* **109**, 096602 (2012).
- [120] J. Skalyo, Jr., G. Shirane, R. J. Birgeneau and H. J. Guggenheim, Magnons at Low and High Temperatures in the Planar Antiferromagnet K₂NiF₄, *Phys. Rev. Lett.* **23**, 1394 (1969); R. J. Birgeneau, H. J. Guggenheim, and G. Shirane, Spin Waves and Magnetic Ordering in K₂MnF₄ *Phys. Rev. B* **8**, 304 (1973).
- [121] T. Chatterji, G. J. McIntyre, and P.-A. Lindgard, Antiferromagnetic phase transition and spin correlations in NiO, *Phys. Rev. B* **79**, 172403 (2009).
- [122] S. Takei, T. Moriyama, Teruo Ono, and Y. Tserkovnyak, Antiferromagnet-mediated spin transfer between a metal and a ferromagnet, *Phys. Rev. B* **92**, 020409(R) (2015).
- [123] R. Khymyn, I. Lisenkov, V. S. Tiberkevich, A. N. Slavin, and B. A. Ivanov, Transformation of spin current by antiferromagnetic insulators, *Phys. Rev. B* **93**, 224421 (2016).
- [124] Satoshi Okamoto, Spin injection and spin transport in paramagnetic insulators, *Phys. Rev. B* **93**, 064421 (2016).
- [125] K. Y. Camsari, S. Ganguly, and S. Datta, Modular Approach to Spintronics, *Sci. Rep.* **5**, 10571 (2015).
- [126] P. C. van Son, H. van Kempen, and P. Wyder, Boundary Resistance of the Ferromagnetic-Nonferromagnetic Metal Interface *Phys. Rev. Lett.* **58**, 2271 (1987).

- [127] Y. Ji, , A. Hoffmann, , J. S. Jiang, and S. D. Bader, Spin injection, diffusion, and detection in lateral spin-valves, *Appl. Phys. Lett.* **85**, 6218 (2004).
- [128] H. Jaffrès, Spin Transport Goes Ballistic, *Physics* **7**, 123 (2014).
- [129] V. S. Rychkov, S. Borlenghi, H. Jaffrès, A. Fert, and X. Waintal, Spin Torque and Waviness in Magnetic Multilayers: A Bridge between Valet-Fert Theory and Quantum Approaches, *Phys. Rev. Lett.* **103**, 066602 (2009).
- [130] D. Culcer, J. Sinova, N. A. Sinitsyn, T. Jungwirth, A. H. MacDonald, and Q. Niu, Semiclassical Spin Transport in Spin-Orbit-Coupled Bands, *Phys. Rev. Lett.* **93**, 046602 (2004).
- [131] V. Y. Kravchenko and E. I. Rashba, Spin injection into a ballistic semiconductor microstructure, *Phys. Rev. B* **67**, 121310(R) (2003).
- [132] Y. -N. Qi and S. Zhang, Crossover from diffusive to ballistic transport properties in magnetic multilayers, *Phys. Rev. B* **65**, 214407 (2002).
- [133] Y. Qi and S. Zhang, Spin diffusion at finite electric and magnetic fields, *Phys. Rev. B* **67**, 052407 (2003).
- [134] E. G. Mishchenko and B. I. Halperin, Transport equations for a two-dimensional electron gas with spin-orbit interaction, *Phys. Rev. B* **68**, 045317 (2003).
- [135] A. A. Burkov, Alvaro S. Núñez, and A. H. MacDonald, Theory of spin-charge-coupled transport in a two-dimensional electron gas with Rashba spin-orbit interactions, *Phys. Rev. B* **70**, 155308 (2004).
- [136] P. W. Anderson, D. J. Thouless, E. Abrahams, and D. S. Fisher, New method for a scaling theory of localization, *Phys. Rev. B* **22**, 3519 (1980).
- [137] R. Landauer, Conductance determined by transmission: probes and quantised constriction resistance, *J. Phys.: Condens. Matter* **1**, 8099 (1989).
- [138] M. I. Dýakonov and V. I. Perel, Spin Orientation of Electrons Associated with the Interband Absorption of Light in Semiconductors, *Zh. Eksp. Teor. Fiz.* **60**, 1954 (1971).
- [139] M. I. Dýakonov and V. I. Perel, Spin relaxation of conduction electrons in non-centrosymmetric semiconductors, *Fiz. Tverd. Tela (Leningrad)* **13**, 3581 (1971).

- [140] M. A. Brand, A. Malinowski, O. Z. Karimov, P. A. Marsden, R. T. Harley, A. J. Shields, D. Sanvitto, D. A. Ritchie, and M. Y. Simmons, Precession and Motional Slowing of Spin Evolution in a High Mobility Two-Dimensional Electron Gas, *Phys. Rev. Lett.* **89**, 236601 (2002).
- [141] W. J. H. Leyland, R. T. Harley, M. Henini, A. J. Shields, I. Farrer, and D. A. Ritchie, Oscillatory Dyakonov-Perel spin dynamics in two-dimensional electron gases, *Phys. Rev. B* **76**, 195305 (2007).
- [142] A. V. Poshakinskiy, and S. A. Tarasenko, Electron spin dephasing in two-dimensional systems with anisotropic scattering, *Phys. Rev. B* **84**, 155326 (2011).
- [143] A. V. Poshakinskiy, and S. A. Tarasenko, Effect of Dresselhaus spin-orbit coupling on spin dephasing in asymmetric and macroscopically symmetric (110)-grown quantum wells, *Phys. Rev. B* **87**, 235301 (2013).
- [144] I. Žutić, J. Fabian, and S. Das Sarma, Spintronics: Fundamentals and applications, *Rev. Mod. Phys.* **76**, 323 (2004).
- [145] X. Cartoixà, D. Z.-Y. Ting, and Y.-C. Chang, Suppression of the Dyakonov-Perel spin-relaxation mechanism for all spin components in [111] zincblende quantum wells, *Phys. Rev. B* **71**, 045313 (2005).